

PHD

Phase Stability and Composition of Tin Sulfide for Thin-Film Solar Cells

Burton, Lee

Award date:
2014

Awarding institution:
University of Bath

[Link to publication](#)

General rights

Copyright and moral rights for the publications made accessible in the public portal are retained by the authors and/or other copyright owners and it is a condition of accessing publications that users recognise and abide by the legal requirements associated with these rights.

- Users may download and print one copy of any publication from the public portal for the purpose of private study or research.
- You may not further distribute the material or use it for any profit-making activity or commercial gain
- You may freely distribute the URL identifying the publication in the public portal ?

Take down policy

If you believe that this document breaches copyright please contact us providing details, and we will remove access to the work immediately and investigate your claim.

Phase Stability and Composition of Tin Sulfide for Thin-Film Solar Cells

submitted by

Lee Alan Burton

for the degree of Doctorate of Philosophy

of the

University of Bath

Centre for Sustainable Chemical Technologies

October 2014

COPYRIGHT

Attention is drawn to the fact that copyright of this thesis rests with its author. A copy of the thesis has been supplied on the condition that anyone who consults it is understood to recognise that its copyright rests with its author and that no quotation from the thesis and no information derived from it may be published without the prior written consent of the author.

This thesis may be made available for consultation within the University Library and may be photocopied or lent to other libraries for the purposes of consultation with effect from.....

Signed on behalf of the Faculty of Science

Summary

This thesis details an investigation into the factors that could be restricting the performance of tin sulfide thus far. It is shown that there is confusion in the literature with respect to the assignment of different tin sulfide phases, and that the presence of these phases cannot easily be discerned with routine diffraction methods. In order to better understand the behaviour of tin sulfide in devices, it is important to isolate these materials as separate components and to consider the distinct properties of each. Herein, the targeted synthesis of SnS, SnS₂ and Sn₂S₃ by chemical vapour transport is used to produce phase-pure single crystals, which are characterised in terms of structural, optical and electrical properties. These are compared directly with results from modern simulation methods as well as the work of others to explore fully the possible origins of performance losses. It is found that the work function of SnS is significantly lower than those of alternate successful photovoltaic materials, which means that novel device architectures are necessary in order to unlock the full potential of this promising photo-absorber. Concerns are also raised regarding the stability of the tin monosulfide phase with respect to degradation and defect formation over time, processes that undoubtedly affect device performance and lifetimes if sufficient safeguards are not put in place to suppress them. Further results of this 3 year research project also provide a broader platform for achieving sustainable light harvesting devices from the abundant and cheap elements, tin and sulfur.

Publications arising from this and related work:

- R. E. Banai, L. A. Burton, S. G. Choi, F. Hofherr, T. Sorgenfrei, A. Walsh, B. To, A. Cröll & J. R. S. Brownson; Ellipsometric characterization and density-functional theory analysis of anisotropic optical properties of single-crystal α -SnS, *Journal of Applied Physics*, **2014**, 116 (1), 013511.
- T. Shibuya, Y. Goto, Y. Kamihara, M. Matoba, K. Yasuoka, L. A. Burton & A. Walsh; From kesterite to stannite photovoltaics: Stability and band gaps of the Cu₂(Zn,Fe)SnS₄ alloy, *Applied Physics Letters*, **2014**, 104 (2), 021912.
- L. A. Burton, D. Colombara, R. D. Abellon, F. C. Grozema, L. M. Peter, T. J. Savenije, G. Dennler & A. Walsh; Synthesis, Characterization, and Electronic Structure of Single-Crystal SnS, Sn₂S₃, and SnS₂, *Chemistry of Materials*, **2013**, 25 (24), pp 4908.
- L. A. Burton & A. Walsh; Band alignment in SnS thin-film solar cells: Possible origin of the low conversion efficiency, *Applied Physics Letters*, **2013**, 102 (13), 132111.
- L. A. Burton & A. Walsh; Phase Stability of the Earth-Abundant Tin Sulfides SnS, SnS₂ and Sn₂S₃, *Journal of Physical Chemistry C*, **2012**, 116 (45), 24262.
- L. A. Burton & A. Walsh; A Photoactive Titanate with a Stereochemically Active Sn Lone Pair: Electronic and Crystal Structure of Sn₂TiO₄ from Computational Chemistry, *Journal of Solid State Chemistry*, **2012**, 196, 157160.

“On the arid lands there will spring up industrial colonies without smoke and without smokestacks; forests of glass tubes will extend over the plains and glass buildings will rise everywhere; inside of these will take place the photochemical processes that hitherto have been the guarded secret of the plants, but that will have been mastered by human industry which will know how to make them bear even more abundant fruit than nature, for nature is not in a hurry and mankind is. And if in a distant future the supply of coal becomes completely exhausted, civilization will not be checked by that, for life and civilization will continue as long as the sun shines!”

G. Ciamician, 1912.



Contents

1	Introduction	1
1.1	Solar energy	1
1.2	Solar cell operation	4
1.3	Solar cell fabrication	8
1.3.1	First generation PV	9
1.3.2	Second generation PV	10
1.3.3	Third generation PV	11
1.4	Earth abundant PV	15
1.5	Photovoltaic suitability of SnS	17
1.6	Earth abundance of SnS	17
1.7	Environmental impacts of SnS	22
1.8	SnS performance to date	24
1.9	Potential flaws of SnS	25
1.10	Thesis structure	27
2	Methodology	28
2.1	Experimental methods	28
2.1.1	Single crystal growth	28
2.2	Theoretical methods	30
2.2.1	<i>Ab initio</i> calculations	31
2.2.2	Electron density convergence	32
2.2.3	Atomic position convergence	42

2.2.4	Periodicity of solids	44
2.3	Methods comparison & discussion	47
3	Single crystal synthesis & thermodynamic properties	48
3.1	Single crystal growth & characterisation	48
3.1.1	Single crystal stability	52
3.1.2	Single crystal purity	56
3.2	Density functional theory analysis	57
3.2.1	Phase space analysis of tin sulfide	58
3.2.2	Enthalpies of formation & relative stabilities	60
3.2.3	Enthalpies of sublimation & disproportionation	66
3.2.4	Enthalpies of reaction with oxygen	68
3.2.5	Enthalpies of reaction with iodine	69
3.2.6	Chemical reactions in potential device configurations	70
3.3	Results comparison & discussion	73
4	Electronic & optical properties	75
4.1	Single crystal analysis	75
4.1.1	Single crystal band gaps from reflectivity	75
4.1.2	SnS band gap from optical absorption relative to temperature	78
4.1.3	Evaluation of work function & band gaps for all phases	80
4.2	Density function theory analysis	82
4.2.1	Band gaps & work functions for all phases	83
4.2.2	Band structure of SnS	85
4.2.3	Temperature dependent electronic structure of SnS	88
4.2.4	Dielectric function of SnS	91
4.2.5	Absorption coefficient of SnS	95
4.2.6	Assessment of potential device back contacts for SnS	95
4.3	Results comparison & discussion	100
5	Transport & defect properties	105
5.1	Single crystal analysis	105

5.1.1	Conductivity, mobility & related properties for all phases	105
5.1.2	Pulse-radiolysis time-resolved microwave conductivity	107
5.1.3	Hall-effect mobility measurements	113
5.2	Density functional theory analysis	115
5.2.1	Intrinsic defect formation for all phases	115
5.2.2	Charge carrier effective masses	117
5.2.3	Charge carrier mobilities	119
5.2.4	Modelled conductivity for SnS	124
5.2.5	Results comparison & discussion	126
6	Conclusion	129
7	Future work	134
Bibliography		136
A Appendix		153
A.1	Single crystal XRD data	153
A.2	Glow discharge mass spectroscopy data	154
A.3	X-ray photoelectron spectroscopy data	157
A.4	Optical absorption coefficient script	158
A.5	Charge carrier mobility script	161

List of Figures

1-1	Annual solar irradiation in Europe & Germany's power production mix	3
1-2	Maximum PV efficiency & solar energy spectrum	5
1-3	Schematic of a thin-film solar cell	8
1-4	Hybrid perovskite crystal structure & associated molecular dipole	13
1-5	Highest achieved solar cell efficiency records	14
1-6	Observed phase segregation & calculated stability region for CZTS	16
1-7	Relative abundance of elements in the earth's crust	18
1-8	Maximum potential for deployment of alternative photoactive materials	21
1-9	Annual production of elements important for photovoltaic applications	22
1-10	Life cycle impact analysis of common PV components	23
1-11	Example XRD pattern showing mixed phases of tin sulfide	26
2-1	Schematic representation of chemical vapour transport process	30
2-2	Representative flow chart of an <i>ab initio</i> calculation process	31
2-3	Representation of the LDA & GGA treatments of electron density	41
3-1	Crystal batches obtained from chemical vapour transport	50
3-2	Obtained & predicted XRD patterns for tin sulfide structures	51
3-3	TGA analysis of single crystals	53
3-4	Observed oxidation of SnS single crystals	54
3-5	Observed sulfur loss of SnS single crystals	55
3-6	Grazing incidence XRD on the SnS surface	56
3-7	The crystal structures of the tin sulfides considered in this work	59

3-8 Convex hull showing enthalpy of formation against elemental composition	63
3-9 Energy-volume curve for ZB & RS SnS & the structure of amorphous SnS	64
3-10 Predicted XRD patterns for RS & ZB SnS	65
3-11 The calculated structures of molecular Sn_2S_3 , SnS_2 & SnS	66
3-12 Phase diagrams for Sn - S - I & Sn - S - O configuration space	71
4-1 UV/vis reflectance analysis of single crystals	77
4-2 Absorption profiles as a function of temperature for SnS	79
4-3 Observed SnS band gaps as a function of temperature	80
4-4 Band edge analysis with UPS & IPES techniques	81
4-5 Calculated electrostatic potential for SnS	84
4-6 Calculated band offset diagram for each of the three tin sulfide phases	85
4-7 The Brillouin zone of the orthorhombic SnS system	86
4-8 Band structure analysis for SnS	87
4-9 Thermal expansion & temperature dependent band structure of SnS	90
4-10 Temperature dependence of the SnS unit cell volume & band gap	91
4-11 Calculated & spectroscopically determined dielectric spectra for SnS	94
4-12 Critical point assignments for SnS	94
4-13 Optical absorption coefficient for SnS derived from DFT	96
4-14 Calculated band offset diagram for tin sulfide & metal contacts	99
5-1 Schematic relationship between quasi-Fermi levels & device voltage	110
5-2 Normalised PR-TRMC data for SnS_2 & Sn_2S_3 phases	111
5-3 Normalised PR-TRMC conductivity data for SnS_2 & Sn_2S_3	112
5-4 PR-TRMC signal lifetime for SnS_2	113
5-5 Anisotropic conductivity calculated for SnS	125
5-6 k -grid convergence for the conductivity of SnS from the BoltzTrap code .	126

List of Tables

3.1	Reaction conditions required to synthesise the separate phases of tin sulfide	49
3.2	Elemental composition of single crystals from EDS	52
3.3	GDMS analysis of single crystal SnS	57
3.4	Reported structural parameters from experiment & theory	61
3.5	Enthalpies of formation	62
3.6	Enthalpies of sublimation	67
3.7	Enthalpies of oxidation	68
3.8	Enthalpies of disproportionation	68
3.9	Enthalpies of iodination	70
3.10	Enthalpies of reactions for metal disulfides	72
4.1	Reported optical band gaps of the tin sulfides from the literature	76
4.2	UPS/IPES determined properties for the tin sulfide phases	81
4.3	Calculated values of dielectric constants of SnS	93
4.4	Calculated work functions for metal surfaces	98
4.5	Band gaps & ionisation potential for metal disulfide interlayers	100
4.6	Obtained fundamental band gaps of the tin sulfides	101
5.1	Reported electron transport properties of the tin sulfides	107
5.2	Point defect formation energies & concentrations	116
5.3	Charge carrier effective masses for SnS from Boltzmann transport analysis	120
5.4	Data used for the calculation of deformation potential of SnS	122

A.1	Single crystal crystallographic data for SnS ₂ & Sn ₂ S ₃	153
A.2	Glow discharge mass spectroscopy of an SnS single crystal	154
A.3	XPS atomic concentration peak assignments of SnS, SnS ₂ & Sn ₂ S ₃	157

List of Abbreviations

CIGS	Copper Indium Gallium Diselenide
CVT	Chemical Vapour Transport
CZTS	Copper Zinc Tin Sulfide
DFT	Density Functional Theory
EDS	Energy Dispersive Spectroscopy
FHI AIMS	Fritz Haber Institute Ab Initio Molecular Simulations Package
FTIR	Fourier Transform Infra-Red
HFT	Hartree Fock Theory
ICSD	Inorganic Crystal Structure Database
IPES	Inverse Photo-Emission Spectroscopy
IR	Infra-Red
GDMS	Glow Discharge Mass Spectroscopy
GGA	Generalised Gradient Approximation
LCA	Life Cycle Analysis
LDA	Local Density Approximation
MD	Molecular Dynamics
NIR	Near Infra-Red
PAW	Projector-Augmented Wave
PR-TRMC	Pulse-Radiolysis Time-Resolved Microwave Conductivity
PV	Photovoltaic
RS	Rocksalt
SCF	Self Consistent Field

SEM	Scanning Electron Microscopy
TCO	Transparent Conducting Oxides
TGA	Thermo-Gravimetric Analysis
UPS	Ultraviolet Photoelectron Spectroscopy
UV/vis	Ultraviolet-Visible Spectroscopy
VASP	Vienna Ab Initio Simulation Package
XC	Exchange - Correlation
XPS	X-ray Photoelectron Spectroscopy
XRD	X-ray Diffraction
ZB	Zincblende

List of Symbols

α	Optical Absorption Coefficient
A	Helmholtz Free Energy
χ	Single Electron Orbital
c	Speed of Light
C	Atom Core Potential
C_l	Longitudinal Elastic Constant
D	Charge Diffusion Coefficient
ϵ	Energy of an Orbital or Band
ϵ_0	Static Dielectric Constant
ϵ_∞	High Frequency Dielectric Constant
ϵ_{ion}	Ionic Contribution to the Dielectric Response
ϵ_v	Permittivity of Free Space
ϵ_1	Real Dielectric Function
ϵ_2	Imaginary Dielectric Function
η	Complex Shift
e	Elementary Charge
E	Energy of a System
E_d	Deformation Potential
E_F	Fermi Energy
F	Force Acting on a Species
h	Planck's Constant
\hbar	Reduced Planck's Constant ($h/2\pi$)

H	Enthalpy
\hat{H}	Hamiltonian Operator
i	Electron
I	Nucleus
k	Wave Vector
k_B	Boltzmann Constant
λ	Vibrational Mode
L	Crystal Grain Size
μ	Chemical Potential
μ	Mobility
μ_i	Ionised Impurity Scattering
μ_g	Grain Boundary Scattering
μ_l	Lattice Vibration Scattering
μ_n	Neutral Impurity Scattering
m^*	Effective Mass
m_e	Mass of an Electron
M	Effective Mass Tensor
∇	Laplacian Operator
N	Carrier Concentration
ω	Frequency
Ω	Volume of a Unit Cell
Ψ	Electron Wave Function
Ψ_b	Grain Boundary Energy Barrier
p	Momentum
P	Pressure
P	Power
P_v	Principal Value
q	Incident Wave Bloch Vector
q	Electrical Charge

Q	Electron Beam Charge
R	Periodic Unit Cell Length
r_x	Species' Spacial Coordinate
ρ	Charge Density
σ	Conductivity
s_x	Species' Spin Angular Momentum
S	Entropy
τ	Relaxation Time
t	Time
T	Temperature
T	Kinetic Energy
U	Potential Energy
V	Volume
Z	Partition Function
Z_x	Species' Charge

Acknowledgments

I would like to thank Prof. Aron Walsh, who sincerely could not have been a better supervisor. Thanks to my fellow students in the Centre for Sustainable Chemical Technologies who made doing a PhD not only bearable but actively enjoyable, and thanks to the DTC for providing me with the balanced mixture of support and freedom to allow me to grow as a person as well as a scientist.

Some members of the Walsh Group weren't terrible.

Direct contributors to this work are listed as follows:

- Thomas J. Whittles, David Hesp and Dr Vin R. Dhanak, University of Liverpool, UK, for XPS, UPS and IPES data.
- Mohana Rajpalke, Dr Wojciech M. Linhart and Dr Tim D. Veal, University of Liverpool, UK, for temperature dependent FTIR data.
- Dr James J. Walsh, University of Liverpool, UK, for UV/vis reflectance data.
- Dr Ruben D. Abellon, Dr Ferdinand C. Grozema and Dr Tom J. Savenije, Delft University of Technology, The Netherlands, for PR-TRMC analysis data.
- Alexander Polizzotti, Katy Hartman, Dr Rafael Jaramillo, Dr Jasmin Hofstetter and Dr Tonio Buonassisi, Massachusetts Institute of Technology, USA, for Hall effect and GDMS impurity data.
- Dr Christopher Woodall, University of Bath, UK, for single crystal and powder XRD data.

- Adam J. Jackson, University of Bath, UK, for use of the methods flowchart, Figure 2-2.
- Dr Jonathan M. Skelton, University of Bath, UK, for help with SnS thermal expansion and *ab initio* conductivity data.
- Rona Banai and Dr Jeffrey R. S. Brownson, Pennsylvania State University, USA for the synthesis of single crystal SnS by the Bridgman-Stockbarger method.
- Dr Sukgeun G. Choi and Dr Bobby To, National Renewable Energy Laboratory, USA, for variable angle ellipsometry analysis of single crystal SnS.
- Helen H. Park, Prasert Sinsermsuksakul and Prof. Roy Gordon, Harvard University, USA, for useful discussions.
- Dr Gerardo Laramona and Dr Gilles Dennler, IMRA-Europe, France, for useful discussions.

Chapter 1

Introduction

1.1 Solar energy

To date, the development of the global economy has been based on large reserves of fossil fuels that can be burned to provide energy for heat, electricity and work. These reserves correspond to energy from the sun captured by organisms over hundreds of millions of years, now being depleted at such a rate that mankind is beyond the threshold of anthropomorphic climate change and ocean acidification from CO₂ release.¹ With rising population and an accelerated rate of global development, energy demand only continues to rise, leading to predictions of peak oil occurring before 2030.^{2,3} Consequently, one of the greatest challenges facing humanity is maintaining the current standard of living for future generations, without causing irreparable damage to the global ecosystem. The first step towards such an end is the reduction, or indeed, elimination of CO₂ emissions.⁴

Renewable energy is a term describing methods of power generation that do not deplete finite fuels or release net positive amounts of CO₂ to the atmosphere. Almost all of these technologies derive their energy either directly or indirectly from the sun, as the solar resource is enormous. Quantitatively it has been estimated that the earth receives around

885 million terawatt hours worth of solar energy each year,⁵ which is greater than 16 thousand times more energy than was consumed globally in 2011.⁶

In this thesis, photovoltaic (PV) technology is to be discussed; the use of semiconductor materials to harvest the massive solar resource directly to produce electricity. This technology offers a number of significant benefits over alternative renewable energies, including:

- PV systems are within the reach of individuals, co-operatives and businesses that want to mitigate variable energy costs.
- Unlike many other electricity generation technologies, PV cells are sufficiently small to be used for temporary or mobile structures such as military bases and vessels.⁷
- The solar resource is available everywhere in the world. Even Germany, which receives relatively low levels of solar radiation (as shown in Figure 1-1), was able to meet 5.7 % of its national energy consumption using PV in 2013.⁸
- Unlike conventional power plants, PV has relatively low operation costs and requires no maintenance. Combined with manufacturers' warranties of up to 25 years for installed devices, PV provides a valuable cost hedge against volatile fossil fuel prices.
- While PV electricity production is variable, it does have a high coincidence with peak electricity demand, as also shown in Figure 1-1.⁹ It is also easy to anticipate based on modern weather prediction technology.
- The record efficiency for PV devices is more than five times greater than the best possible efficiencies for photosynthesis *before* the biomass can be processed into

fuels for energy.^{10,11} Also, unlike biofuels, PV need not compete with space for agriculture or nature, with rooftop solar a viable option.¹²

- Reductions in PV production costs mean that solar energy can now compete on a cost per watt basis with conventional methods of generation in Italy, Spain and Germany.¹³ Many other regions with relatively low electricity production costs and/or large solar resources are also predicted to achieve this parity before 2020.¹⁴

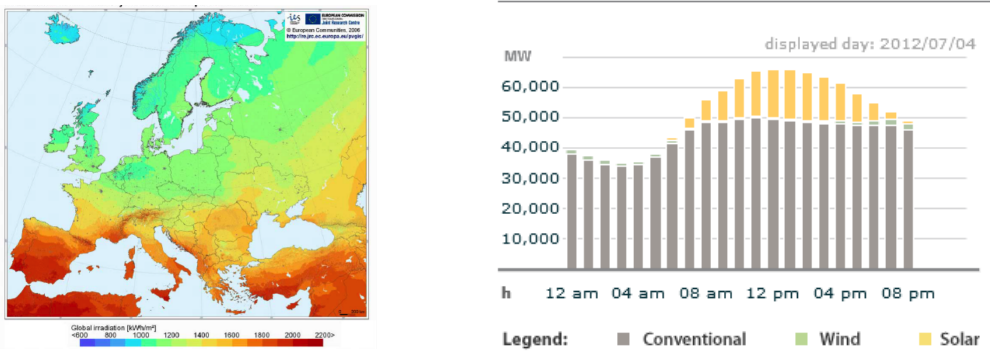


Figure 1-1: Yearly sum of solar irradiation in Europe (left) and power generation by type in Germany on a sample date as shown (right).¹⁵

Unfortunately, generating the total amount of energy we now consume using solar power alone is practically impossible in the near term future, and getting even close raises issues with resource availability. Thus to maximise the potential of PV in the long-term, it is important to consider component suitability today. In order to accomplish such a task however, it is important to first deconstruct existing photovoltaic technologies in order to identify areas of potential improvement.

1.2 Solar cell operation

This section describes the operating principles of photovoltaic technology and the physical properties one would seek in the associated components.

Beginning with the material that absorbs the sunlight, a semiconductor is required. A semiconductor by definition is a material with a band gap *i.e.* a discontinuity in the allowed energetic states of electrons in the solid. This feature is the key to photovoltaic activity as it acts as the barrier to electron relaxation after being excited by a photon. If no such barrier is present the electron can dissipate the energy of the photon by heat on a timescale too rapid to prevent. A larger band gap means more potential energy or voltage can be provided by a device, but fewer photons can be absorbed, and it is this parameter that determines electrical current. Together voltage and current dictate a cells power and a compromise should be found between the two. Shockley and Queisser calculated that the optimal absorber band gap occurs at a photon energy of around 1.34 electron volts,¹⁶ using the solar energy spectrum experienced at the earth's surface, both of which are shown in Figure 1-2. This provides a convenient screening parameter for potential photovoltaic materials.

Besides presenting a magnitude in energy, band gaps can also be direct or indirect in nature. For a band gap to be direct, an electron must be able to traverse said gap with no change in crystal momentum. If this is not the case the gap is said to be indirect. It is desirable for a photovoltaic material to exhibit a direct band gap as indirect band gap materials require light *and* heat to promote electrons across the gap, with an associated weaker optical absorption and loss of device efficiency.

When light shines on a semiconductor and a photon is absorbed, an electron is promoted from the full valence band to the empty conduction band where it can migrate away

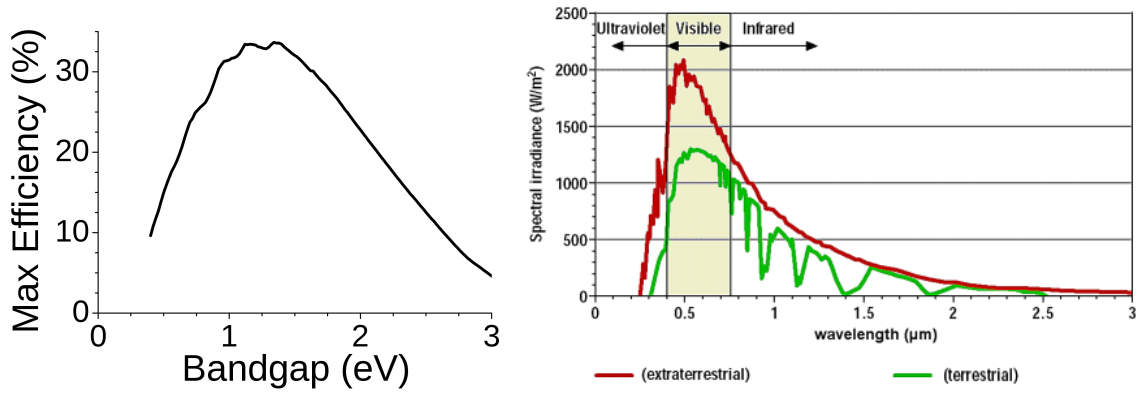


Figure 1-2: The Shockley Queisser limit of maximum PV efficiency as a function of band gap and average solar spectral irradiance outside the earths atmosphere (extraterrestrial) and incident on the surface (terrestrial).¹⁷

from its original position. This leaves behind an effective positive charge as the species was neutral to begin with. This electron ‘hole’ can be filled by a neighbouring electron, creating another hole on the adjacent space. This mechanism can be repeated such that the electron vacancy migrates in the opposite direction to the electrons filling the previous holes. Thus for each photon absorbed two mobile charge carriers are produced, one positive and one negative.

Normally, as the excited electron (with a negative charge) and coexistent hole (with a positive charge) are electrostatically attracted to each other, they won’t migrate very far apart. This binary species is called an exciton and will have a lifetime typically of femto-seconds before the electron ejects a photon that corresponds to the energy of the band gap and recombines with the hole it left behind. This process is termed radiative recombination and is an undesirable process for PV applications as that electron is no longer available to do work. However, the exciton is stabilised or ‘screened’ by the dielectric constant of the material and if one applies an electric field across an exciton, it is possible to cause the bound hole and electron to migrate away from each other. A potential gradient can

be generated without the need for any externally applied bias by using crystal defects, in what is called a *p-n* junction.

While, in an ideal, pure semiconductor there are no available states for an electron or hole to occupy in the band gap, all crystals, except at zero Kelvin, contain impurities or imperfections. If these impurities introduce a localised empty state slightly higher in energy than the valence band, it will be able to accept an electron from the valence band. This will leave behind a hole that can act as a charge carrier and conduct. When a significantly large amount of these defects are present in a material, it determines the conductivity, and the material is termed *p*-type (where *p* stands for positive). Conversely, if the majority of defects have a filled state slightly lower in energy than the conduction band, then the electrons from the dopant can be easily promoted to the empty band. Conduction can then occur predominantly with the electron charge carrier, and is the case for so-called *n*-type materials (where *n* stands for negative).

If a *p*-type and *n*-type material are placed together the charge carriers recombine at the interface between the two, forming a depletion zone. This acts to charge the interface of the *p*-type substrate negative (because the holes have been filled by electrons) and the *n*-type substrate positive (because the electrons have moved across the interface to fill the holes). By employing this set up in a photovoltaic cell, a natural electric field is provided so that when excitons are created by photons, the charge carriers can separate across this field and produce a working current.

It is important to note that these defect states can also be introduced intentionally as extrinsic dopants. In this way it is possible control conductivity and even create an *p-n* junction across a single material by doping opposing sides differently. However, care must be taken in the selection of suitable dopants as defect energy levels that are close to the centre of the band gap can allow for charge recombination in so called trap-assisted or Shockley-Read-Hall recombination.

As well as the *p*- and *n*-type materials there must be electrodes present that are able to collect the charges once they have been separated by the *p-n* junction. For this reason it is important that both components of the junction allow for as large a charge carrier diffusion length as possible, and as small a thickness as possible, to increase the likelihood that the charges reach the contact before recombination.

The so-called back electrode in a cell, i.e. the component placed furthest from the light source, is usually a metal, as metals have high conductivity and reflectivity. This allows the electrode to not only collect charges but also reflect any photons that were not absorbed by the photoactive material back into the cell, thereby reducing losses.¹⁸

Finally the top electrode, or window layer, must be able to function as an electrode and, at the same time, be stable with respect to exposure to atmospheric conditions and be transparent to visible light. The class of materials selected for this task are ‘transparent conducting oxides’ (TCOs) because they typically have wide enough band gaps to be inactive with respect to photon absorption up to around 3 eV and they are stable in air as they are already oxidised. The most common TCOs at the time of writing are indium doped tin oxide (ITO), fluorine doped tin oxide (FTO) and aluminium doped zinc oxide (ZnO:Al).

The electrodes may not have a band gap (metals certainly do not) but are still able to receive charge carriers from the *p-n* junction. That is because all materials have energetically allowed states that fill predictably, starting from the lowest in energy and increasing from there. The energy up to which the states are filled is called the Fermi level and in a *p*-type semiconductor will usually correspond to the valence band maximum. By definition this must exist below the energy of a free electron outside the material, known as the vacuum level, or else the material would not be stable. The difference in energy between the Fermi level and the vacuum level is called the work function and characterises how strongly a solid holds on to its electrons. This is important as electrons will spontaneously

move from a solid with a low work function to a large work function if they are able, and so factor into device design.

The four components discussed in this section are arranged as shown in Figure 1-3.

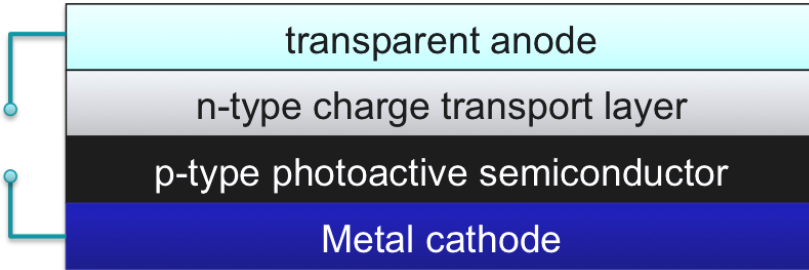


Figure 1-3: Schematic of a thin-film solar cell. A successful example might include a gold cathode, a cadmium telluride photoactive component, a cadmium sulfide charge transport layer and a zinc oxide transparent anode.

All of the materials properties discussed in this section that directly affect device operation can be found or approximated from first principles simulation methods or reported in experiment using modern spectroscopic techniques. Thus, it is possible to assess the photovoltaic suitability of a given material without the need to fabricate a PV device. Indeed, assessing the absorber material properties outside of a device configuration can yield a greater understanding of the likely limiting factors that are obscured once contained within a cell.

1.3 Solar cell fabrication

Modern photovoltaic technology can be traced back to 1879 when Adams and Day described a generation of internal voltages in a selenium cell upon exposure to sunlight.¹⁹ Since this initial discovery, photovoltaic devices have progressed from the first cell with an efficiency of 1%,²⁰ through the original device of modern architecture at 6 % in 1954,²¹

to single-junction cells today with certified efficiencies of 28.8%.²²

There are typically considered to be three generations of PV cell technologies available depending on the materials used and the level of commercial maturity. Each of these has its own advantages and disadvantages that are subsequently discussed.

1.3.1 First generation: Crystalline silicon photovoltaics

First-generation PV systems are fully commercialised and use single crystalline or multi-crystalline silicon. Commercial production of crystalline silicon modules began in 1963 when the ‘Sharp’ Corporation installed a 242 W PV fixture on a lighthouse, the world’s largest installation at the time.²³ Not only is this technology mature in itself, but it builds upon the accumulated knowledge base of the silicon-chip electronics industry and benefits from the fact that silicon is one of the most abundant elements in the earth’s crust. As a result, these type of cells dominate the current PV market, accounting for around 87 % of global PV sales in 2010.⁹

The record efficiency for a crystalline silicon module currently stands at 24.7 %,²⁴ with typical commercial cells in the range of 14 to 19 %.⁹ However, silicon is an indirect band gap material and as such needs a larger light-harvesting region than typical direct gap materials in order to operate effectively.²⁵ The large thickness of high purity crystalline silicon required leads to high processing costs and has been estimated to incur losses of around 20 % in device efficiency,²⁶ as the increased distance charges must travel before extraction means recombination is more likely to occur. These factors form the primary impetus behind the wealth of research that has led to the development of the subsequent generations of photovoltaic devices.

1.3.2 Second generation: Thin-film photovoltaics

‘Second generation’ is a term used to refer to devices that recently reached market maturity. These cells, more commonly referred to as ‘thin-film’ devices, are considered promising alternatives to crystalline silicon solar cells because the photoactive components are more optimal photon absorbers. As a consequence, they require up to 99 % less active material than crystalline silicon in order to absorb the same amount of light (typically 1 to 4 μm in thickness).⁹

For this reason, among others, thin-films cells are thought to be the simplest, cheapest and most sustainable method of solar cell production.²⁷ Besides which, the highest efficiency achieved to date for a single junction cell was obtained with a thin-film device.²²

The three primary types of thin-film solar cells in terms of commercial development are:

- Amorphous silicon
- Cadmium telluride
- Copper indium selenide and copper indium gallium diselenide

Amorphous silicon solar cells are the most mature thin-film solar cells, with module efficiencies in the range of 4 % to 8 %, and the record efficiency standing at 10.1 %.²⁸ A major disadvantage of amorphous silicon cells however is that they suffer from a significant reduction in power output over time (up to 35 %), as sunlight degrades their performance.

Cadmium telluride thin-film PV cells have the lowest production costs of any PV technology,⁹ but they have high efficiencies (a record of 19.6 %)²² and are robust with respect to imperfections.²⁹ Perceived issues surrounding the toxicity of elemental cadmium have

been shown to be baseless,³⁰ however tellurium is relatively rare and expensive. Regardless, the so-called payback time for CdTe cells has been shown to be less than one year, a powerful advantage over first generation technologies.³¹

Copper indium selenide and copper indium gallium diselenide (CIGS) PV cells also offer high efficiencies of up to a record 19.8 %,²² but they are afflicted by the same problems as CdTe in that the constituent element gallium is rare and expensive. Both CIGS and CdTe commercial modules typically range between 7-11 % in efficiency, but this is expected to increase as the relatively new technologies mature.⁹

1.3.3 Third generation: Novel and emerging technologies

Third-generation describes systems that are still under demonstration or are not yet market ready. Some third-generation PV technologies are beginning to be commercialised, however it remains to be seen how successful they will be in taking market share from existing technologies. The most notable third-generation PV devices are:

- Multi-junction
- Organic
- Hybrid perovskites
- Dye-sensitised

Multi-junction, or tandem solar cells consist of a stack of multiple different semiconductors, chosen to absorb separate regions of the solar spectrum individually. Naturally such cells can achieve greater efficiencies than single junction devices, with a record of 44.4 %,²² and a theoretical limit of 59 % efficiency.³² The most commonly employed materials are Ge, GaAs or InGaAs, and InGaP, which are expensive in themselves and

the extra processing requirements increase costs further. As such, these expensive devices are usually reserved for critical applications *e.g.* satellite deployment and space-faring technologies.³³

Organic solar cells are composed of carbon based, usually polymeric materials, that now have efficiencies in the range 4 to 5 % commercially and a 10.7% record.²² The major challenge for organic solar cells is their instability over time, much the same as amorphous silicon, but their production allows for high-speed and low temperature manufacturing techniques. As a result, organic solar cells may become cost competitive with other PV technologies in certain applications, as the manufacturing costs are marginal and continuing to decline.⁹ For example, their lightweight and flexible properties make them ideal for mobile applications such as wearable electronics.

Hybrid perovskite ($\text{CH}_3\text{NH}_3\text{PbI}_3$) material research dates back to the 1920's,³⁴ but only recently has the field attracted a great deal of excitement after a reported inclusion of them into a device.³⁵ The record efficiencies for these devices have exploded from the original 3.8 % in 2009 to 19.3 % at the time of writing.³⁶ While these high efficiencies are obtained only in the lab and are typically very short-lived, the mechanism behind these high efficiencies is potentially novel. One theory states that the organic molecule in this inorganic structure represents a rotating dipole that can stabilise generated charges or enhance applied fields (see Figure 1-4).³⁷ The full effect of this is yet to be understood but it seems safe to assume that hybrid perovskites, or materials of similar nature, will play a major role in the future of photovoltaics.

Finally, the class of devices known as dye-sensitised cells use chemically tunable dyes adsorbed onto a high surface area TiO_2 substrate as the photoactive component. The strong absorption and chemical functionality associated with molecular dyes makes them ideally suited for PV applications, and the possibility of absorbing light over multiple ranges of the electromagnetic spectrum with a mix of dyes (similar to the operation principles of

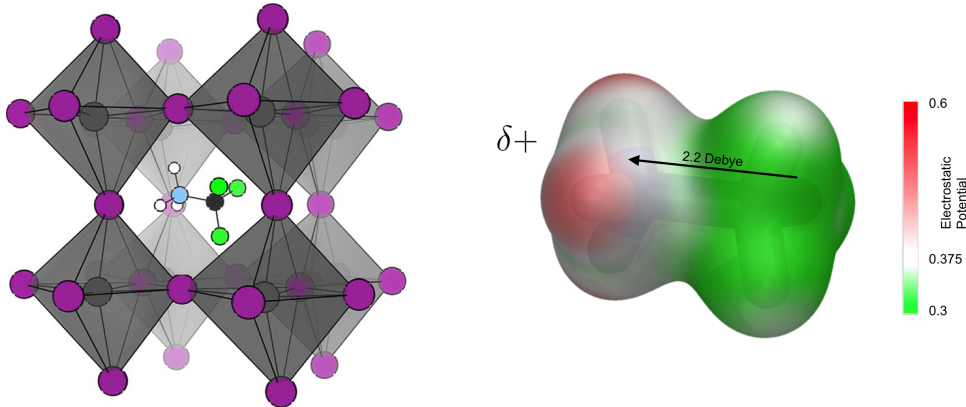


Figure 1-4: Schematic of hybrid perovskite crystal structure showing the inorganic ‘cage’ and intercalated molecule (left) with the associated dipole of the organic component (right).³⁷

tandem devices) is appealing.³⁸

In practice, however, this technology suffers from many drawbacks, not least among which is that it is the only PV cell to contain a liquid component.³⁹ This so called redox mediator is required in order to regenerate the dye after photo-excitation, however not only is this component corrosive, but the repeated thermal expansion of this fluid during normal photovoltaic operation can compromise device seals, resulting in relatively short device lifespans.⁴⁰ This branch of research has suffered a recent reduction in interest as many research groups transition to the more promising hybrid perovskite devices that are equally facile to solution process, simpler and yield higher efficiencies.⁴¹

In addition to the above mentioned third-generation technologies, there are a number of novel solar technologies under development that use quantum dots,⁴² quantum wires,⁴³ or quantum wells.⁴⁴ These technologies are thought to be able to achieve very high efficiencies in certain applications by overcoming the thermodynamic limitations of conventional cells, but they are currently far from commercial deployment. The certified progress of all of the technologies discussed in this section, and more, are plotted over time in Figure 1-5.

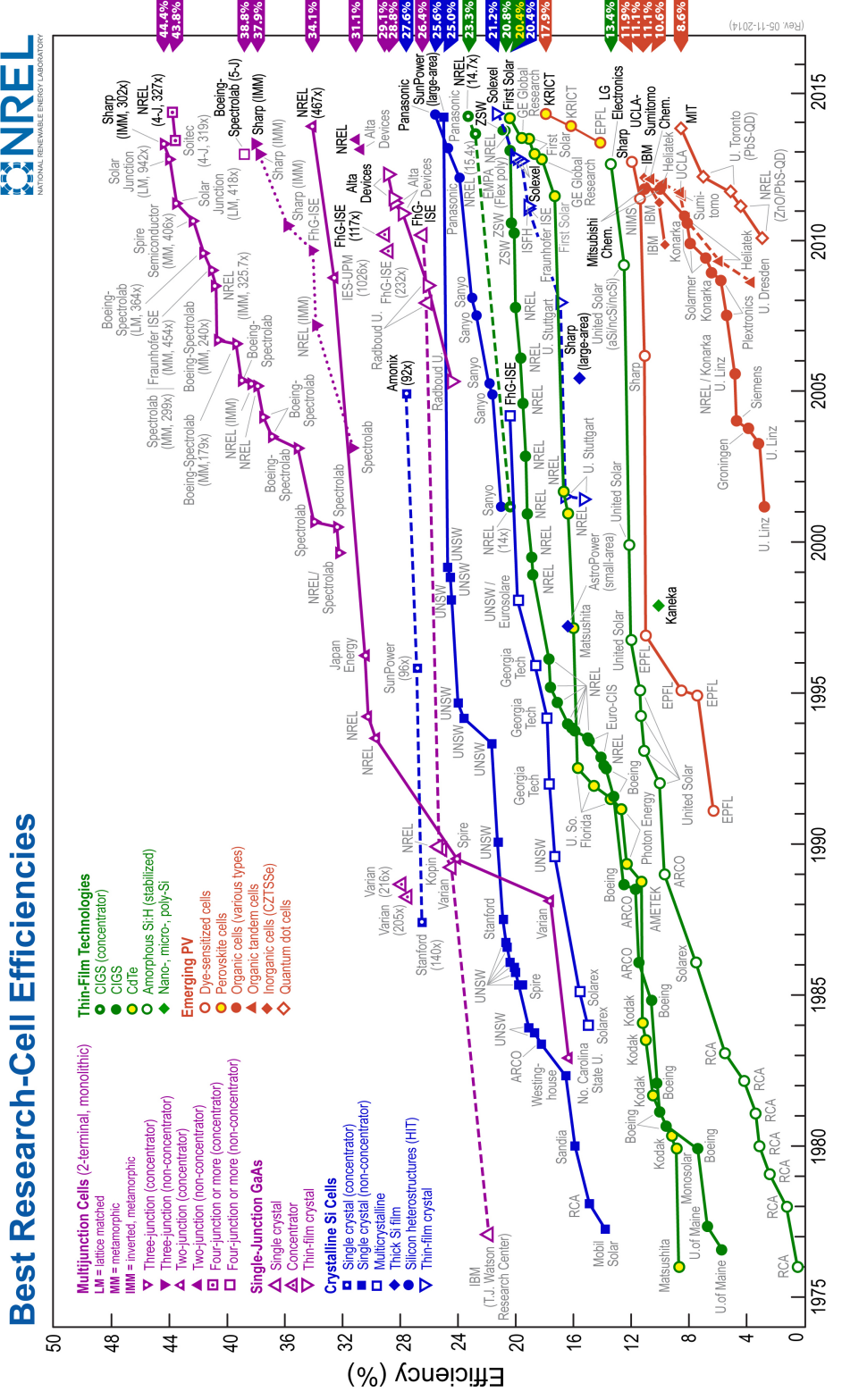


Figure 1-5: Highest recorded solar cell efficiencies, compiled by the National Renewable Energy Laboratory, USA.

1.4 Earth abundant PV

It was shown in Section 1.1 that photovoltaics is a vital component of the future energy generation mix. The desirable properties of ideal components were also shown in Section 1.2, and it was discussed that current technologies are not ideal in Section 1.3, so now the potentially sustainable alternatives can be considered.

This thesis will focus on the photoactive semiconductor component (see Figure 1-3) as this forms the basis around which the remainder of a device is constructed. The method of deployment has also been chosen to be thin-film technologies, which allow for the substitution of existing materials with new candidates as well as being the cheapest mode of PV. Indeed, several currently cheap photoactive materials exist that are being investigated to replace current, more expensive, materials.

Iron disulfide (FeS_2) was first proposed as a candidate for photovoltaics and photocatalysis in 1984.⁴⁵ FeS_2 has a band gap of 0.95 eV, large absorption coefficient and an adequate charge carrier diffusion length.⁴⁶ However, difficulties in isolating phase pure material continue to plague this field of research.⁴⁷

Similarly, Cu_2S is a potential photoabsorber with an indirect band gap of 1.21 eV,⁴⁸ a high absorption coefficient,⁴⁹ and favourable charge transport properties.⁵⁰ Unfortunately, in this case, copper ion diffusion into the contacting solid components from the absorber compound has been shown to degrade performance over time.⁵¹

The low-cost photovoltaic material probably receiving the most interest currently is $\text{Cu}_2\text{ZnSnS}_4$ (CZTS). CZTS is a quaternary chalcogenide and was introduced as a photovoltaic material in 1988 by Ito and Nakazawa.⁵² CZTS has an ideal direct band gap of 1.45 eV,⁵² high optical absorption coefficient and good charge mobilities.⁵³ The record efficiency for CZTS is an impressive 8.4 %,⁵³ but partial substitution of sulfur content

with selenium allows for an even higher light-to-electricity conversion efficiency of 12.6 %.⁵⁴ Unfortunately, this comes at increased expense due to the use of the rarer selenium.

As an alloy of Cu₂S, ZnS and SnS₂, element availability is not a concern, but controlling the component ratios can be difficult. It has been shown that the desirable phase of CZTS occupies just a small fraction of the overall phase space for the system, as shown in Figure 1-6,^{55,56} and has little or no thermodynamic barrier to phase separation.⁵⁷ Consequently, phase segregation to ternary, binary and even elementary constituents have been observed,⁵⁶ as also shown in Figure 1-6, all of which affects device performance.⁵⁸

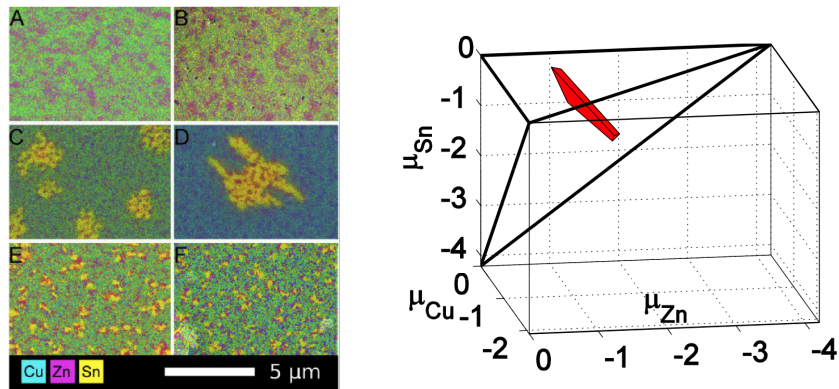


Figure 1-6: Observed phase segregation for CZTS samples (left),⁵⁸ and the phase space stability diagram of CZTS (right) with respect to chemical potential (μ). The stability region highlighted in red.⁵⁶

This thesis will consider the application of tin sulfide (SnS) for use in sustainable photovoltaics - a relatively new photovoltaic candidate. The thesis begins in earnest with subsequent assessments on the suitability of tin sulfide as a photovoltaic material, specifically with regard to deployment in second generation architectures, on the relative abundance of tin sulfide and finally on the environmental impacts of forming tin sulfide.

1.5 Photovoltaic suitability of SnS

Tin monosulfide has an optical band gap of between 1.30 eV⁵⁹ and 1.43 eV,⁶⁰ which coincides with the optimum band gap for maximum theoretical efficiency within the terrestrial solar spectrum, more so than either FeS₂ or Cu₂S discussed in the previous section.¹⁶ SnS also exhibits intrinsic *p*-type conductivity and has a higher optical absorption coefficient than CdTe ($> 1 \times 10^5 \text{ cm}^{-1}$).^{61,62} With these, among other favourable parameters observed for SnS,^{63,64} it has been shown that a single junction device ought to be able to achieve up to 24 % efficiency.^{65–67}

Besides these physical properties, SnS must be more facile to synthesise than the earth-abundant CZTS as it is itself a binary component of the quaternary material. Thus, by all preliminary measures tin sulfide is an ideal photoabsorbing PV component. However, it has been shown that there are many ways of harvesting energy from the sun, but if photovoltaics are ever to deliver a significant portion of global energy demands, one must consider more than just the semiconductor physics of a material. The cost, stability, toxicity, abundance *and* the physical suitability of components must be considered. The degree to which these terms can be applied to SnS is assessed in the following sections.

1.6 Earth abundance of SnS

The desire to break record device efficiencies has led to the use of increasingly elaborate and precise cell fabrication techniques, regardless of cost or commercial scalability. For example the record single junction cell efficiency found for any material to date is using gallium arsenide, which not only contains the expensive element gallium but the toxic element arsenic. Both of these components are expected to limit the future commercial deployment of this technology, rendering the wealth of research on this topic almost purely

academic. As such the elemental availability of SnS is subsequently discussed in order to assess the degree to which global energy demand could be met using this material.

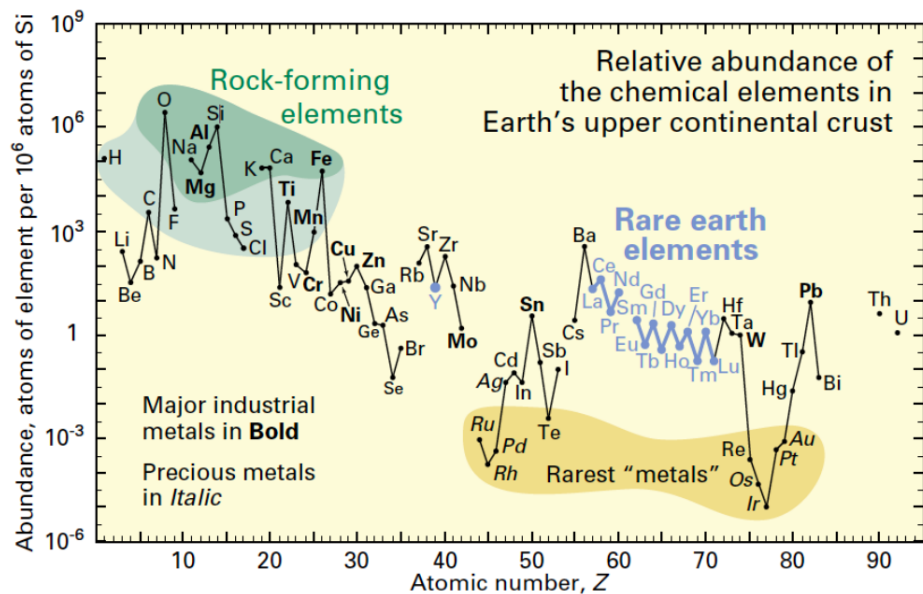


Figure 1-7: Abundance of elements in the earth’s crust relative to silicon as a function of atomic number.⁶⁸

Unlike the chalcogenides in the technologies discussed in Section 1.3 (tellurium and selenium), sulfur is known to be widely earth abundant. Figure 1-7 shows that sulfur is thought to be orders of magnitude more abundant in the earth’s crust than copper or lead, and so is not predicted to become an endangered element in the foreseeable future. However, the availability of tin in this case, is more of a concern.⁶⁹

At least one aspect of tin availability is self-evident, and that is that, unlike certain elements, tin is broadly available across geo-political boundaries. This was a key factor of bronze age civilisation development across Europe *circa* 3000 BC (bronze being an alloy of tin and copper). As such the commodity supply of tin is more robust with respect to political instability or economic turbulence, unlike, for example, localised global reserves of lithium in Bolivia or dysprosium in China.⁶⁹ This consideration has been quantified

using the so-called Herfindahl-Hirschman Index, in which tin scores more favourably than either bromine or chromium for example.⁷⁰

Not only is tin widely available but its abundance in the earth's crust is relatively high, as shown in Figure 1-7. It is estimated to be orders of magnitude more abundant than either cadmium or tellurium, for example.

In order to quantitatively assess how sustainable the use of tin sulfide in photovoltaic devices would be, the amount of tin and sulfur one would require to meet the energy demands of human civilisation is subsequently approximated.

The reported amount of energy consumed in 2011 was 12,275 million tonnes of oil equivalent.⁶ However, the approximate amount of energy that can be harvested using modern power stations is around 4,400 GWh/Mton oil.⁶ This means that the energy required to power the globe in 2011 was approximately 54,000 TWh. Given that there are 8,766 hours per year, the total annual global energy consumption was around 6.16 TW.

The earth receives around 8.85×10^8 TWh per year in solar energy from the sun.⁵ Again, given that there are 8,766 hours per year, there is 1.01×10^5 TW of energy incident to the earth. Assuming a global surface area of 5.10×10^8 km,⁷¹ the average solar energy available per meter squared is 197.96 W/m² per year. This is incredibly conservative, considering that commercial sources estimate that solar energy averages at about 1,000 watts per square meter, but is unsurprising given that this scenario considers all of the earth's surface, including the poles.

The record efficiency for a single junction device is 28.8 %,²² but commercial cells typically range between 11 - 15 %, as discussed in Section 1.3. As such it seems not unreasonable to choose 10 % as an efficiency for future SnS PV to achieve. With these hypothetical 10 % efficient cells the average energy that could be harvested would be 19.796 W/m² per year.

Continuing, it can be found that the required coverage for these model 10 % cells, given

the derived value for the average global solar radiation, would be $311,234 \text{ km}^2$, which is approximately the surface area of the Philippines or the U.S. State of New Mexico. While this may seem large at first it is in fact smaller than the estimated coverage of ‘urban’ areas of the globe in the year 2000 and a quarter of the estimated area occupied by urban areas in 2030.⁷² These growth predictions are doubly promising from a photovoltaic perspective as it is in Africa, Asia and India where the highest rates of urban growth will take place - parts of the world that are rich in available solar resource. Given that PV is suitable for deployment in existing urban environments (*i.e.* rooftop solar), it would appear that any earth-abundant cell with 10 % efficiency could make great strides towards a sustainable energy future.

Now it is possible to consider how much material one would need to meet global energy demand using tin sulfide PV alone. It was stated in Section 1.3 that thin-film cells typically use between 1 and 4 micrometer thickness of photoactive material. In order to be, again, conservative in the assumptions of this calculation, let the thickness of SnS for these hypothetical 10 % cells be $5 \mu\text{m}$. This thickness of material over the area already calculated, yields a volume of $1.556 \times 10^6 \text{ m}^3$ tin sulfide, a material with a density of $5,150 \text{ kg/m}^3$. As such $3.233 \times 10^6 \text{ kg}$ of SnS would be needed to meet the world’s energy needs, $2.545 \times 10^6 \text{ kg}$ of which is tin.

The world total tin reserves are estimated by the US geological survey to be $4.7 \times 10^9 \text{ kg}$ as of 2014,⁷³ three orders of magnitude higher than that required to power the world in this scenario. The definition of ‘reserve’ in this context being identified tin deposits which could be economically extracted or produced at the time of determination. As such it would appear that tin sulfide is indeed worthy of the title ‘earth-abundant’ and able to support global scale deployment of photovoltaic technology.

If we extend this hypothetical SnS cell to include common alternate device components, such as a molybdenum back contact, a zinc oxy-sulfide charge transport layer and

an aluminium doped zinc oxide window layer, it is possible to expand this study on materials abundance.

As of January 2012, the United States Geological Survey predicted there to be 2.5×10^{11} kg of zinc and 9.98×10^9 kg of molybdenum in known extractable reserves. Given that both of these masses are larger than that of tin, and that both zinc and molybdenum are lighter than tin (*i.e* there are more moles of atoms per given mass) we can see that such a device would be capable of making a huge contribution to a sustainable energy future before constituent element availability became of critical concern. And this scenario does not take into account PV device recycling practices that are possible even today.⁷⁴

Similar calculations have been performed for other photovoltaic materials showing that multiple PV technologies could meet global energy demands themselves, as shown in Figure 1-8.

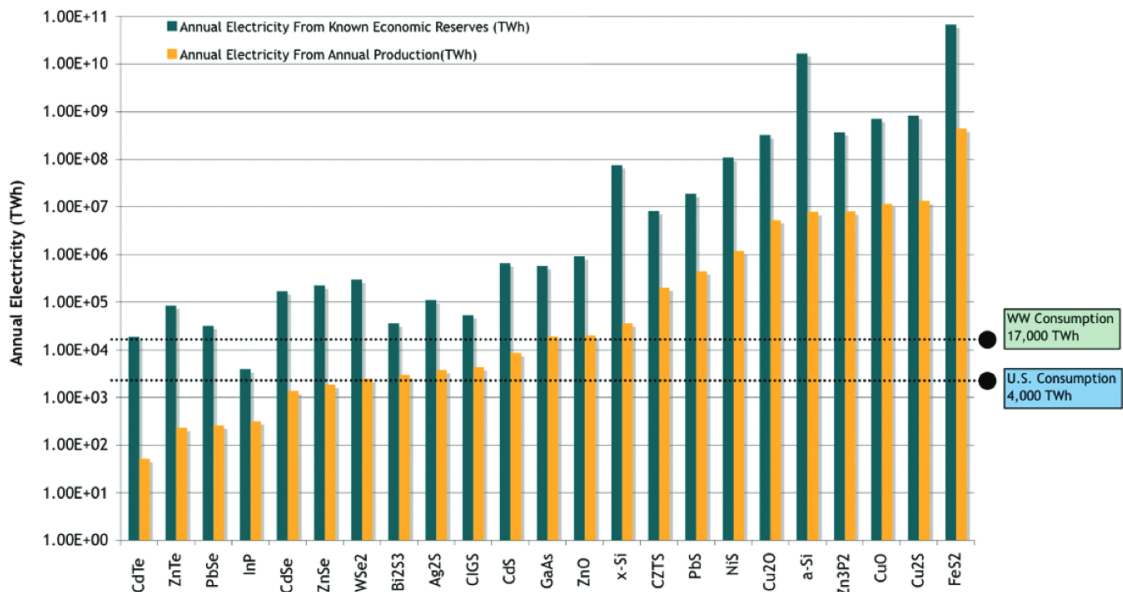


Figure 1-8: Maximum potential for deployment of alternative photoactive materials with known mineral reserves. Both band gap and optical absorption coefficient are included in the calculation of potential electricity generation.⁷⁵

1.7 Environmental impacts of SnS

It has been shown already that silicon is earth abundant (Figure 1-7) but the necessary processing for semiconductor grade crystalline silicon is an energy intensive process that is problematic with regards to device costs. As such, it is important to consider not just the relative abundance but the ease of extracting and refining tin metal, along with any relevant environmental impacts of such practices, in order to ensure that SnS would not suffer the same fate.

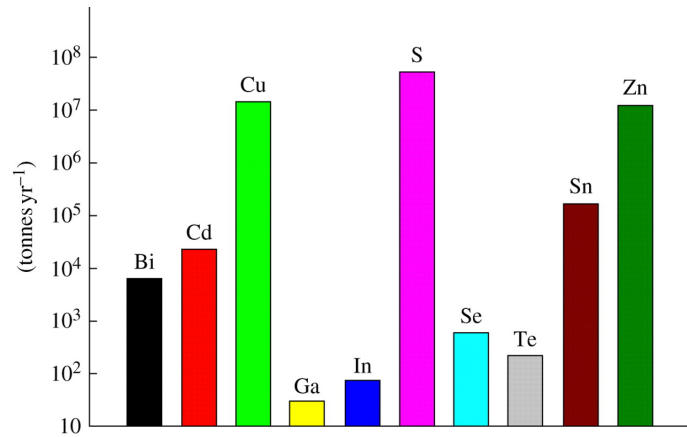


Figure 1-9: Annual production of elements important to the field of photovoltaics, reflecting the relative abundance of both sulfur and tin.¹⁵

Figure 1-9 shows recent values of annual production of some of the most common components in photo-converter materials, corroborating earlier discussions on availability and showing the production of tin is already relatively high. However, projecting future production is not quite so straightforward, for example gallium, indium and tellurium are by-products of zinc,⁷⁶ tin,⁷⁷ and copper¹⁵ extraction respectively. While indium is indeed important for PV technologies it is also a vital component of flat screen and touch screen technologies that have enjoyed massive commercial success recently. Were demand for

indium to continue to rise, it is expected that the rate of extraction of tin would increase concomitantly,⁶⁹ maintaining low-cost and high availability into the medium term future. While such predictions are difficult to quantify, there are several other assessments that can be made based on information available today.

Life cycle analysis (LCA) is an important tool for considering factors beyond availability, for example if large amounts of energy are required to extract raw tin, the time before a tin sulfide solar cell offsets its own production costs could be significant. Using SimaPro 7 software, accurate data for impacts on human health, ecosystem and materials resource for the extraction and importation of several relevant semiconductor materials was found.⁷⁸

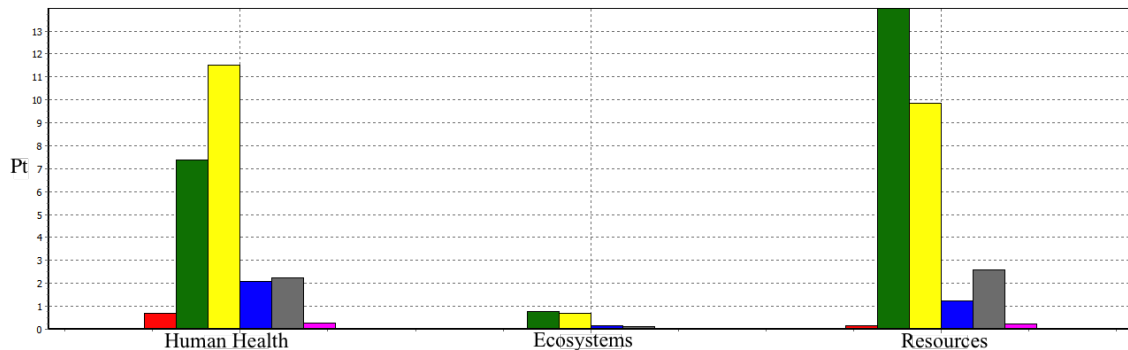


Figure 1-10: Impact analysis of commonly used PV components, where the unit 'Pt' indicates one thousandth of the yearly environmental load of an average European citizen. In order, the elements are copper in red, gallium in green, indium in yellow, molybdenum in blue, tin in grey and zinc in pink.

Figure 1-10 displays the results from the LCA analysis, comparing the various impacts of copper, molybdenum, gallium, tin, indium and zinc (where the unit 'Pt' indicates one thousandth of the yearly environmental load of an average European citizen). These elements were chosen based on relative importance to the PV industry as well as data availability within the SimaPro toolkit. It is clear from this data that tin mining and refining represents a fraction of the environmental impact of alternate elements employed by

the photovoltaics industry today.

Carbon footprints also afford a convenient parameter to compare relative energy intensiveness of industrial processes. The carbon footprint associated with the extraction and importation of 1 kg of each element is found to be 16.1 kg of CO₂ for tin; 3.17 kg of CO₂ for zinc; 8.95 kg of CO₂ for molybdenum; 145 kg of CO₂ for indium; 162 kg of CO₂ for gallium and 1.86 kg of CO₂ for copper, again showing tin to be relatively sustainable.

In conclusion, tin has an associated CO₂ footprint less than one tenth of that of gallium and is not considered critical or endangered in the medium term.⁶⁹ The environmental impacts are also relatively low and would appear to remain so for the foreseeable future. Assuming tin sulfide's potential as a PV material can be realised, the decrease in reliance on fossil fuels and rare elements should represent a great step towards reducing the impacts of society on the global ecosystem.

1.8 SnS performance to date

The ideality of tin sulfide with respect to various factors has been presented up to now, but the feature that truly defines the sustainability of SnS, *i.e.* the pay-back time for devices, is photovoltaic efficiency.

The first SnS PV device was reported in 1994 by Noguchi *et al.*,⁷⁹ where a CdS/SnS *p-n* junction was deposited on a silver contact using vacuum evaporation. The transparent conducting oxide layer was indium-tin-oxide. All of these device components and their method of synthesis are fairly standard in the field, yet the obtained efficiency of 0.29 % is incredibly low.

Spurred on by the screening studies of Dittrich *et al.*,⁸⁰ which showed that ‘sulfosalts’ were promising candidates for PV, Reddy *et al.* also created an early SnS device in 1997. This time with a recorded efficiency of 0.5 %.⁸¹ Despite this poor performance the

observed quantum efficiency (*i.e.* the probability that one photon will deliver one electron to the external circuit) was approximately 70 %, which indicates that the limiting factors correspond to issues surrounding device fabrication and are not due to tin sulfides performance as a photoactive material.

However, the progress of improvement proved incremental until the record efficiency stood at 1.3 % at the time of commencement for this project (2011).⁶¹ As of the conclusion of this work, in 2014, the record stood at a certified efficiency of 3.88 %.⁸²

Thus, the crux of this research project is revealed. Sections 1.5 - 1.7 showed how by all accounts SnS ought to be ideal for photovoltaic applications, yet the record device efficiencies loosely correspond to those of silicon in the early 20th century. The subsequent sections of this thesis will investigate various possible origins of this anomalous behaviour.

1.9 Potential flaws of SnS

The previous discussions have shown the ideality of pure tin sulfide for PV applications but that obtained device efficiencies have been remarkably low. There are multiple possibilities as to the origin of these low efficiencies for SnS, perhaps the likeliest of which is the formation of the alternate phases of SnS that may be less than ideal for PV applications. Indeed, there is evidence of this occurring, Figure 1-11 shows an example of an X-ray diffraction pattern performed on a film of SnS that shows traces of Sn_2S_3 formation,⁸³ and it has even been shown that pre-purchased ‘SnS’ powder contains up to 55 % Sn_2S_3 by weight.⁸⁴

Evidence for the presence of phase impurities in CZTS has already been shown (see Section 1.4), however the record efficiencies for this material are more than twice those for SnS. As such, besides the issues relating to the accessible locations of the sulfur - tin phase diagram, one must also consider alternate efficiency loss mechanisms.

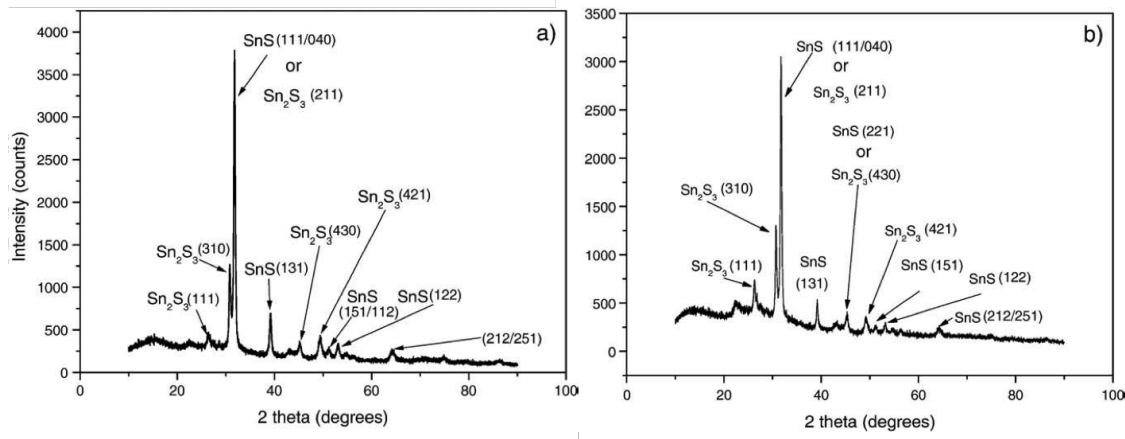


Figure 1-11: Example X-ray diffraction pattern of a thin-film showing mixed phases of tin sulfide.⁸³

The possibility of spontaneous and irreversible reaction with oxygen is well-known. Not only are SnO_2 and SnO known to exist but three tin sulfate compounds are also thought to be stable. Even still, externalities such as O_2 or moisture exposure are possible to minimise, and presumably the tin in CZTS would oxidise in a similar way.

It is possible that chemical reactions occur between the SnS and alternate device components. A ‘detrimental’ reaction has been observed between a deposited film of CZTS and a molybdenum back contact, forming layers of MoS_2 , and still the efficiencies of CZTS routinely obtained in a lab are much higher than the best performance of SnS . While not all reactions are expected to be deleterious to photovoltaic performance, it is expected to be a source of major discrepancies in performance between two different devices.

It is also possible that cation migration can limit performance, which was found to be the case for almost all Cu_2S devices as discussed in Section 1.4.⁸⁵ Once again, it would be seem that if this were the case for SnS , why not CZTS, given that it contains copper ions as well as tin?

This research project aims to perform an in-depth analysis of tin sulfide by combin-

ing high-quality experiment and computation. It is hoped that greater understanding of this material could unlock a new sustainable candidate for large-scale photovoltaics and improve knowledge in the wider field of sustainable PV.

1.10 Thesis structure

This thesis describes a joint theoretical and experimental project and contains three research results chapters. Each chapter lists results obtained on single crystals of phase pure tin sulfide and density functional theory simulations on corresponding perfect, infinite solids. These are compared with alternate findings in the literature throughout and followed by a discussion section to conclude each chapter.

The first chapter contains the synthesis conditions and relative energies of the obtained phases of tin sulfide with respect to various conditions, in order to evaluate the chemical stability of SnS. The second chapter details studies on the opto-electronic properties of tin monosulfide, sesquisulfide and disulfide in order to ascertain whether the presence of alternate phases might adversely affect photovoltaic performance. The final results chapter investigates the intrinsic defects and transport properties of SnS to better understand the behaviour of tin sulfide inside a working photovoltaic device.

This thesis concludes with a discussion of the important results found over the course of this three-year project and suggestions for future work, in order to carry these conclusions forward.

Chapter 2

Methodology

This chapter details both the methods of synthesising single crystal tin sulfide phases and the methods of deriving calculated properties.

2.1 Experimental methods

The following section describes the experimental methods used to synthesise tin monosulfide (SnS), tin sesquisulfide (Sn_2S_3) and tin disulfide (SnS_2), using chemical vapour transport.

2.1.1 Single crystal growth

Thin-films of SnS have been formed by many different deposition techniques,^{63,86–93} but single crystals of tin monosulfide have only been grown previously by the BridgmanStockbarger,⁹⁴ or chemical vapour transport method.⁹⁵ The method chosen to create phase-pure single crystals in this project was chemical vapour transport (CVT), a method first proposed in 1957 as a way to vaporise a metal at relatively low temperatures by forming a

volatile chemical intermediate.⁹⁶ CVT involves placing the elemental components of the desired crystal compound in a sealed and evacuated quartz ampoule along with a carrier agent and then subsequently enforcing a temperature gradient across the ampoule, providing the driving force for the crystal formation.

For tin, iodine has been shown as an optimum carrier agent,⁹⁷ and also been successfully used in the synthesis of CZTS single crystals.⁹⁸ As such, to synthesise tin sulfide, tin (> 99 % powder, Aldrich) and stoichiometric amounts of sulfur (> 99.999 % pieces, Puratronic, hand crushed with an agate pestle and mortar) were placed in silica ampoules that are 15 cm in length and 2 cm in diameter. Iodine (99.999 % pieces, Aldrich) was placed in the same ampoule, in quantities corresponding to the 5 mg cm³ as recommended by Nitsche *et al.* to deliver the solid more slowly than the rate of crystal growth.⁹⁷

The ampoule was then evacuated under the effect of liquid nitrogen in order to prevent the I₂ from evaporating under vacuum. Prior to ampoule evacuation, all components were exposed to air and the associated content thereof, which represents a potential source of impurities, for example, oxidation or the inclusion of moisture. Care was taken when considering net mass of components, as ampoule explosions were known to occur upon heating.

The apparatus itself consisted of a horizontal tubular furnace (Elite Thermal Systems Ltd.) with four independently controlled zones within the furnace. The applied temperatures were chosen to be greater than the boiling point of the carrier phase, in order for it to be gaseous, but below the boiling point of the desired crystal, in order for it to crystallise. Given that the boiling point of tin iodide is 348 °C and that of tin monosulfide is approximately 1230 °C,⁹⁹ a large scope of temperature gradients is possible for this method.

The temperatures of the individual furnace zones were chosen after calibration with a thermocouple drawn along inside of the furnace, such that the desired gradient was

obtained across the length of the ampoule, as shown in Figure 2-1. During the experiments the ampoule was in contact with the alumina work tube of 30 mm internal diameter that constituted the wall of the furnace, with end plugs for the furnace made of ceramic fibre.

A schematic representation of the system used in this project and the chemical processes that this induces is also included in Figure 2-1, showing that tin is consumed at high temperature and migrates as tin iodide towards the cooler end of the ampoule where the tin sulfide forms and releases the iodine. Concentration causes diffusion of I_2 back towards the tin creating a cycle.

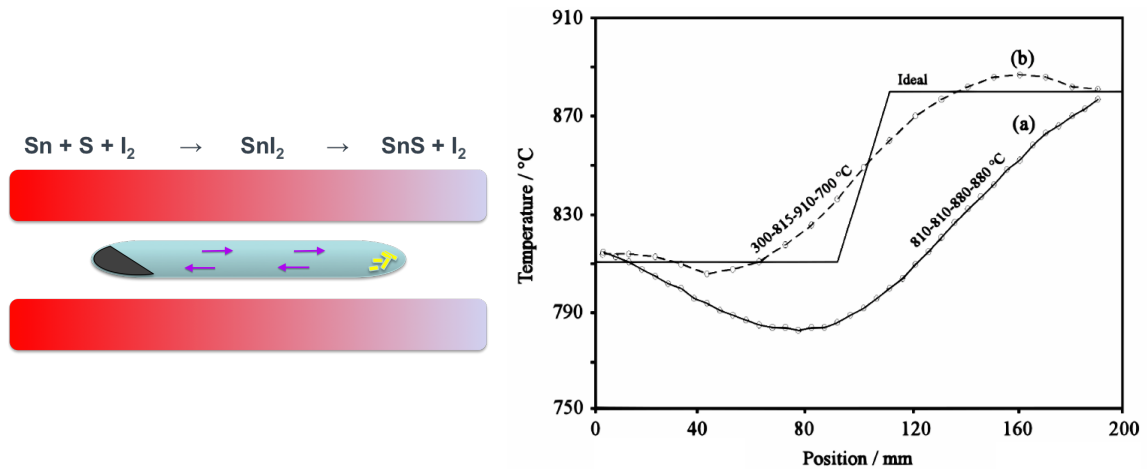


Figure 2-1: Schematic of the chemical process induced by CVT (left), with red and blue showing higher and lower temperatures, respectively. The crystals are in yellow and the solid components black. A sample temperature profile along an ampoule at an unrefined (a) and a refined stage (b) of adjustment is also shown (right), compared to a desired condition.⁹⁸

2.2 Theoretical methods

In this section the first principles methods used to analyse and predict semiconductor properties are discussed.

2.2.1 *Ab initio* calculations

Almost all methods of *ab initio* electronic structure calculations will follow a procedure similar to that shown in Figure 2-2, which is the implicit methodology behind all of the theoretical results discussed in this thesis. The subsequent discussions contain the numerical methods of performing each of the decision components of this work flow.

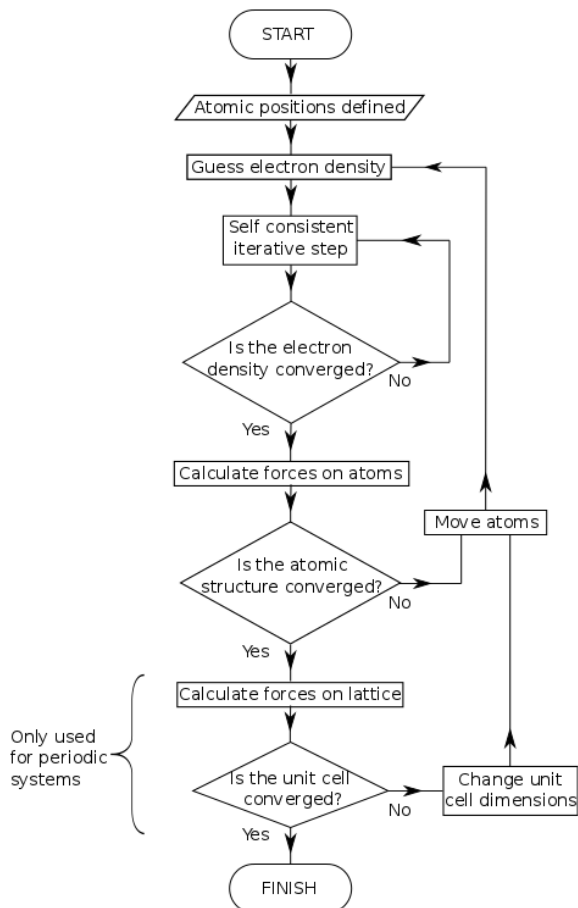


Figure 2-2: Representative flow chart of an *ab initio* calculation process. For a solid-state calculation the input is the crystal structure and the output is the total energy and ground state properties of the material.

2.2.2 Electron density convergence

As can be seen in Figure 2-2 the first step in completing an *ab initio* calculation is arriving at a converged electron density. The resulting solution is unique to a given level of theory and will lead to different structure and property predictions between them. In this thesis Hartree-Fock theory, density functional theory and hybrid methods will be considered as procedures for converging the spatial arrangement of electrons.

2.2.2.1 The Schrödinger Equation

Virtually all of chemistry depends on the behaviour of electrons, as such it has long been the goal of science to describe and predict this behaviour. A wave function (Ψ) is a description of an electron that allows for its quantum properties to be detailed. In 1926 Erwin Schrödinger proposed a way of relating an electron wave function to its physical environment, known as the Schrödinger equation:

$$\hat{H}\Psi(r_i, r_I, t) = E\Psi(r_i, r_I, t) \quad (2.1)$$

where \hat{H} and E are the Hamiltonian operator, containing all of the energy terms for a system, and system energy respectively. The variables r_i and r_I are the coordinates of the electron and nucleus, again, respectively and t is time. Unfortunately this equation can only be solved analytically for one electron. Thus to derive the properties of anything beyond a hydrogen atom, an approximate solution to the Schrödinger equation must be found.

Firstly, it is possible to neglect time, as the desired solution to the Schrödinger equation is the lowest energy (*i.e.* ground state) configuration of Ψ , which is constant in time. This is known as the ‘adiabatic approximation’.¹⁰⁰ Secondly, it is possible to neglect the effects

of gravity and relativity given the infinitesimal mass of an atom and that the velocities of a typical electron in a (*e.g.* hydrogen) atom are less than 1 % the speed of light.^{101,102} For heavy elements such as europium, relativity must be accounted for, but this does not impact on this study.

Now the wave function depends only on the electronic and nucleic coordinates, r_i and r_I , becoming

$$\hat{H}\Psi(r_i, r_I) = E\Psi(r_i, r_I) \quad (2.2)$$

where the components of the Hamiltonian operator are the kinetic energies of the nuclei (T_I) and electrons (T_i), and the potential energies for nucleus-electron (U_{Ii}), electron-electron (U_{ij}) and nucleus-nucleus (U_{IJ}) interactions

$$\hat{H} = T_I + T_i + U_{Ii} + U_{ij} + U_{IJ} \quad (2.3)$$

Furthermore, when one considers that neutrons and protons are each around 2,000 times more massive than an electron,¹⁰³ it is possible to see that were a nuclei to move, the electrons would respond almost instantaneously and always occupy the ground state of that given nuclear configuration. Born and Oppenheimer proposed therefore, that the positions of the nuclei could be considered constant,¹⁰⁴ effectively decoupling the nuclear and electronic dynamics and leading to:

$$\hat{H} = T_i + U_{Ii} + U_{ij} \quad (2.4)$$

The kinetic energy term for n electrons is given as

$$T_i = -\frac{\hbar^2}{2m_e} \sum_i^n \nabla_i^2$$

where m_e is the mass of an electron and \hbar is the reduced Planck constant. ∇_i^2 is called the ‘Laplacian operator’ and is the divergence of the gradient of the position of n electrons in Cartesian space:

$$\nabla_i^2 = \frac{\delta^2}{\delta x^2} + \frac{\delta^2}{\delta y^2} + \frac{\delta^2}{\delta z^2}$$

The second term of the Hamiltonian (Equation 2.4) describes the attraction of n electrons due to N nuclei

$$U_{Ii} = - \sum_I^N \sum_i^n \frac{Z_I}{|r_{Ii}|} \quad (2.5)$$

where Z_I is the charge of the nuclei.

The third term in Equation 2.4 is the repulsion of the n electrons to each other

$$U_{ij} = \frac{1}{2} \sum_{i \neq j}^n \frac{1}{|r_{ij}|} \quad (2.6)$$

and covers all cases where $i \neq j$ to exclude self interaction, with the factor $1/2$ correcting for double counting.

Substituting in all these terms, the Hamiltonian operator, \hat{H} , of Equation 2.2 is now given by

$$\hat{H} = -\frac{\hbar^2}{2m_e} \sum_i^n \nabla_i^2 - \sum_I^N \sum_i^n \frac{Z_I}{|r_{Ii}|} + \frac{1}{2} \sum_{i \neq j}^n \frac{1}{|r_{ij}|} \quad (2.7)$$

However, even in this simplified form, solving the Schrödinger equation is too demanding for systems where the number of electrons is greater than one, due to the electrostatic term for the electron-electron interaction. This is called the many body problem and is a major obstacle considering that virtually all systems of interest have a large number of

quantum bodies to be described. Consequently, further assumptions must be made.

2.2.2.2 Describing the many body wave function

To describe a system of many bodies, their full quantum behaviour must be accounted for. Electrons belong to a class of elementary particle called ‘fermions’. These particles are characterised as having a half-integer spin, and obeying the Pauli exclusion principle that forbids them from occupying the same quantum state.¹⁰⁵ As a result, the total wave function must be anti-symmetric with respect to the exchange of particles, *i.e.* the wave function reverses sign if the space and spin co-ordinates of any two particles are interchanged. That is to say

$$\Psi(x_1, x_2, \dots, x_i, \dots, x_j, \dots, x_n) = -\Psi(x_1, x_2, \dots, x_j, \dots, x_i, \dots, x_n) \quad (2.8)$$

where x accounts for both position and spin r, s .

It is possible to find a many body wave function for a system if the electrons are treated as if they do not interact with each other. The Hamiltonian for such a system of n non-interacting electrons is

$$\hat{H} = \sum_{i=1}^n h(i) \quad (2.9)$$

where $h(i)$ is the operator describing single electron kinetic and potential energies.

The single electron Schrödinger equation can be solved to obtain a set of single electron spin orbitals (χ).

$$h(i)\chi(x_i) = E\chi(x_i) \quad (2.10)$$

Now the many body wave function of the system can be written as

$$\Psi(x_1, x_2, \dots, x_n) = \frac{1}{\sqrt{n!}} \begin{bmatrix} \chi(x_1) & \chi(x_1) & \cdots & \chi(x_1) \\ \chi(x_1) & \chi(x_1) & \cdots & \chi(x_1) \\ \vdots & \vdots & \ddots & \vdots \\ \chi(x_n) & \chi(x_n) & \cdots & \chi(x_n) \end{bmatrix} \quad (2.11)$$

which is known as a Slater determinant.¹⁰⁶ It satisfies the Pauli exclusion principle (Equation 2.8) as exchanging two rows yields a change in sign of the determinant, and if any two rows are equal the determinant is zero.

A single Slater determinant is used as an approximation to the electronic wave function in the first widely successful method of solving the Schrödinger equation: Hartree-Fock theory.

2.2.2.3 Hartree-Fock theory

While in principle the only information required to solve the Schrödinger equation is a species' atomic number and spatial coordinate, the equation is too complex to solve for anything beyond a one electron system. Several approaches can be employed to make the problem manageable; the first of which to be broadly implemented was the Hartree-Fock theory (HFT).

Hartree-Fock calculations rely on what is known as the ‘variational principle’, that is to say that a guess or ‘trial’ electron density determines a trial Hamiltonian and wave function (Ψ_t) with an energy greater than or equal to that of the ground state. As such, the electron density that results in the lowest energy is the desired ground state density.

To arrive at this density in HFT, the single-particle wave functions (χ) of a Slater determinant (Equation 2.11) are varied individually to find an electron density iteratively.¹⁰⁷ This method is called the self-consistent field (SCF) method and conceptually corresponds

to each electron interacting with the mean field of the other electrons in the system. In this way HFT allows for the computation of a converged electron density necessary for the archetypal *ab initio* calculation shown in Figure 2-2.

Significantly, the use of anti-symmetric single electron wave functions in this method introduces a term that accounts for the interaction felt between electrons of the same spin. This is called the exchange energy and yields:

$$U_{ij} = U_{ij}^H + U_{ij}^X \quad (2.12)$$

where U_{ij}^H is the Hartree potential that describes the Coulomb interaction between electrons i and j , of the form

$$U_{ij}^H = \sum_{j=1}^n \int \frac{|\chi_j(r')|^2}{|r - r'|} dr' \quad (2.13)$$

and U_{ij}^X is the exchange potential

$$U_{ij}^X = - \sum_{j=1}^n \chi_j(r) \int \frac{\chi_j^*(r') \chi_i(r')}{|r - r'|} dr' \quad (2.14)$$

In the Hartree-Fock method this exchange energy is formally exact; however, there is no description of the interactions between electrons of different spin, the so-called correlation energy. Fortunately there are alternate methods that allow for correlation to be accounted for.

2.2.2.4 Density functional theory

Density functional theory (DFT) is an alternate method of solving the Schrödinger equation that has enjoyed massive success in recent years. It is based on a proof theorem put forward by Hohenberg and Kohn in 1964,¹⁰⁸ which states that the total energy, including

both exchange and correlation energies, of an electron gas is a unique functional of the electron density. The minimum value of this functional yields the ground state energy, and the corresponding density is the exact single electron ground state density.

Unfortunately, while Hohenberg and Kohn were able to provide this proof, they were not able to outline a suitable method for implementation. Kohn and Sham would later provide a pathway to making such calculations possible in 1965.¹⁰⁹

The Kohn-Sham method

Kohn and Sham approached the problem by decomposing the density of an n -electron system into that of n non-interacting electrons. This yields so-called Kohn-Sham orbitals ($\chi_i(r)$) that are solutions to the Schrödinger equation

$$\left[-\frac{1}{2} \nabla^2 + U_{eff}(r) \right] \chi_i(r) = \varepsilon_i \chi_i(r) \quad (2.15)$$

Here ε is the energy corresponding to the Kohn-Sham orbital and U_{eff} is a unique effective potential with a ground state charge density $\rho(r)$

$$\rho(r) = \sum_{i=1}^N |\chi_i(r)|^2 \quad (2.16)$$

In DFT the total energy of an interacting system is given as

$$E_{tot}[\rho(r)] = T_i[\rho(r)] + E_H[\rho(r)] + E_{xc}[\rho(r)] + \int U_{Ii}(r) \rho(r) d(r) \quad (2.17)$$

Here the notation $[\rho(r)]$ is used to show that a term, for example, the energy functional E , is a function of electron density, ρ , which is itself a function of location, r .

The kinetic energy functional is given by

$$T_i[\rho(r)] = -\frac{\hbar^2}{2m_e} \sum_i^n \chi_i(r) \nabla_i^2 \chi_i(r) dr \quad (2.18)$$

and the electrostatic or Hartree functional is

$$E_H[\rho(r)] = \frac{e^2}{2} \int \int \frac{\rho(r)\rho(r')}{|r-r'|} dr dr' \quad (2.19)$$

The $E_{xc}[\rho(r)]$ term is the exchange correlation functional and contains all of the unknown interaction terms. For this case, as well as exchange and correlation, the interacting component of the kinetic energy is also unknown, as the $T_i[\rho(r)]$ (Equation 2.18) is derived from the non-interacting Kohn-Sham orbitals $\chi_i(r)$ and not the electron density.

The wave functions that minimise the energy functional (Equation 2.17), are provided by Equation 2.15, in which

$$U_{eff} = U_{iI} + U_{ij}^H + U_{ij}^{xc} \quad (2.20)$$

where U_{ij}^{xc} is $\delta E_{xc}[\rho(r)]/\delta\rho(r)$.

In this way it is possible to map a system of interacting particles onto a system of non-interacting particles with the same charge density. Thus a relatively high level of accuracy is obtained for a relatively low computational cost.

All of these equations are solved self consistently in the same manner as the HFT method; however, as already stated, the $E_{xc}[\rho(r)]$ functional is not yet known. Fortunately, it is possible to approximate this term in order to find a solution to this method. This is fortuitous as, while this term typically accounts for less than 10% of the total energy, it is actively involved in determining materials properties.¹¹⁰

Local Density Approximation

All of the terms of the energy functional are now known apart from the exchange correlation (XC) functional, however, it is possible to obtain an exact XC energy functional for a homogeneous electron gas.^{111,112}

The local density approximation (LDA) is a method that assumes that the exchange-correlation energy per electron at a point r in a system is equal to the exchange-correlation energy per electron in a homogeneous electron gas of the same density (ϵ_{xc}^{hom})^{113–115}

$$E_{LDA}^{xc}[\rho] = \int \rho(r) \epsilon_{xc}^{hom}(\rho(r)) dr \quad (2.21)$$

The LDA reproduces materials properties well, even for homogeneous systems where the electron density does not resemble that of a homogeneous electron gas. The success of the LDA can partly be attributed to the fact that some of the errors involved in the XC energy are systematically cancelled, *i.e* the correlation energy is underestimated and the exchange energy is overestimated. However, one notable problem experienced with LDA calculations is that the binding energies between atoms is overestimated with respect to experiments and can lead to incorrect results for ground state structures, leading to flaws in associated property predictions.

Generalised Gradient Approximation

It is possible to generate more accurate XC functionals by treating both the local and semi-local density information; this is known as the generalised gradient approximation (GGA) and means that the gradient of the electron density at a given point in space is also accounted for.

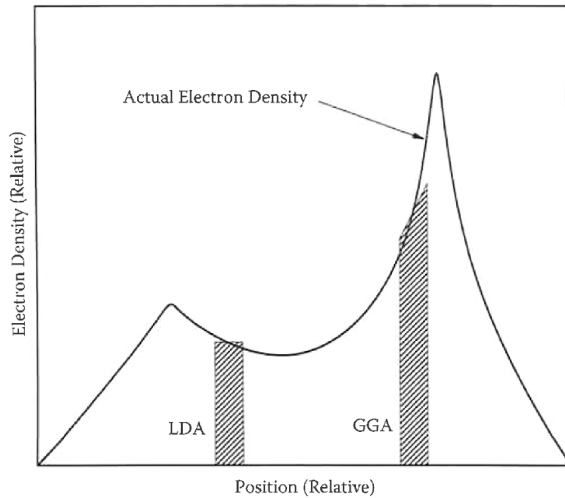


Figure 2-3: Schematic representation of the LDA and GGA treatments of electron density, showing the increased accuracy of GGA due to the inclusion of the density gradient.¹¹⁰

$$E_{GGA}^{xc}[\rho] = \int \rho(r) \epsilon_{xc}^{GGA}(\rho(r), \nabla \rho(r)) dr \quad (2.22)$$

Therefore GGA is LDA with density gradient as an additional variable and is able to retain LDA's analytic properties.¹¹⁶ This higher level of treatment can be seen from the schematic shown in Figure 2-3.

In general for non-metallic systems, GGA based calculations tend to reproduce the key properties of real systems, such as atomic structure, with a greater degree of accuracy than LDA. The overestimated binding energies observed in the LDA are corrected for within GGA and the band gaps of materials are reported with improved accuracy.¹¹⁰

While within the LDA there is an exact form of the XC potential, within the GGA the XC energy has been fitted by a number of analytic forms.^{117,118} The one chosen for use in this work is that of PBEsol,¹¹⁹ unless otherwise stated. The PBEsol functional was specifically developed to describe electron exchange in solids and surfaces and is an empirically modified version of the successful Perdew, Burke and Ernzerhof (PBE)

functional.

With an exchange correlation functional identified, we now have all constituting terms for the total energy functional (Equation 2.17) that allows us to converge an electron density for an *ab initio* calculation (Figure 2-2).

2.2.2.5 Hybrid functionals

We saw previously that HFT describes electron exchange exactly but discounts correlation, while DFT treats both exchange and correlation by approximation. This led Becke^{120,121} to conclude that a fraction of the exchange energy evaluated using HFT, mixed with DFT GGA exchange and correlation would improve the overall accuracy of a calculation. Such a hybrid calculation takes the form

$$E_{hyb}^{xc}[\rho] = E_{HF}^x[\rho] + \alpha(E_{GGA}^x[\rho] - E_{HF}^x[\rho]) + E_{GGA}^c[\rho] \quad (2.23)$$

where α is an empirically derived coefficient to describe the degree of splicing of the HFT and GGA methods. In particular the value of α is chosen to be 0.25 for the inclusion of screened HF exchange in this project.

The functional developed by Heyd, Scuseria, and Ernzerhof (HSE06) for hybrid calculations is the chosen method of electronic structure calculations in this thesis.¹²² For solid state materials this method has shown to be among the most accurate methods available, even more so than higher levels of theory.¹²³ However, the computational expense of this method is orders of magnitude larger than the previously discussed HFT or DFT.

2.2.3 Atomic position convergence

Up to now all methods discussed have aimed to converge the electron density to the ground state configuration for a given nuclear coordinate. However there will be an overall energy

minimum with respect to both electronic *and* nucleic configuration for a given level of theory. This is the second iterative loop of the typical *ab initio* calculation shown in Figure 2-2.

To find this ground state atomic arrangement, the forces acting on each ion are calculated after each electronic minimisation and the ions are driven down the force vector before a subsequent electronic iterative convergence calculation is again performed. After successive minimisation of electronic and atomic energies the system will reach its minimum energy configuration and stop once the forces acting on each atom reach below a predefined criterion.

2.2.3.1 Hellman-Feynmann theorem

Forces on atoms arise from both atomic and electronic sources and the Hellman-Feynman theorem provides an efficient way to account for them that is computationally accessible.^{124,125}

The theorem states that, if an exact Hamiltonian \hat{H} and the corresponding wave function Ψ are calculated, the force on an atom (F_I) is the expectation value of the partial derivative of \hat{H} with respect to atomic position r_I . Since only two potential terms are related to r_I , the theorem leads to

$$F_I = -\frac{dE}{dr_I} = -\frac{\delta U_{IJ}}{\delta r_I} - \int \frac{\delta U_{Ii}}{\delta r_I} \rho(r) dr \quad (2.24)$$

Therefore, after taking an electronic iteration, the forces can be calculated by performing simple derivative operations. Based on these calculations, it is possible to direct atoms down a potential energy gradient and identify the overall ground state configuration, with relative computational ease.

While either HFT, DFT or hybrid methods can be used in conjunction with this geo-

metric minimisation, it is important to note that for hybrid calculations, in this project, the atomic configuration is pre-relaxed at the DFT level described. This is due to the excessive computational cost of the HSE06 method.

2.2.4 Periodicity of solids

The methods discussed in the previous sections of this chapter are trivially applicable to molecules or atoms in free space. However, solids will typically contain of the order of 10^{23} quantum particles that define bulk properties and observed behaviour. This is orders of magnitude too large to calculate at the levels of theory discussed in this thesis. Fortunately, solids are characterised by a repeating periodic arrangement of atoms. If we assume that a solid is perfect, it is possible to treat it as a repeating infinite unit cell structure using periodic boundary conditions. The most common method of implementing this in *ab initio* methods is using plane wave basis functions.

2.2.4.1 Plane wave representation

Atoms in most solids are arranged in a periodically repeating pattern, as such, any quantity of interest that depends on position (r) will be periodic as well. For example, a given potential (U) acting on electrons will be invariant under translation with respect to the unit cell length (R) *i.e.*

$$U(r) = U(r + R) \quad (2.25)$$

where $R = nx + ny + nz$ (n is an integer and x, y and z are the unit cell vectors). Similarly, the electron density in a solid is also periodic as it too depends on position

$$\rho(r) = \rho(r + R) \quad (2.26)$$

Bloch realised that the electrons in a solid retain the form of a propagating free electron, differing only by a periodic modulation associated with the ionic positions,¹²⁶

$$\Psi(r) = Ce^{ik \cdot r} \quad (2.27)$$

in which C is the potential of the atom core and k is the wave vector (where crystal momentum is $p = \hbar k$). Bloch mapped the same plane waves onto the structurally repeating pattern of a solid and made the wave functions quasi-periodic with the introduction of a periodic cell potential $u_k(r)$.

$$\Psi_k(r) = u_k(r)e^{ik \cdot r} \quad (2.28)$$

where $u_k(r)$ has the same periodicity as the potential.

The wave function can now be written

$$\Psi_k(r+R) = u_k(r+R)e^{ik \cdot (r+R)}\Psi_k(r)e^{ik \cdot R} \quad (2.29)$$

In this way all relevant entities such as wave functions, potential, electron densities or energies can be expressed in periodic form. Thus we arrive at the final iteration check of the *ab initio* calculation procedure of Figure 2-2, as the periodic boundaries of a model solid can be varied to allow greater degrees of freedom in the geometric relaxation stage.

2.2.4.2 Pseudo-potential approximation

Almost all solid state *ab initio* codes implement periodic boundary conditions, but employed methods of approximating the potentials for these are where simulation packages differ.

It is possible in materials simulations to account for all electrons with numeric atom-

centred orbitals, as does the Fritz Haber Ab Initio Molecular Simulations Package (FHI AIMS) code used in this thesis. However, this is computationally quite expensive and not practical with plane waves, as it requires too many to describe wave function oscillations close to the nuclei.

A simplification of this method is to approximate atoms as having bound ‘core’ electrons and free ‘valence’ electrons. The core electrons contribute little to chemical bonding or observed materials properties but still would require wave functions to describe them correctly. To avoid this, core electrons are represented by pseudo-potentials, which represent the long-range interactions of the core and produce pseudo-wave functions outside of the core. Within the core the pseudo-potential is as uniform as possible, thus significantly reducing the number of plane waves required and reducing the computational load.

The Vienna Ab Initio Simulation Package (VASP) code used in this project employs the so-called projector-augmented wave (PAW) potentials. These were first proposed by Blöchl,¹²⁷ to map both core and valence wave functions with separate descriptions.

The Ψ_{inter} of the valence part is represented with a plane wave expansion (see preceding section), while the Ψ_{core} of the core part is projected on a radial grid at the atom centre. After the addition of these two terms, the overlapping part Ψ_{net} , is subtracted to make the final wave function Ψ_{PAW}

$$\Psi_{PAW} = \Psi_{inter} + \Psi_{core} - \Psi_{net} \quad (2.30)$$

Owing to the use of the core wave function, the overall complexity is reduced while still allowing for a high level of accuracy.

2.3 Methods comparison & discussion

In this chapter it was shown how, via a series of applicable assumptions, it is possible to simulate a perfect bulk system in its ground state crystal structure. Such a perfect solid is most closely analogous to single crystals, sought by CVT in this case, where the system is allowed to adopt its preferred structure, not subject to any epitaxial strain or confinement effects that may be present in thin-films or nanoparticles. As such, the results presented in the remainder of this thesis are considered directly comparable, whether they be derived by spectroscopy or mathematical transformation. It is expected therefore, that as well as allowing for the identification of likely efficiency loss mechanism for SnS in PV applications, it is also possible to comment on the suitability of either method, especially when compared with the results presented in the literature for this system.

Chapter 3

Single crystal synthesis & thermodynamic properties

This chapter begins with the identified and optimised routes for synthesising the single crystals of SnS, Sn_2S_3 and SnS_2 , as these crystals will form the basis of much of the discussion in the remainder of this thesis. Subsequently, the density functional theory calculations performed to obtain relevant physical parameters are presented. It will be shown that these calculations yield complementary results that aid in the consideration of the observed behaviours of the synthesised crystals and help derive important conclusions regarding tin sulfide.

3.1 Single crystal growth & characterisation

It was shown in Chapter 2 that the ability to extract physically meaningful properties from *ab initio* calculations depends upon arriving at a ground state configuration with respect to both electronic and ionic coordinates. Consequently, only the three ground state phases of

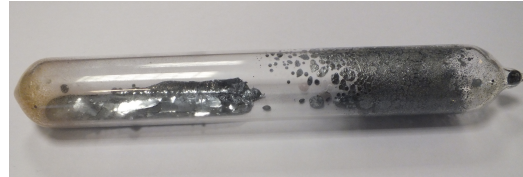
the tin sulfide system were sought in single crystal synthesis.

The established conditions for optimal crystal growth are listed in Table 3.1, corresponding to the stoichiometric amounts of solid reagents with examples of resultant crystals shown in Figure 3-1. These conditions agree well with the work of others,⁹⁵ and imply that to obtain phase pure SnS, one must rapidly cool the reaction in order to escape the lower temperature gradients required to synthesise the competing phases, *i.e.* prevent phase dissociation. Indeed, rapid quenching of SnS below 650 °C was a technique employed by Lambros *et al.* in their isolation of “almost perfect” crystals.¹²⁸ As a result, SnS has only been obtained as a smooth, black crystal of poorly defined morphology in this project, as it is quickly cooled from a temperature greater than its melting point.

Table 3.1: Reaction conditions required to synthesise the separate phases of tin sulfide.

Phase	Temperature difference (°C)	Mass of tin (g)	Mass of sulfur (g)	Time
SnS	850 - 950	1.579	0.427	10 days
SnS ₂	600 - 950	1.691	0.897	12 days
Sn ₂ S ₃	500 - 650	1.781	0.723	10 days

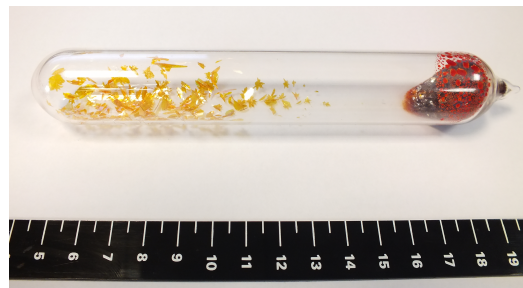
The crystal structure for each of the phases was confirmed with X-ray diffraction (XRD). For Sn₂S₃ and SnS₂ single-crystal diffraction was possible, which confirmed the ground state *Pnma* structure of Sn₂S₃ with structural parameters in agreement with previous reports.¹²⁹ For SnS₂ an extended *R*-3 polytype was identified, which is closely related to the known ground state *P-3m1* phase but with an AAB layer stacking.¹³⁰ The ill-defined morphology of bulk SnS, resulting from the rapid cooling process from above its melting temperature, was not conducive to single-crystal diffraction; however, powder diffraction pattern of a ground sample resulted in the expected *Pnma* phase.¹³¹ The powder diffraction pattern of the SnS phase is shown in Figure 3-2, whereas the crystallographic information files generated for the single crystal analysis are contained in the Appendix, Table A.1. The powder-diffraction measurements were performed on a Bruker D8-Advance machine



(a) SnS crystals (on the left of the ampoule)



(b) Sn_2S_3 crystals (in the centre of the ampoule)



(c) SnS_2 crystals (on the left of the ampoule)

Figure 3-1: The appearance of single crystal batches obtained from chemical vapour transport, as labelled. The ampoules were identical in size for each case.

and the single-crystal XRD was performed on an X-calibur, Atlas, Gemini-ultra X-ray diffractometer, both for a Cu K α radiation source.

The predicted patterns for the different structures in this work are also shown in Figure 3-2, generated using CrystalDiffract software version 6, which deduces intensities using published atomic scattering factors. It can be seen that the similarities in diffraction patterns would lead to difficulties in distinguishing any SnS_2 present in a SnS sample as the dominant SnS_2 (001) peak overlaps the (111) reflection of the desired SnS. Similarly, Sn_2S_3 exhibits its largest peak at just over 30° for (211), indicating that observing small

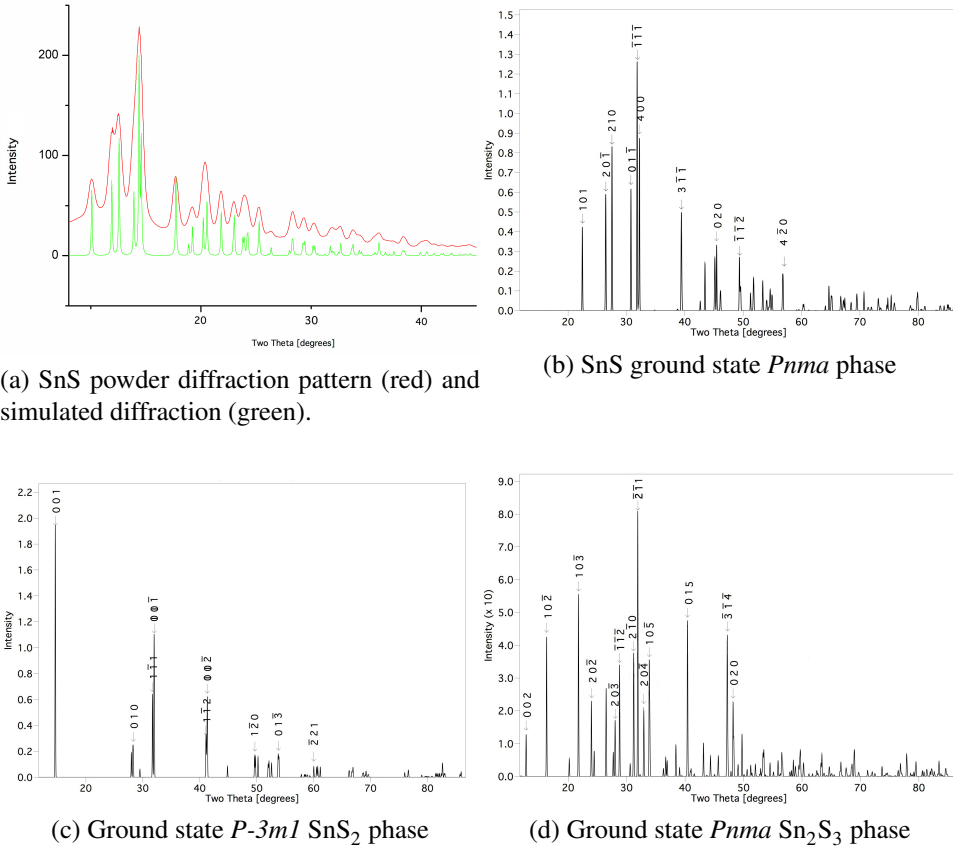


Figure 3-2: Obtained and predicted powder XRD patterns for SnS alongside predicted powder XRD patterns for a Cu K α radiation source.

amounts of tin sulfide phase impurities in a sample predominantly composed of tin monosulfide would be difficult using XRD alone. This is, perhaps, how commercially available ‘SnS’ powder is reported to contain up to 55 % Sn₂S₃ by weight.⁸⁴

In order to assess the stoichiometries and morphology, a high-performance JEOL JSM 6610-LV scanning electron microscope (SEM) fitted with an Oxford Instruments X-Max 800 mm energy-dispersive spectrometer (EDS) was used for multiple point-scans of the single crystals. The crystals were unpolished and unsputtered but the results agree well with the structural assignments of the XRD analysis (Table 3.2).

With the combined XRD and EDS analysis the phase assignment of the three materials is clear, with dark gray SnS, black needles of Sn_2S_3 , and yellow flakes of SnS_2 . However, this assignment is in contradiction to previous studies. Nitsche *et al.* reported black needle-like crystals of SnS, whereas following the same procedure in this study yielded Sn_2S_3 .⁹⁷ Price *et al.* described yellow plates of Sn_2S_3 and black needles of SnS_2 , the opposite of what is observed here.¹³² Many more authors report brown coloured tin sulfide films,⁹² with tunable properties based on Sn:S ratios;^{133,134} a description which corresponds to none of the pure phases and could indicate a mechanical mixture of compounds.¹³⁵ This is problematic in the case of photovoltaics as grain boundaries and localised impurities can act to trap and recombine generated charges.¹³⁶

Table 3.2: Elemental composition of single crystals obtained as atomic percent using energy dispersive spectroscopy and their macroscopic appearance.

Phase	Sn (%)	S (%)	Appearance
SnS	49.54	50.46	dark grey amorphous solid
SnS_2	31.58	68.42	yellow transparent flakes
Sn_2S_3	39.88	60.12	shiny black needles

3.1.1 Single crystal stability

The stability of the crystallites with respect to temperature and oxygen exposure was assessed via thermo-gravimetric analysis (TGA) using a Perkin Elmer 4000 Thermogravimetric Analyser. The crystals were heated from 21 °C to the maximum operating temperature of 858 °C under a flow of air in alumina crucibles. The recorded mass variance as a function of temperature for each of the tin sulfide phases is shown in Figure 3-3.

SnS exhibits a sharp increase in mass beginning at around 550 °C that would indicate oxygen uptake prior to sulfur loss at around 710 °C. This behaviour is likely to be due to the ability of tin to hold both a 2+ or a 4+ charge, *i.e.* bind extra anions, and explains why

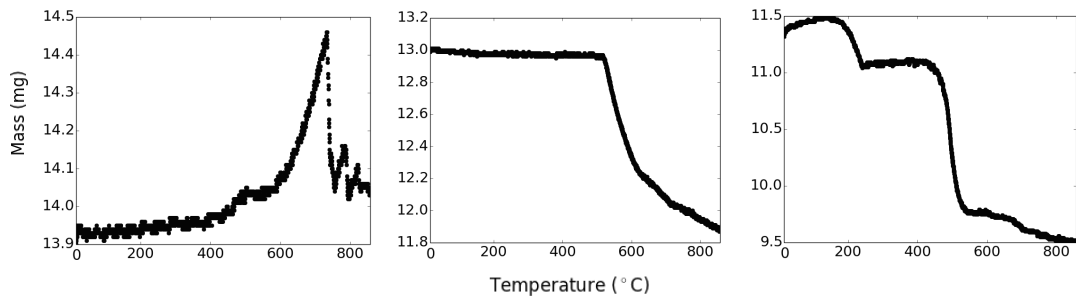


Figure 3-3: Thermo-gravimetric analysis of each of the three phases SnS (left), Sn₂S₃ (centre) and SnS₂ (right) showing change in mass as a function of temperature under a flow of air.

no such increase in mass occurs for SnS₂.

The Sn₂S₃ data shows little change until degradation occurs at around 550 degrees, similar to the onset of degradation of SnS, but higher than that of SnS₂, at around 450 °C. Tin sesquisulfide also does not appear to incorporate additional oxygen as does SnS, and therefore would appear to be more stable.

The graph for SnS₂ shows a two stage mass loss, one beginning at 150 and the other at 450 °C. The low temperature mass loss of around 0.5 mg quantitatively is most likely due surface contaminants and is evidence of residual iodine from the chemical transport synthesis method.

In all cases, significant mass loss is assumed to be due to substitution of sulfur for oxygen, rather than evaporation of components, as the large residual mass observed would suggest that the heavy tin component remains. That said, all of the TGA results indicate that the crystals are stable at ambient conditions with respect to oxygen exposure. However, a surface effect was noted to occur over a period of weeks of exposure to atmospheric conditions that was identified as being localised oxidation on the surface of

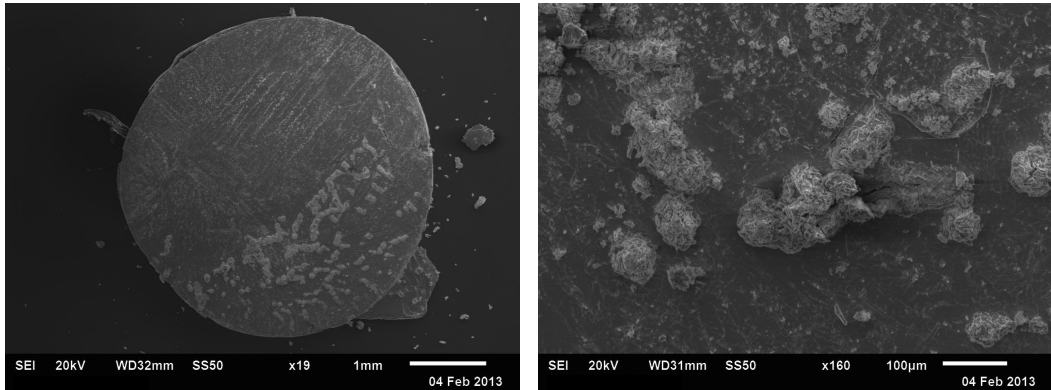


Figure 3-4: Observed localised oxidation of SnS single crystals, using scanning electron microscopy at the scales indicated.

SnS single crystals. These took the form of nodules on the crystal surface as shown by the SEM analysis in Figure 3-4, containing high levels of oxygen as found by EDS. The nucleation procedure and growth mechanism for this process remain unknown due to the extended time frame over which they occur, however, these processes were not observed for the Sn_2S_3 or SnS_2 crystals.

Figure 3-5 again shows that SnS is not stable with respect to atmospheric conditions, with macroscopic amounts of sulfur loss observable around the interior of its container after being kept at temperatures no greater than 28 °C (post synthesis). This is in contrast to the known self-limiting oxidation behaviour of metal surfaces that cease to degrade after a monolayer of oxide has formed.¹³⁷ A possible mechanism for such extensive sulfur loss is the formation of sulfur dioxide upon exposure to air. SO_2 has a vapour pressure of around 3 atmospheres at room temperature,¹³⁸ which would allow for the continued decomposition of SnS in an open environment. It is also possible that exposed defects or defect clusters allow for the onset of localised oxygen degradation.

The volatility of SnS has been shown to be problematic for the CZTS system,¹³⁹ however, the yellow colour of the desorbate shown in Figure 3-5 would indicate a large loss



Figure 3-5: Observed macroscopic amounts of sulfur loss observed for single crystal SnS (left) but not for Sn₂S₃ (centre) or SnS₂ (right). All crystals displayed were synthesised at least three months prior to the image being taken.

of elemental sulfur (proportionally at least), considering that SnS is black. Further work is needed in order to fully assess the degradation pathway observed for SnS crystals, however it is possible to rule the role of iodine given the stability of the alternate phases despite synthesis occurring via the same carrier agent.

The progressive decomposition of SnS (but seemingly not SnS₂ or Sn₂S₃ in the time scales of this project) represents the first potential culprit for poor device performance of this material. While it is true that these observations were made with single crystals in contact with oxygen, it is possible that chemical degradation occurs in the absence of oxygen, or even in the conditions represented by a sealed solid state PV device as it has already been discussed that sulfur can react with molybdenum in devices. Certainly it would seem that sulfur is mobile to some degree, even at ambient conditions, given that degradation is not limited to a surface monolayer.

3.1.2 Single crystal purity

The presence of orange crystallites adhered to certain surfaces of the SnS were observed under a visible light microscope, even after repeated washing procedures. This was later identified as being residual SnI_4 from the CVT synthesis. Grazing incidence X-ray analysis performed on a Rigaku SmartLab Multipurpose Diffractometer indicated that the presence of any crystalline impurities was unique to the surface of the crystals as surface treatment led to a reduction of secondary peaks, as shown in Figure 3-6; which is in good agreement with the work of others,¹⁴⁰ and the predicted patterns in Figure 3-2. Unfortunately, further analysis proved the presence of tin iodide to be more persistent.

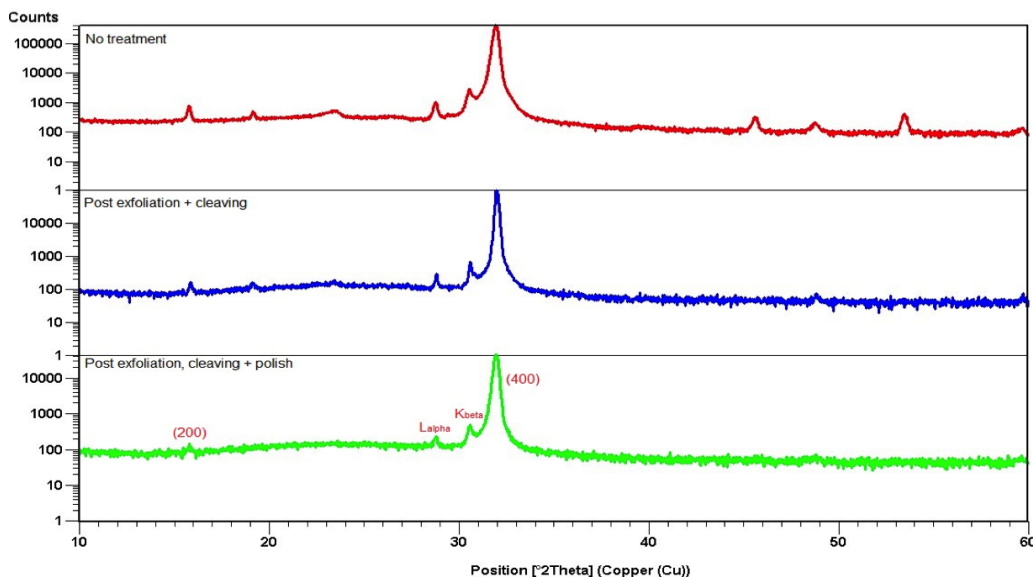


Figure 3-6: Grazing incidence XRD on the surface of single crystal SnS before and after exfoliation and cleaning processes. It can be seen that secondary peaks above 40° and below 20° disappear and the sharpness of the major SnS (400) peak increases for treated compared to untreated samples.

It was found later in the study that the single crystals synthesised using the method described were not of sufficient purity to derive accurate data for transport properties.

Subsequent analysis of single crystal SnS samples using glow discharge mass spectroscopy (GDMS), a service provided by the ‘Evans Analytical Group’, revealed that the presence of impurities in these samples was prohibitively high. The full data for this analysis can be found in the Appendix, Table A.2, with a summary of highest concentration impurities presented in Table 3.3. Here, it is possible to see that not only is there a persistence of iodine in the sample, that can be ascribed to the chosen synthesis method, but also a large concentration of heavy metal impurities that are most likely associated with the tin source.

Table 3.3: Glow discharge mass spectroscopy analysis of single crystal SnS, with impurity elements arranged in descending order of concentration.

Element	Concentration (ppm wt)	Atom mass (g/mol)	Atom number (ppm)	Atoms per volume (cm ⁻³)
I	620.0	126.90	368.32	1.53×10^{19}
Pb	280.0	207.20	101.88	4.24×10^{18}
Sb	100.0	121.76	61.92	2.58×10^{18}
Al	5.3	26.98	14.81	6.16×10^{17}
Cl	2.4	35.45	5.10	2.12×10^{17}

As such, a final batch of SnS was synthesised using the route described in Section 2.1.1 but this time using Alfa Aesar, Puratronic, tin shot, 99.9999 % (metals basis) as the tin source. These higher purity crystals were used only for the Hall measurements discussed in Chapter 5 of this thesis, whereas all alternate analysis implicitly considers crystals that contain said impurities.

3.2 Density functional theory analysis

The unique crystal structures pertaining to the tin-sulfur-iodine-oxygen phase space were identified from the inorganic crystal structure database (ICSD). DFT as implemented in the Fritz Haber Institut *ab initio* molecular simulations (FHI AIMS) package,¹⁴¹ and the

Vienna *ab initio* Simulation Package (VASP),¹⁴² were used to calculate the equilibrium geometry and total energy for each structure. Each calculation was checked for convergence with respect to electronic plane wave density and basis set to within 0.01 eV per formula unit.

All calculations were performed in closed shell configuration (restricted spin), with geometry relaxations undertaken using the Broyden - Fletcher - Goldfarb -Shanno (BFGS) algorithm within FHI AIMS,¹⁴³ and the Davidson algorithm within VASP.¹⁴⁴ A force convergence criterion tolerance in all cases of 0.01 eV per Å was employed.

3.2.1 Phase space analysis of tin sulfide

It is important to consider the entire phase space of tin and sulfur in order to be aware of any possible phase impurities present in SnS, both in single crystals and thin-films.

Sn(II) has the electron configuration [Kr] 4d¹⁰ 5s² 5p⁶ and forms stoichiometric SnS that preferentially crystallises in the orthorhombic herzenbergite structure, with the space group *Pnma*. In this structure, the Sn²⁺ ion coordinates to three S²⁻ ions, with the Sn 5s² lone pair occupying the last position of a tetrahedral geometry. Other phases of SnS that are of interest are the rocksalt (RS) structure grown under epitaxial strain,¹⁴⁵ the high temperature orthorhombic structure,¹³¹ and the zincblende (ZB) structure first reported in 1962 from SnS evaporation onto rocksalt, with more reports occurring only recently.^{146,147} The spacegroup labels for the SnS phases correspond as follows: *Pnma*; the orthorhombic ground state phase, *Fm-3m*; the rocksalt phase, *Cmcm*; the orthorhombic, high temperature phase and the *F-43m* zincblende phase.

The different SnS lattice structures are shown in Figure 3-7 along with the ground state structures of SnS₂ and Sn₂S₃. The low energy phase of SnS₂ (Sn⁴⁺) is a trigonal structure composed of SnS₂ trilayers where the Sn(IV) ion is coordinated to six S ions in an

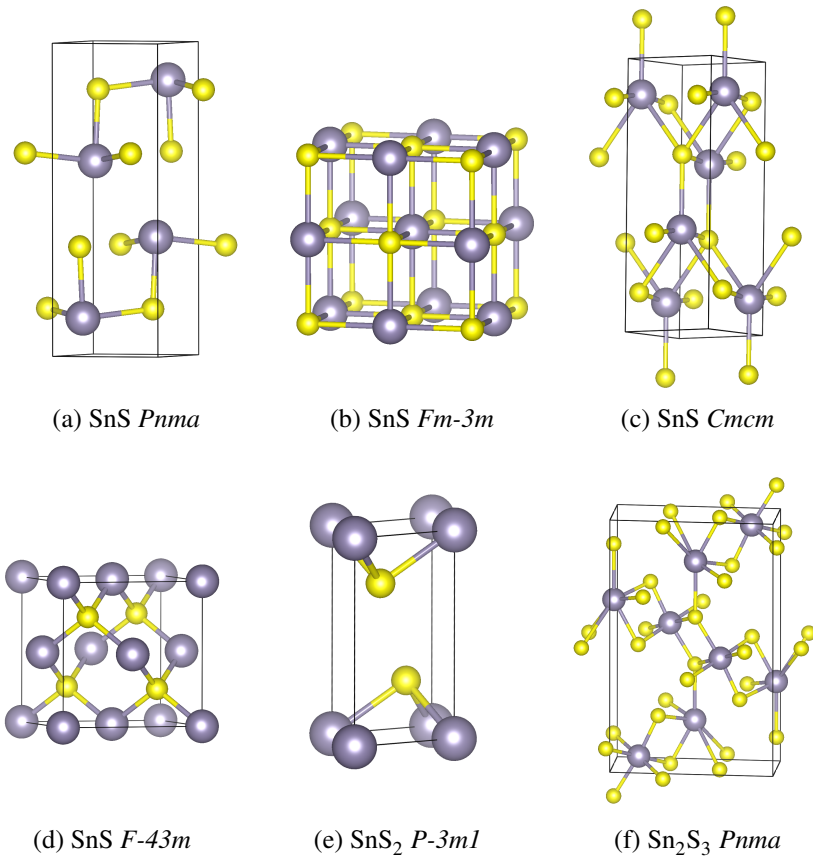


Figure 3-7: the crystal structures of the tin (grey) sulfides (yellow) and the ground state structures of SnS_2 and Sn_2S_3 .

octahedral environment, which is similar, for example, to that found in the 2 dimensional semiconductor MoS_2 .¹⁴⁸ Alternate stacking of the trilayers results in a series of structural polytypes, as typified by the isostructural CdI_2 system.

The crystal structure of tin sesquisulfide (Sn_2S_3) is also orthorhombic and shares the same space group as the ground state phase of SnS . The structure is composed of Sn_2S_3 chains, with the Sn(IV) ions adopting chain-centre positions in octahedral coordination to sulfur, and the Sn(II) ions adopting chain-end positions in the favoured trigonal-pyramidal arrangement. Hence, the coordination preferences of both Sn oxidation states can be si-

multaneously satisfied.

For the enthalpies discussed in this section, the atomic coordinates were fully allowed to relax where ever possible, but in high temperature or highly strained configurations the energy minimisation algorithm would cause the structure to deviate significantly from the experimental geometry. In these cases, the unit cell volume was altered systematically while the internal symmetry was fixed; extrapolation to the lowest energy allowed for the ground state lattice vectors to be identified.

Table 3.4 contains the lattice parameters for the different tin sulfide, oxide and oxysulfide phases discussed in this section. For both VASP and FHI AIMS simulation packages the ground state structure lattice parameters are in excellent agreement with experiment, where the error is typically less than 2%. The *Cmcm* phase could not be stabilised as it is a high temperature conformation that undergoes a second order phase transition to the ground state *Pnma* structure, observed experimentally at around 878 K.¹⁴⁹ A large discrepancy is observed between the calculated and measured lattice parameters for the zincblende *F-43m* structure, which will be discussed later in this section.

3.2.2 Enthalpies of formation & relative stabilities

Enthalpies of formation are key to understanding the relative stabilities of a multi-phase system as they indicate which conformation the system would preferentially adopt. The following results, obtained from DFT calculations, represent values at 0 K (excluding zero point contributions), and do not account for any prohibitive kinetic barriers involved in structural change according to their respective reactions.

The enthalpies of formation for tin monosulfide, shown in Table 3.5 agree well with experiment whereas the formation enthalpies for SnS_2 and Sn_2S_3 somewhat disagree. This result likely reflects more on the difficulty of obtaining phase pure materials experimen-

Table 3.4: Reported structural parameters from experiment and obtained with both FHI AIMS and VASP implementations of the PBEsol level density functional theory for the compounds investigated in this study.

Phase	Spacegroup	Experimental parameters			Ref.	FHI AIMS parameters (% error)		
		<i>a</i>	<i>b</i>	<i>c</i>		<i>a</i>	<i>b</i>	<i>c</i>
I	<i>Cmca</i>	7.12	4.66	9.80	150	7.27 (2.18)	4.68 (0.50)	9.42 (3.85)
S	<i>Fddd</i>	10.48	12.92	24.55	151	10.54 (0.54)	12.57 (2.70)	25.23 (2.78)
Sn	<i>Fd-3m</i>	6.47	6.47	6.47	152	6.54 (1.11)	6.54 (1.11)	6.54 (1.11)
SnS	<i>Pnma</i>	11.32	4.05	4.24	131	11.11 (1.86)	3.99 (1.48)	4.24 (0.00)
SnS	<i>Fm-3m</i>	5.80	5.80	5.80	153	5.75 (0.86)	5.75 (0.86)	5.75 (0.86)
SnS	<i>F-43m</i>	5.85	5.85	5.85	146	6.43 (9.91)	6.43 (9.91)	6.43 (9.91)
SnS ₂	<i>P-3m1</i>	3.64	3.64	5.89	154	3.66 (0.55)	3.67 (0.82)	6.06 (2.89)
Sn ₂ S ₃	<i>Pnma</i>	8.87	3.75	14.02	95	8.80 (0.79)	3.77 (0.53)	13.83 (1.36)
SnO	<i>P4/h m m</i>	3.80	3.80	4.82	155	3.81 (0.26)	3.81 (0.26)	4.76 (1.24)
SnO ₂	<i>P42/m n m</i>	4.74	4.74	3.19	156	4.77 (0.63)	4.77 (0.63)	3.22 (0.94)
SnSO ₄	<i>P42/m n m</i>	8.80	5.32	7.12	157	8.66 (1.60)	5.42 (1.97)	7.08 (0.62)
SnI ₂	<i>C 1 2/m I</i>	14.17	4.54	10.87	158	14.10 (0.50)	4.38 (3.41)	10.75 (1.08)
SnI ₄	<i>P a -3</i>	12.23	12.23	12.23	159	12.08 (1.24)	12.06 (1.35)	12.09 (1.16)
Sn ₂ Si ₂	<i>Pnma</i>	17.45	25.33	4.39	160	17.29 (0.93)	25.04 (1.14)	4.35 (0.93)
Phase	Spacegroup	Experimental parameters			Ref.	VASP parameters (% error)		
I	<i>Cmca</i>	7.12	4.66	9.80	150	7.50 (5.34)	4.40 (5.58)	9.63 (1.73)
S	<i>Fddd</i>	10.48	12.92	24.55	151	10.60 (1.16)	12.95 (0.27)	24.31 (0.98)
Sn	<i>Fd-3m</i>	6.47	6.47	6.47	152	6.54 (1.08)	6.54 (1.08)	6.54 (1.08)
SnS	<i>Pnma</i>	11.32	4.05	4.24	131	11.21 (0.97)	4.02 (0.74)	4.14 (2.36)
SnS	<i>Fm-3m</i>	5.80	5.80	5.80	153	5.74 (1.03)	5.74 (1.03)	5.74 (1.03)
SnS	<i>F-43m</i>	5.85	5.85	5.85	146	6.43 (9.91)	6.43 (9.91)	6.43 (9.91)
SnS ₂	<i>P-3m1</i>	3.64	3.64	5.89	154	3.65 (0.27)	3.65 (0.27)	5.97 (1.36)
Sn ₂ S ₃	<i>Pnma</i>	8.87	3.75	14.02	95	8.82 (0.56)	3.76 (0.27)	13.82 (1.43)
SnO	<i>P4/h m m</i>	3.80	3.80	4.82	155	3.77 (0.79)	3.77 (0.79)	4.62 (4.15)
SnO ₂	<i>P42/m n m</i>	4.74	4.74	3.19	156	4.72 (0.42)	3.12 (2.19)	
SnSO ₄	<i>P42/m n m</i>	8.80	5.32	7.12	157	8.46 (3.86)	5.26 (1.13)	6.89 (3.23)
SnI ₂	<i>C 1 2/m I</i>	14.17	4.54	10.87	158	14.19 (0.14)	4.40 (3.08)	10.75 (1.10)
SnI ₄	<i>P a -3</i>	12.23	12.23	12.23	159	12.17 (0.49)	12.17 (0.49)	12.17 (0.49)
Sn ₂ Si ₂	<i>Pnma</i>	17.45	25.33	4.39	160	17.34 (0.63)	25.08 (0.99)	4.35 (0.91)

Table 3.5: Enthalpies of formation obtained at the PBEsol level of DFT, compared to experimental data where available.

Phase	Spacegroup	ΔH_f^{DFT} (eV)	(kJ mol ⁻¹)	ΔH_f^{exp} (kJ mol ⁻¹)
SnS	<i>Pnma</i>	-1.03	-99.35	-100 to -108 ^{99,161}
SnS	<i>Fm-3m</i>	-0.95	-91.66	
SnS	<i>F-43m</i>	-0.29	-27.80	
SnS ₂	<i>P-3m1</i>	-1.36	-130.99	-148 to -182 ^{161–163}
Sn ₂ S ₃	<i>Pnma</i>	-2.39	-230.35	-249 to -297 ^{161–163}

tally than on the accuracy of the level of theory employed in this work, which is supported by the large variation in the measured enthalpies of formation. As already stated it has proven difficult to confirm the isolation of a pure single phase by diffraction techniques alone (see, for example, Figure 1-11).

The calculated enthalpy of formation for individual phases plotted against elemental composition affords a convenient method of comparing phase stabilities for any binary state. A convex hull is a plot of this kind, with the lowest energy states connected to form the base of a ‘hull’ and any higher energy states appearing above this line. The convex hull for tin sulfide is shown in Figure 3-8.

A few anomalous results can be highlighted at this stage. Firstly, it is possible to see that the Sn₂S₃ phase does not lie on the convex hull *i.e* the line connecting the SnS₂ and SnS phases would pass below the obtained enthalpy of Sn₂S₃, by around 6 meV quantitatively. This would usually indicate that Sn₂S₃ would rather dissociate into SnS and SnS₂, however, the prevalence and stability of the Sn₂S₃ crystals discussed in the previous sections have led to this modified representation of the convex hull for its inclusion. It is also important to note that a higher level of density functional theory that includes non-local van der Waals interactions explicitly, may be necessary to accurately describe tin sesquisulfide, and, as such, the proximity to the convex hull may be within associated errors.¹⁶⁴

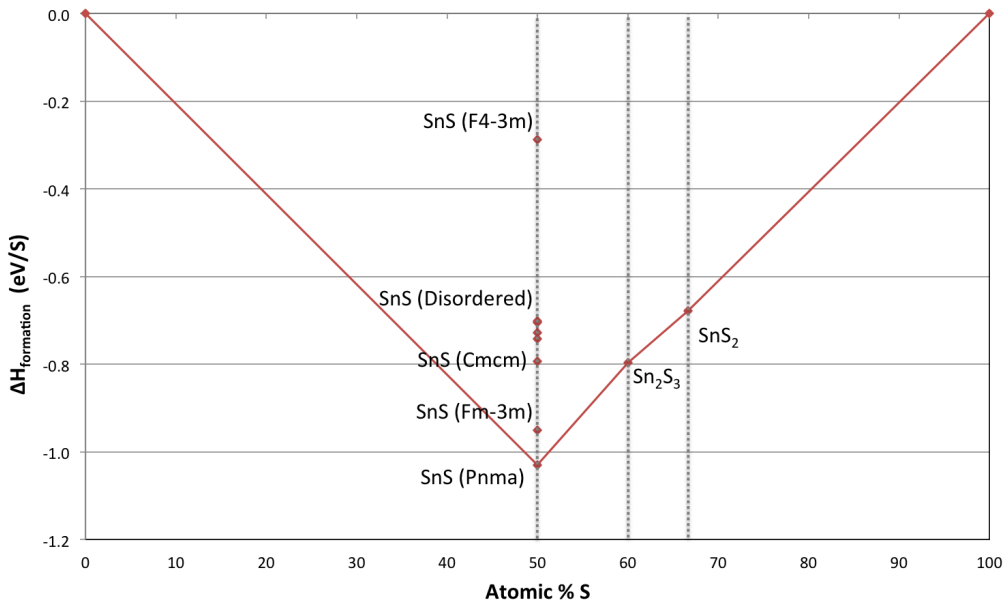


Figure 3-8: Plot showing enthalpy of formation from PBEsol DFT against atomic percent of sulfur present in each phase. The convex hull indicates the ground state energy as a function of sulfur composition.

Secondly, the enthalpy of formation for the zincblende phase of SnS is aberrantly small. Figure 3-8 shows that ZB (*F-43m*) tin monosulfide should not be thermodynamically accessible given that it resides so high on the convex hull. Considering that *Cmcm* SnS does not form below 878 K,¹⁴⁹ and is 0.236 eV above the ground state, it is possible to predict that ZB SnS would correspond to an accessible phase at around 2760 K. By contrast rocksalt *Fm-3m* SnS, while not the ground state, could still be thermodynamically accessible at reasonable conditions.

The inherent instability of the ZB phase has been verified with alternate DFT functionals (LDA and GGA) and both implementations (*i.e.* FHI AIMS and VASP). The calculated energy-volume curve is shown in Figure 3-9 alongside that of rocksalt *Fm-3m*. The slope of the curves represents the effective pressure of the system, *i.e.* $P = -(\partial E / \partial V)_T$, which

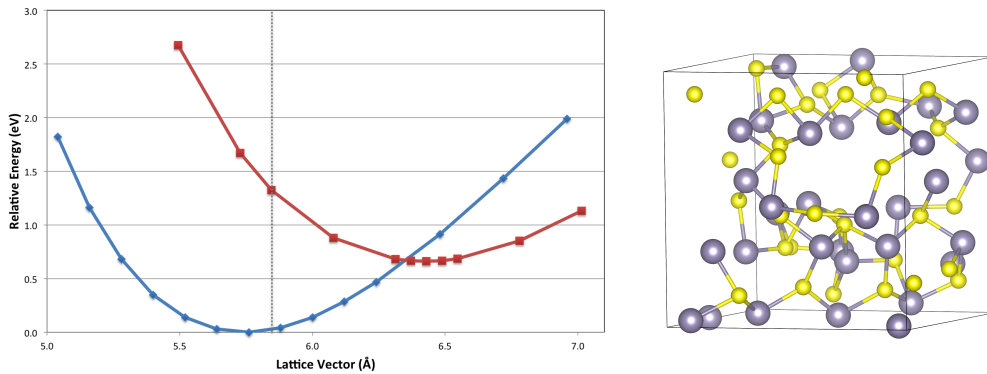


Figure 3-9: The energy-volume curve for zincblende (red) and rocksalt (blue) SnS, with the reported lattice parameter of 5.845 Å highlighted with a vertical line (left) and a structure of amorphous SnS obtained upon relaxation the ZB phase (right).¹⁴⁶

for the observed ZB lattice parameter corresponds to an extremely large pressure of around 930 GPa , and can clearly not be representative of an equilibrium state. On the other hand, it is important to note the similarity between the experimentally observed ZB lattice parameter and the relaxed rocksalt lattice parameter.

In order to confirm the dynamic phase instability of ZB SnS, *ab initio* molecular dynamics (MD) simulations were carried out within the Nosé-Hoover thermostat of the NVT canonical ensemble. This approach combines DFT forces with classical Newtonian mechanics, and a time-step of 1 fs. The temperatures modelled were 300, 500, 700, and 1000 K over 5 ps and quenched directly to 0 K, by the standard local optimisation procedure. All of these calculations lead to a spontaneous distortion from the high symmetry ZB phase to an amorphous geometry, a typical resultant structure from which is shown in Figure 3-9. The enthalpies of formation for these amorphous structures are included in the convex hull for comparison (labelled ‘SnS (disordered)’ in Figure 3-8).

Three plausible explanations exist for this behaviour: (i) the phase found in experiment is not ZB; (ii) the phase is formed in a highly strained environment; (iii) the phase is stabilised by a high concentration of lattice defects. However, the predicted X-ray diffrac-

tion patterns for rocksalt and zincblende SnS, at the same lattice spacing, are shown to be almost identical, see Figure 3-10. These agree well with the experimental XRD on ZB SnS obtained by Greyson *et al.* and with those obtained by Avellaneda *et al.* for nano-particulate and thin-film ZB tin sulfide respectively.^{146,147} One can see that the peak positions and the reflections associated with each are equivalent, due to the common fcc crystal structure, and it would be possible to confuse the two. The preferential orientation of crystals is not accounted for here due to the dependence of the growth process on nucleation,¹⁶⁵ but a powder diffraction pattern of each would show that ZB SnS exhibits a stronger (111) reflection at $2\theta = 26.8^\circ$, whereas rocksalt SnS would have a stronger (002) reflection at $2\theta = 31.0^\circ$. In previous work, the intensity ratios predicted for ZB SnS were not used in ascribing the ZB structure from the diffraction pattern and this could be an important consideration in distinguishing between the two phases.¹⁴⁷

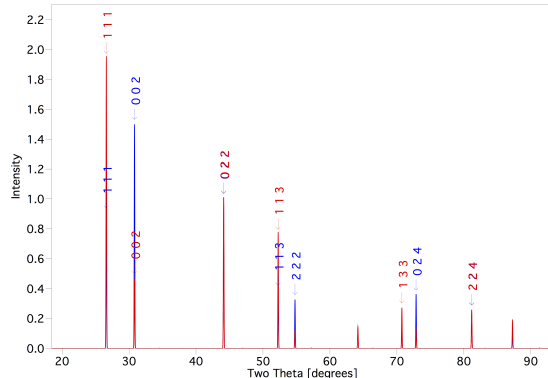


Figure 3-10: The predicted powder XRD patterns for rocksalt (blue) and zincblende (red) SnS.

It would appear from this DFT analysis of the tin-sulfur phase space that good agreement with experiment is obtained, with the exception of zincblende SnS, which is predicted to be thermodynamically and kinetically unstable. These predictions match previous calculations showing that Sn(II) in a tetrahedral environment with sulfur will form an

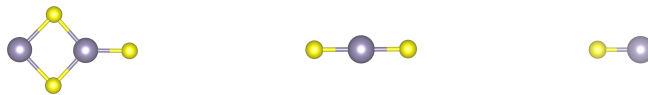


Figure 3-11: The calculated structures of molecular Sn_2S_3 , SnS_2 and SnS , from left to right, respectively.

asymmetric electron density *i.e.* an electron lone pair, due to orbital interactions (Sn 5s-5p hybridisation).¹⁶⁶ Indeed, evidence of lone pair formation can be seen in the apparent cavity formation of the relaxed ZB structure of Figure 3-9, which is also seen for other tin compounds.¹⁶⁷ On the basis of the equivalent nature of reflections in the RS and ZB diffraction patterns, it would appear most likely that the known rocksalt phase of SnS has been mis-assigned as zincblende in recent reports.

3.2.3 Enthalpies of sublimation & disproportionation

Enthalpies of sublimation are important for materials processing methods, such as chemical vapour deposition, and post processing techniques, such as thermal annealing. Herein, they are considered according to the following reaction: $\text{Sn}_x\text{S}_y(\text{s}) \longrightarrow \text{Sn}_x\text{S}_y(\text{g})$ and are displayed in Table 3.6.

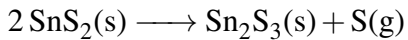
While the structures of molecular SnS and SnS_2 are trivial, the structure assumed for the gaseous form of Sn_2S_3 was taken from an evolutionary algorithm search, which showed it to be the only stable structure for 5 bonded atoms that allows for the two different oxidation states within one formula unit.¹⁶⁸ The structure of SnS_2 and SnS were assumed to be linear, like that of CO_2 and CO respectively, and are all shown in Figure 3-11.

The exceptional agreement observed for the sublimation enthalpy of SnS , alongside that shown for the enthalpy of formation of SnS , reflect the suitability of the chosen simulation methodology in this work.

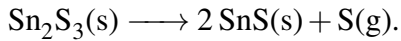
Table 3.6: Enthalpies of sublimation predicted by DFT, compared to experimental values where available.

Phase	Spacegroup	ΔH_{sub}^{DFT} (eV)	ΔH_{sub}^{DFT} (kJ mol ⁻¹)	ΔH_{sub}^{exp} (kJ mol ⁻¹)
SnS	<i>Pnma</i>	2.28	219.96	$220 \pm 2^{163,169}$
SnS ₂	<i>P-3m1</i>	3.01	290.48	
Sn ₂ S ₃	<i>Pnma</i>	3.08	297.14	

While the enthalpy of sublimation can be instructive, it has been observed that the sesqui- and disulfide phases decompose before sublimation occurs, according to the reactions¹⁶³



and



The corresponding enthalpies of disproportionation are 0.16 eV (15.82 kJ mol⁻¹) for the SnS₂ decomposition and 0.33eV (31.65 kJ mol⁻¹) for that of Sn₂S₃. The enthalpy changes as per these reaction pathways are much lower in magnitude than those for direct sublimation, agreeing with the behaviour reported by others in the literature.¹⁶³ However, these results would indicate that the sesqui- and disulfide crystal phases would lose sulfur over time, and decompose to SnS, whereas it is the tin monosulfide that is observed to lose sulfur in this project. An explanation for this is that, while these reaction energies are lower than those of sublimation, they are still many times greater than the thermal energy at room temperature (2.47 kJ mol⁻¹) and this method of DFT does not allow for the quantification of prohibitive energetic barriers for reactions.

3.2.4 Enthalpies of reaction with oxygen

The enthalpies for the direct oxidation of tin sulfide phases are shown in Table 3.7, to highlight possible surface reactions upon exposure of tin monosulfide to oxygen or excess sulfur.

Table 3.7: The enthalpies of oxidation for the reactions listed as predicted by DFT.

Reaction	ΔH_{ox} (eV)	ΔH_{ox} (kJ mol ⁻¹)
$2 \text{SnS} + \text{O}_2 \longrightarrow 2 \text{SnO} + \frac{1}{4} \text{S}_8$	-3.20	-308.58
$\text{SnS} + \text{O}_2 \longrightarrow \text{SnO}_2 + \frac{1}{8} \text{S}_8$	-4.09	-394.86
$\text{SnS}_2 + \text{O}_2 \longrightarrow \text{SnO}_2 + \frac{1}{4} \text{S}_8$	-3.76	-363.22
$2 \text{SnS}_2 + \text{O}_2 \longrightarrow 2 \text{SnO} + \frac{1}{2} \text{S}_8$	-2.54	-245.30
$\text{SnS} + 2 \text{O}_2 \longrightarrow \text{SnSO}_4$	-7.69	-742.26

The enthalpies of disproportionation that involve oxygen are also considered, in order to account for the ambivalent nature of tin ions and are shown in Table 3.8. The addition of sulfur to form Sn⁴⁺ is included for comparison.

Table 3.8: The enthalpies of disproportionation with oxygen, beginning with tin monosulfide, from DFT.

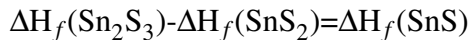
Reaction	ΔH_{ox} (eV)	ΔH_{ox} (kJ mol ⁻¹)
$\text{SnS} + \text{S} \longrightarrow \text{SnS}_2$	-0.33	-31.64
$2 \text{SnS} + \frac{1}{2} \text{O}_2 \longrightarrow \text{SnO} + \text{SnS}_2$	-1.93	-185.93
$3 \text{SnS} + \frac{1}{2} \text{O}_2 \longrightarrow \text{SnO} + \text{Sn}_2\text{S}_3$	-1.93	-185.94
$2 \text{SnS} + \text{O}_2 \longrightarrow \text{SnO}_2 + \text{SnS}_2$	-4.42	-426.50
$3 \text{SnS} + \text{O}_2 \longrightarrow \text{SnO}_2 + \text{Sn}_2\text{S}_3$	-4.42	-426.51

The reaction enthalpies implicitly assume an oxygen partial pressure of 1 atm. While this level of theory is known to over-stabilise the O₂ molecule,¹⁷⁰ the energetic effect is much smaller than the values presented here.

The above results indicate that oxidation of tin sulfide is a favourable, exothermic reaction. It is also possible to see the relative preference of tin to fully oxidise to SnO₂. From

this, one would expect that any tin sulfide sample exposed to air will contain a surface oxide layer at least, corroborated by observations reported in the literature of oxygen within tin sulfides, despite stringent counter-measures put in place.⁹⁵

There are two sets of identical enthalpies shown in Table 3.8, which can be shown not to be an error, by noting that the difference between the reactions equates to the following:



This result implies that no energy is lost or gained in forming the mixed oxidation-state sesquisulfide and is problematic for tin sulfide as it is likely that *both* SnS₂ and Sn₂S₃ form on exposure to oxygen.

Finally, the formation of a stable oxysulfide was found to be -7.69 eV (-742.26 kJ mol⁻¹), which is the largest favourable enthalpy reported thus far. This is significant as it shows that oxygen uptake in SnS is thermodynamically favourable without any loss of sulfur, which agrees with the TGA analysis presented in Section 3.1.1.

3.2.5 Enthalpies of reaction with iodine

The enthalpies of formation of the tin iodides along with several competing iodination reactions are shown in Table 3.9. The enthalpies for reaction between iodine and all of the tin sulfide phases are relatively low, but still thermodynamically stable. Consequently, it is possible to predict that all single crystals produced by the CVT method will contain iodine impurities to a certain degree, despite a small amount of iodine used in the synthesis.

In order to investigate the potential role of the presence of iodine on localised oxidation, the overall ternary phase diagrams for the systems considered in this chapter are shown in Figure 3-12. These diagrams contain all of the stable phases predicted using the PBEsol level of the VASP implementation and are produced using the Computational Phase Diagram Application of the Materials Project.^{171,172} It is important to note that

Table 3.9: The enthalpies of iodination for the tin sulfide phases from DFT analysis.

Reaction	ΔH_I (eV)	ΔH_I (kJ mol ⁻¹)
$\text{Sn} + \text{I}_2 \longrightarrow \text{SnI}_2$	-1.44	-138.79
$\text{Sn} + 2\text{I}_2 \longrightarrow \text{SnI}_4$	-1.49	-144.09
$\text{SnS} + \text{I}_2 \longrightarrow \text{SnI}_2 + \frac{1}{8}\text{S}_8$	-0.41	-39.44
$\text{SnS} + 2\text{I}_2 \longrightarrow \text{SnI}_4 + \frac{1}{8}\text{S}_8$	-0.46	-44.75
$\text{SnS} + \text{I}_2 \longrightarrow \text{Sn}_2\text{SI}_2$	-0.44	-42.64
$\text{SnS}_2 + \text{I}_2 \longrightarrow \text{SnI}_2 + \frac{1}{4}\text{S}_8$	-3.09	-298.28
$\text{SnS}_2 + 2\text{I}_2 \longrightarrow \text{SnI}_4 + \frac{1}{4}\text{S}_8$	-0.14	-13.10
$\text{Sn}_2\text{S}_3 + 2\text{I}_2 \longrightarrow 2\text{SnI}_2 + \frac{3}{8}\text{S}_8$	-0.49	-47.24
$\text{Sn}_2\text{S}_3 + 4\text{I}_2 \longrightarrow 2\text{SnI}_4 + \frac{3}{8}\text{S}_8$	-0.60	-57.84

while these do show some compounds not explicitly considered in the preceding discussions there are no known ternary tin iodo-oxide compounds or quaternary blends of tin, sulfur, oxygen and iodine. As such it is likely that the oxidation seen for SnS in this project is not triggered by the localised presence of iodine from the CVT synthesis method.

3.2.6 Chemical reactions in potential device configurations

Simple thermodynamic arguments have been shown to play a fundamental role in the design, optimisation and performance of solar cell devices, due to issues associated with phase mixing and separation across interfaces.¹⁷³ The instability of SnS with respect to atmospheric and CVT synthesis conditions have already been presented, in this section the stability of tin monosulfide in a hypothetical device configuration will be explored.

Evidence of metal disulfide formation at chalcogenide - metal interfaces has been presented in the literature,¹⁷⁴ even for SnS itself.¹⁷⁵ It has been established that these interface impurities, even of the order of a few tens of nm, can affect the formation of an Ohmic contact.¹⁷⁶

In Chapter 1 the sustainability of SnS as an earth abundant material was established. It would thus be self-defeating to seek device contacts for SnS that are themselves rare or

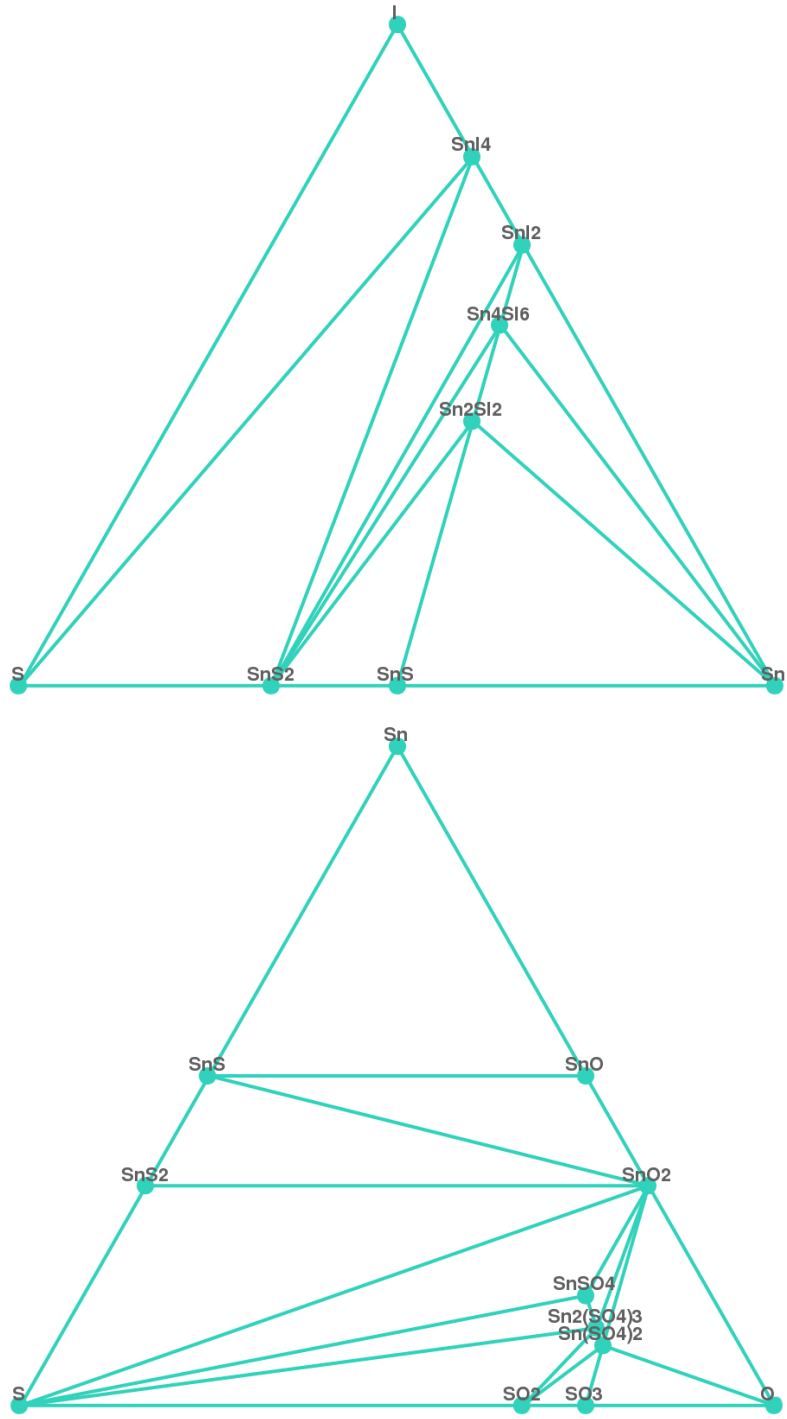


Figure 3-12: The phase diagram for Sn - S - I (top) and the phase diagram for Sn - S - O (bottom) configuration space from PBEsol level of the VASP implementation.

expensive. Four metals are explicitly investigated as device contacts for tin monosulfide in this thesis, which are molybdenum, tin, titanium and tungsten. As such, the possibility of the formation of relevant disulfides is explored in this section by calculating the enthalpies of degradation reactions shown in Table 3.10.

Table 3.10: Thermodynamic equations for the metal sulfide formation and their calculated enthalpies.

Reaction	Enthalpy of reaction ΔH_r (eV)	(kJ mol ⁻¹)
$\text{Mo(s)} + \frac{1}{4} \text{S}_8(\text{g}) \longrightarrow \text{MoS}_2(\text{s})$	-3.02	-290.98
$\text{Sn(s)} + \frac{1}{4} \text{S}_8(\text{g}) \longrightarrow \text{SnS}_2(\text{s})$	-1.36	-130.99
$\text{Ti(s)} + \frac{1}{4} \text{S}_8(\text{g}) \longrightarrow \text{TiS}_2(\text{s})$	-4.15	-400.78
$\text{W(s)} + \frac{1}{4} \text{S}_8(\text{g}) \longrightarrow \text{WS}_2(\text{s})$	-2.82	-271.69
$\text{Mo(s)} + 2 \text{SnS(s)} \longrightarrow \text{MoS}_2(\text{s}) + 2 \text{Sn(s)}$	-0.96	-92.28
$\text{Sn(s)} + 2 \text{SnS(s)} \longrightarrow \text{SnS}_2(\text{s}) + 2 \text{Sn(s)}$	0.70	67.71
$\text{Ti(s)} + 2 \text{SnS(s)} \longrightarrow \text{TiS}_2(\text{s}) + 2 \text{Sn(s)}$	-2.09	-202.09
$\text{W(s)} + 2 \text{SnS(s)} \longrightarrow \text{WS}_2(\text{s}) + 2 \text{Sn(s)}$	-0.92	-88.37

Several interesting points can be discerned from these results. The first is the formation enthalpy for the metal sulfides is the least negative for tin sulfide than any of the disulfides assessed. This is reflected in the explicit contact/SnS reaction scheme, showing that degradation is only thermodynamically unfavourable for tin. The important conclusion therefore is that, excluding kinetics, all tin sulfide devices fabricated to date with molybdenum will develop an MoS_2 intermediate layer (including the champion device).⁸² Whether this is beneficial or harmful in this case remains to be seen. For example, it is known that MoSe_2 has a beneficial effect in CIGS cell performance, as such, the formation of an interlayer is itself no reason to discount a possible Ohmic contact formation.¹⁷⁶ An attempt to clarify the likely effects of these predictions are reported in the later chapters of this thesis.

3.3 Results comparison & discussion

This chapter has shown both the degree of overlap between the remits of theory and experiment and the predictive power of DFT.

The thermodynamic calculations show exceptional agreement with observed structural parameters for the tin sulfide family of compounds with the exception of zincblende SnS. The ZB tin monosulfide appears unusually high in energy and spontaneously distorts when allowed to relax even at room temperature. The similarity between the RS and ZB XRD patterns lead to the conclusion that ZB SnS is in fact mis-assigned RS SnS.

Despite the reduction of complexity represented by eliminating the possibility of the presence of a phase of SnS, it should still be noted that rocksalt SnS could be present in films or at device interfaces, given that it is known to form under epitaxial strain.¹³¹ This is significant as it is predicted to have topologically insulating properties that would harm the rectifying behaviour required for solar cell operation.¹⁷⁷ Besides this, the predicted diffraction patterns highlight possible difficulties in characterising sample purities and structural uniformity in tin sulfide samples. To fully ensure the phase purity of thin films 2-dimensional mapping techniques could highlight regions of off-stoichiometry, while depth profiling techniques could investigate the presence of interlayers.

The calculations present in this chapter also aid in the understanding of the behaviour for the ground state single crystals. The thermodynamic calculations support the observations of degradation of SnS in the presence of oxygen and the persistence of iodine from the CVT method. Unfortunately the mechanism for progressive sulfur loss from the tin monosulfide phase at room temperature has yet to be identified.

The DFT derived enthalpies of iodination allow for a greater scope of optimisation of the CVT method. The slightly stronger preference for SnS_2 to form a tin iodide phase,

shown in Table 3.9, indicates that these crystals ought to be cooled quickly from above the boiling temperature of tin iodide in order to keep these phases as separate as possible. Interestingly, the fact that *all* of the iodination enthalpies are favourable means that the final tin sulfide formation step of the CVT synthesis is endothermic. As a result, it is possible to predict that reversing the temperature gradient, after the formation of the tin iodide, should yield a more rapid synthesis for all phases.

The DFT results are able to go beyond the isolated crystal system and predict that, even in typical solid state device configurations, chemical degradation is likely to occur. Interestingly the only scenario in which degradation is predicted to not occur is with SnS in contact with tin metal, a contact that has yet to be trialled in the literature.

An important conclusion from these results is that chemical vapour transport is a potentially inferior single crystal synthesis technique, due to the presence of carrier agent found in the crystals, compared to, for example, the Bridgman-Stockbarger method that does not require a carrier agent. That said Bridgman-Stockbarger does require a crystal seed to trigger the onset of crystal growth. A potential solution to this problem is to use high purity CVT synthesis to yield a crystal that was subsequently cleaned and polished, to act as a seed for further crystal growth using the Bridgman-Stockbarger method. This tandem technique could significantly reduce the potential for impurity incorporation in to the phase pure crystals that were observed in the GDMS analysis for the CVT crystals in this project.

Chapter 4

Electronic & optical properties

In this chapter the opto-electronic properties of several relevant semiconductors are considered, which, ultimately, define the photovoltaic performance of a given material. As well as analysis of SnS itself, studies on the impurity phases and potential device contacts are presented. Possible origins of poor PV performance of SnS are identified with both experimental and computational electronic structure analysis.

4.1 Single crystal analysis

This section details the results obtained from the analysis of the single crystals synthesised using the methods discussed in Chapter 2. Specifically, the band gaps, work functions and optical absorption data for the tin sulfide phases are presented.

4.1.1 Single crystal band gaps from reflectivity

The difficulty in ensuring that SnS samples are phase pure has been shown already in this thesis, along with the calculated instability of SnS with respect to disproportionation

Table 4.1: Reported optical band gaps of the tin sulfides from thin-film and single crystal samples. The type of band gap used in the fitting process is shown in parenthesis.

Phase	Reported optical band gap (eV)
SnS	0.9 - 1.1 (indirect); ¹⁷⁹ 1.08 (indirect); ⁶⁴ 1.27 (allowed indirect); ¹³⁴ 1.32 (direct); ^{180,181} 1.43 (direct); ⁹² 1.70 (direct); ^{83,182} 1.79 (direct). ¹⁸³
SnS ₂	1.82 (forbidden indirect); ¹⁸⁴ 2.07; ¹⁸⁵ 2.2 (forbidden indirect); ¹⁸⁶ 2.41 (not defined). ¹⁸⁷
Sn ₂ S ₃	0.95eV (forbidden direct); ¹⁸⁸ 1.05 (forbidden direct); ¹⁸⁶ 1.16 (forbidden direct); ¹⁸⁹ 1.6-1.9 ¹⁹⁰ 2 (direct); ¹⁹¹ 2.2 (indirect). ¹⁹²

both in atmospheric conditions and a device configuration. While it is possible that precise control of sulfur content during synthesis could avoid this occurrence for SnS, such control was not sufficient in preventing off-stoichiometric phases of FeS₂ forming for example; another earth abundant material that has so far failed to deliver as a PV absorber layer, as discussed in Section 1.4.⁴⁷ In this chapter, the degree to which the presence of impurities would be problematic for photovoltaic applications has been investigated.

The physical appearance of the single crystals suggests band gaps close to the IR region of the electromagnetic spectrum for SnS and Sn₂S₃ (*i.e.* black) and a larger gap closer to the UV region for SnS₂ (*i.e.* yellow). As such, it could be that the reported brown colouring of SnS thin films and powders in the literature is in fact a mixture of the dark SnS/Sn₂S₃ and the lighter SnS₂.¹⁷⁸

Previous experimental measurements of the band gaps for each of the tin sulfide materials are collected in Table 4.1, showing that values are wide-ranging: 1.08 - 1.79 eV for SnS, 1.82 - 2.41 eV for SnS₂ and 0.95 - 2.20 eV for Sn₂S₃. In addition to the methods of synthesis for the materials, variation can also be attributed to the fitting process, where the optical absorption spectrum is subject to a linear fit and extrapolation.

Each of the three single crystals from this study were analysed by UV/vis spectroscopy with a Shimadzu UV-2600 UV/Vis/NIR spectrophotometer between 400 and 1400 nm wavelength light. The strongest onset of absorption or sudden decrease in reflection can

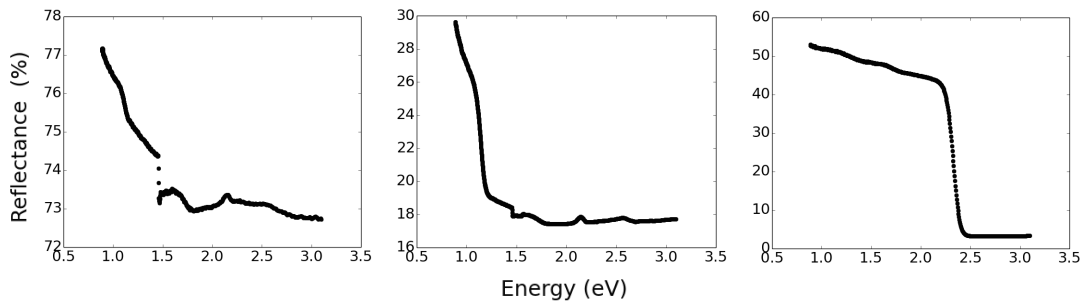


Figure 4-1: Ultraviolet-visible reflectance spectroscopic analysis of SnS (left), Sn_2S_3 (centre) and SnS_2 (right), showing change in reflectance as a function of incident photon energy.

be extrapolated to find the optical band gap of the material, given that above the energy of the band gap photons can promote electrons across said gap. SnS has an extrapolated band gap value of 1.47 eV, Sn_2S_3 has a value of 1.20 eV and SnS_2 has a value of 2.42 eV, as shown in Figure 4-1 a, b and c respectively. Dispersions in reflectance above the band gap, observed particularly for SnS and Sn_2S_3 in these experiments are attributed to defects and impurities in the solid.¹⁹³

The band gap values agree with the appearance of the crystals and the literature data presented in Table 4.1. Given that a high carrier concentration leads to high reflectance,⁹⁹ the data qualitatively indicates that SnS_2 contains fewer impurities than the other phases; an intriguing result given that each of the three crystals were synthesised using the same method and iodine carrier. Indeed, it is possible that a high susceptibility to intrinsic defect formation for SnS explains the high reflectance. SnS also has a larger refractive index than SnS_2 , which could contribute to the higher sub-band gap reflectivity observed for SnS in these experiments.¹⁹³ It is worth noting that tin dioxide has a lower refractive index than tin sulfide and, as such, surface oxidation is not likely to be the cause of this high degree of reflectance.¹⁹⁴

4.1.2 SnS band gap from optical absorption relative to temperature

In this section, the optical properties of tin monosulfide are reported as a function of temperature. These results allow for the assignment of SnS as either a fundamentally direct or an indirect band gap material, as well as allowing for a more direct comparison with the results of DFT, which implicitly correspond to a material at 0 K.

Fourier-transform infra-red (FTIR) spectroscopy was performed using a Bruker Vertex 70v Fourier transform IR spectrometer using a NIR source, a CaF₂ beam-splitter with both an InGaAs and HgCdTe diode detector and a 1.5 mm instrumental aperture cooled with liquid helium on a single crystal of SnS.

The optical absorption coefficient, which is an indication of how strongly a material absorbs light as a function of photon energy, for temperatures between 4 and 350 K, was determined using transmittance, T , reflectance, R and crystal thickness d data, via the relationship,¹⁹⁵

$$\alpha = \frac{1}{d} \ln \left[\frac{(1-R)^2 + \sqrt{(1-R)^4 + (2RT)^2}}{2T} \right] \quad (4.1)$$

The results of this experiment are shown in Figure 4-2, with the corresponding band gaps from linear extrapolation of the absorption profiles shown as a function of temperature in Figure 4-3.

The temperature dependent absorption shows a trend of increasing band gap with increasing temperature before the onset of indirect absorption reverses the trend, which agrees well with the work of others.¹⁹⁶ The highlighted change in the direction of the trend for absorption as a function of increasing temperature is indicative of a direct band gap of SnS at around 1.21 eV at 0 K. As a greater number of crystal phonons become active in the material, new optical absorption transitions across the band gap become accessible

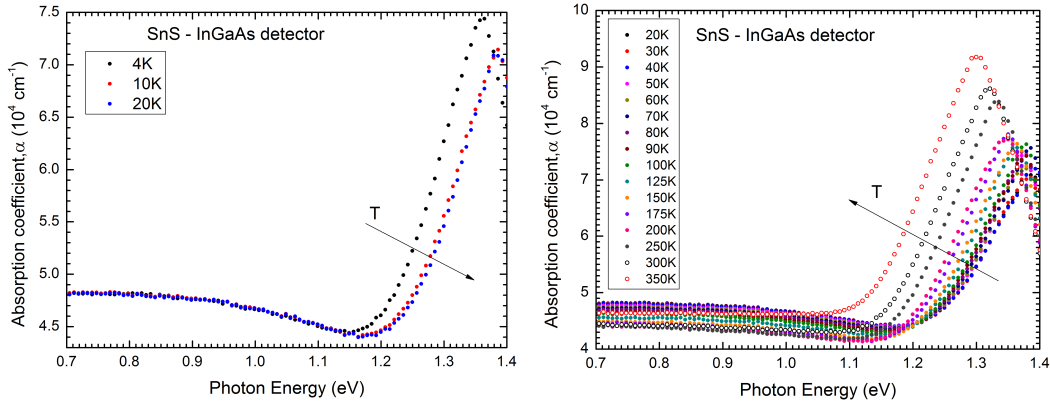


Figure 4-2: Absorption coefficient as a function of photon energy profiles varying with temperature for SnS single crystals with the InGaAs detector.

and the band gap begins to decrease after around 50 K. At around 300 K, an indirect fundamental band gap of 1.14 eV is observed for both detectors, which agrees with the room temperature data from the literature shown in Table 4.1.

The absorption coefficient data agrees well with the optical properties reported for SnS thin films,¹⁹⁵ and the high peak of around $9 \times 10^4 \text{ cm}^{-1}$ also agrees with the work of others.¹⁹⁷ It should be noted that the optical properties of materials with indirect band gaps are known to depend on temperature, despite observations to the contrary for SnS thin films.¹⁹⁸

The linear dependence of band gap on temperature above 100 K here, yields a relationship -0.4 meV K^{-1} between 125 and 350 K, which is in excellent agreement with a variation of $-0.405 \text{ meV K}^{-1}$ reported for 100 to 300 K in the literature.¹²⁸

Despite the peak in band gap observed by both detectors at 1.24 eV for around 50 Kelvin, the 300 K band gap of 1.14 eV is still more optimal than that of silicon, another indirect absorber, for PV applications. Despite these factors, silicon is able to reach over 20 % in modern device architectures as discussed in the Introduction, more than 6 times the current record for SnS.

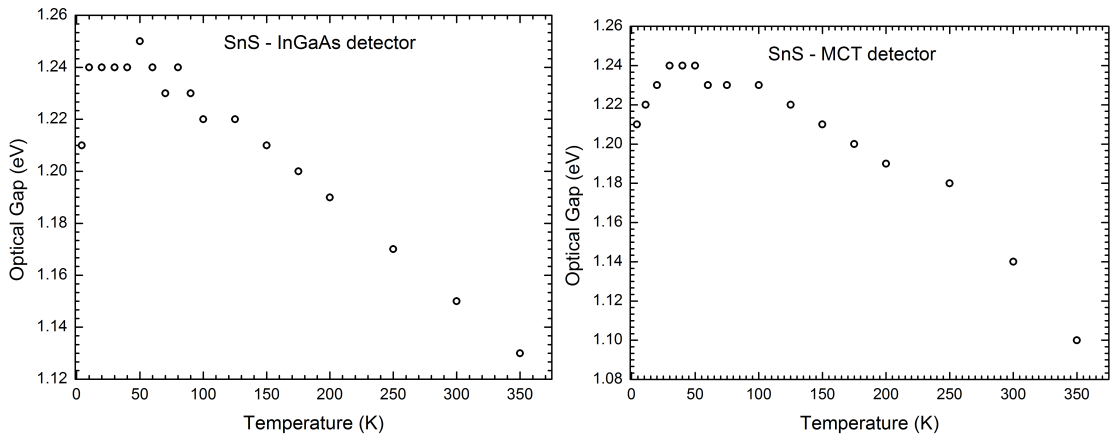


Figure 4-3: Observed SnS band gaps as a function of temperature recorded with an InGaAs detector (left) and HgCdTe detector (right).

The results in this section have shown that SnS exhibits high optical absorption and ideal band gaps across a wide range of temperatures. While these measurements are insightful, they do not allow for the identification of any major efficiency loss mechanisms for SnS PV. As such, the parameter that allows for the relative placement of the energy levels of both SnS and the competing tin sulfide phases is sought: the work function.

4.1.3 Evaluation of work function & band gaps for all phases

X-ray photoelectron spectroscopy (XPS) is a technique that allows for composition analysis of solids and was performed using a Mg-K α anode with 144 W of power, in order to analyse the surfaces of the crystals. Binding energies were obtained with an initial low resolution survey up to 1100 eV and a subsequent high resolution sampling of key regions. The results of this analysis directly affected the procedure for subsequent ultraviolet photoelectron spectroscopy (UPS) and inverse photo-emission spectroscopy (IPES) analysis.

UPS measures kinetic energy of emitted photoelectrons using, in this case, a helium lamp with a survey region between 10 and 22 eV, and allows for the identification of a

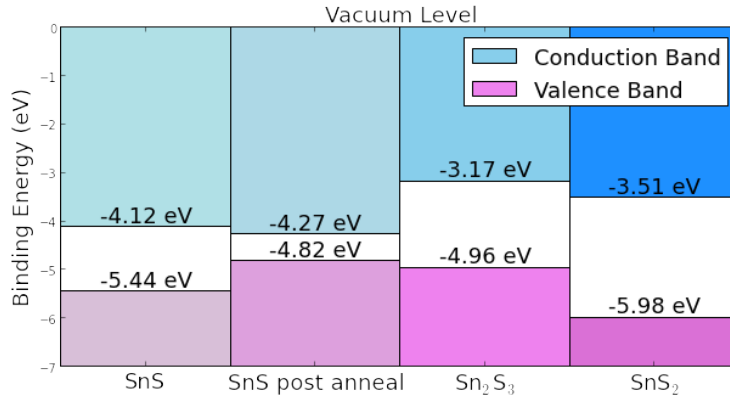


Figure 4-4: Band edge analysis with UPS and IPES, where the numbers indicate the position of the energy band relative to the vacuum level.

Table 4.2: UPS/IPES determined properties for the tin sulfide phases.

Property (eV)	SnS	SnS post-anneal	SnS ₂	Sn ₂ S ₃
Electron affinity	-4.12	-4.27	-3.50	-3.17
Work function	-4.56	-4.24	-4.36	-4.13
Ionisation potential	-5.44	-4.82	-5.98	-4.69
Band gap	1.32	0.55	2.47	1.79

material's Fermi level with respect to the vacuum level, or ionisation potential. IPES on the other hand, measures the kinetic energy of radiative processes of absorbed electrons, using a 1.04 filament current, giving 4 μ A flux at 10 eV kinetic energy and allows for the deduction of a materials electron affinity by filling previously empty electronic states. The combination of these properties allows for the construction of an energy band diagram for each tin sulfide phase, as shown in Figure 4-4, with the corresponding values listed in Table 4.2.

The XPS analysis revealed the presence of tin oxide in each of the three samples and elemental iodine adhered to the surface of the SnS crystal. The observation of iodine contamination of the SnS led to the deployment of an anneal procedure, subjecting the crystal to 300 °C for 10, 5, 25 and 15 minutes, in an attempt to remove the iodine. Unfortunately,

the anneal resulted in an almost metallic surface, as shown by the diminished band gap in Figure 4-4, without fully removing the iodine present. This is indicative of an ease of loss of sulfur in tin monosulfide, first observed in the previous chapter; see Section 3.1.1. The full data for XPS composition analysis can be found in the Appendix, Table A.3.

The band gap for SnS is close to the literature value for the direct band gap and is close in value to that found from UV/vis analysis, as is that of SnS_2 . The band gap for Sn_2S_3 is larger than that observed in the UV/vis analysis and is likely due to surface oxidation or the presence of SnS_2 impurities. Both UPS and IPES are sensitive to surface contamination, typically limited to 5 atomic layers analysis depth.¹⁹⁹

Sputtering with an ISIS 3000 Ar^+ ion sputter system, with an argon overpressure of 6×10^{-6} mbar for ten minutes was found to be ineffective in removing adventitious carbon, which is problematic as the UPS measures the smallest work function of a surface, no matter how small the area with this work function.

A previous photo emission measurement placed the work function of SnS 4.2 eV below the vacuum level for a (001) terminated single crystal,²⁰⁰ and SnS_2 has been reported to have an electron affinity of -4.1 eV,²⁰¹ both of which are in good agreement with the results presented here. However, the Fermi level for the SnS result was reported near the conduction band, which for an intrinsically *p*-type material suggests significant surface band bending (electron accumulation) or impurities present. As such, it is more probable that the larger work function seen in this thesis, better reflects the true nature of SnS. Little data exists in the literature on the electronic energy levels present in Sn_2S_3 .⁵⁰

4.2 Density function theory analysis

The UPS/IPES analysis reported previously, highlighted the difficulty in arriving at accurate opto-electronic properties for a multiphasic system such as that of tin sulfide. In

this section, the results obtained from DFT simulations are presented to compare directly with the experimental measurements. This work begins with the electronic structure, band gap and work function of SnS, continues to consider the properties of the alternate phases and then concludes by suggesting optimal PV device contacts for SnS, by building on the results presented in Section 3.2.6.

4.2.1 Band gaps & work functions for all phases

For the following calculations the structural parameters were held fixed at the experimentally determined values detailed in Section 3.2.1, in order to avoid errors due to the van der Waals interactions, which are small but not negligible for these pseudo-layered structures. The band gaps resulting from hybrid calculations performed with the VASP code with a 400 eV plane wave cut-off and the HSE06 functional, are 1.11 eV for SnS, 1.09 eV for Sn_2S_3 and 2.24 eV for SnS_2 . All of these band gaps are indirect in nature and agree well with the band gaps reported in the literature (Table 4.1) and those found by single crystal analysis. These results support the conclusion that the relatively large band gap found for Sn_2S_3 in the UPS/IPES analysis is due to the presence of surface impurities.

In order to align the electronic band energies to the vacuum level, the non-polar (001) surface of SnS, a reconstructed (001) surface of Sn_2S_3 , and the (001) surface of SnS_2 were used as surface slab models with a 15 Å vacuum spacing. The slab thickness was rigorously checked for convergence with respect to the vacuum potential. These surfaces correspond to the known dominant terminations for SnS and SnS_2 , with little information available in the literature for Sn_2S_3 .^{50,202}

The mapped electrostatic potential including the reference energy vacuum level is shown in Figure 4-5. For SnS, the associated surface ionisation potential is calculated to be -4.67 eV, -4.69 eV, and -4.70 eV for 2, 4, and 8 atomic bilayers, respectively. With

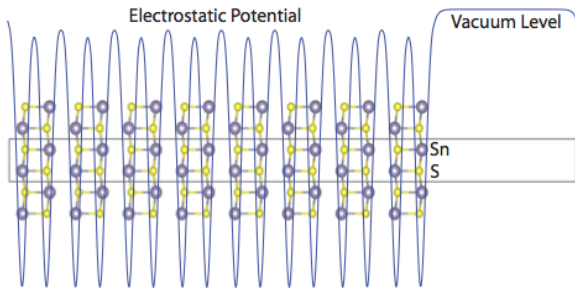


Figure 4-5: Cross section of the calculated electrostatic potential for a (001) terminated slab of SnS.

further increases to the calculation size providing no further change in energy *i.e* the 8-bilayer slab is fully converged. For SnS, the contribution of the surface to the calculated ionisation potential is found to be small, that is to say that when the vacuum level is aligned to the core level energies in the centre of the slab, rather than the valence band maximum directly, the ionisation potential is not modified to within 0.02 eV.

Again, the derived valence band maxima, conduction band minima and vacuum potentials allow for the construction of a band offset diagram for each of the tin sulfide phases, which is shown in Figure 4-6. The reported values for the successful photovoltaic material CZTS are included for comparison. SnS and Sn_2S_3 are both reported to be *p*-type semiconductors;²⁰³ hence, the equilibrium Fermi level will be placed close to the valence band edge, and the work function and the ionisation potential should be close in energy. Conversely SnS_2 is reported to be an *n*-type material,¹⁸⁵ meaning that its work function will be close in energy to its electron affinity.

The predicted ionisation potential of SnS is lower than that typically found for metal-chalcogenide semiconductors,²⁰⁵ which can be explained by the unusual coordination environment and inter-layer repulsion, caused by low binding energy Sn $5s^2$ orbitals. In this lower oxidation state of Sn (*i.e.* 2^+), the $5s^2$ orbitals are formally occupied, with the

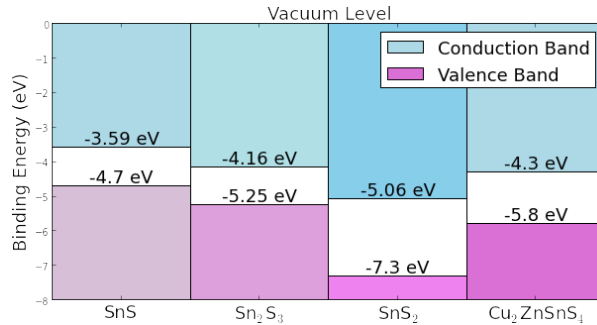


Figure 4-6: Calculated band offset diagram, using the HSE06 functional, for each of the three tin sulfide phases, and that of CZTS for reference, using a vacuum level alignment procedure.²⁰⁴

conduction band formed from the empty 5p band. The interaction of Sn 5s and S 3p results in anti-bonding states at the top of the valence band.²⁰⁶ In contrast, the ionisation potentials of CdTe and CuInSe_2 have been reported as -5.7 eV from UPS²⁰⁷ and HSE06 calculations.²⁰⁸ These values are also close to those found for CZTS and related selenide materials.²⁰⁹

4.2.2 Band structure of SnS

It is possible to derive more detailed information about the energy bands of a solid from DFT other than the band gap and work function. In order to fully understand the electronic structure of SnS, additional factors must be taken into consideration. Firstly, it is common practice to perform solid state calculations in reciprocal space as this allows for the repeating periodic functions in real space to be treated more easily in the frequency domain. Just as with real space, a conventional unit cell can be defined in reciprocal space as having no overlap with respect to translation when describing a periodic structure. The so-called Wigner-Seitz cell about a lattice point in real space, is the region of 3D space that is closer to that point than to any other lattice point. The first Brillouin zone is the Wigner-Seitz cell

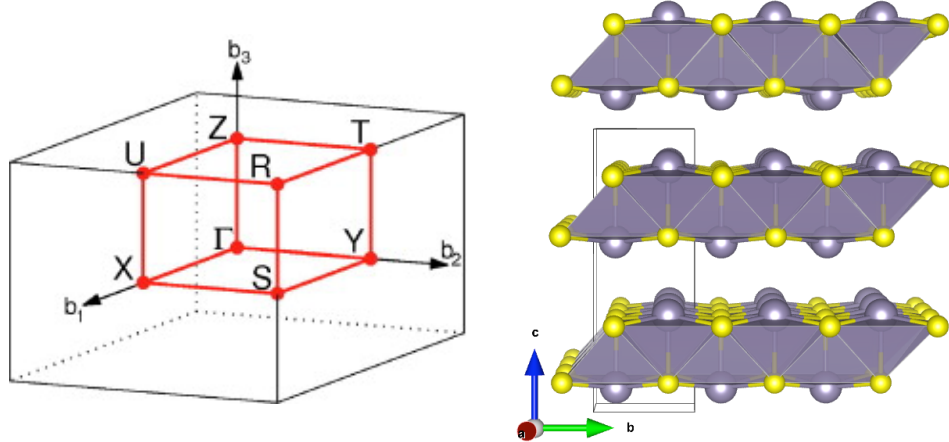


Figure 4-7: The Brillouin zone of the orthorhombic SnS system (left) and the corresponding real space unit cell with the defined axes vectors (right).

of the reciprocal lattice, with the same symmetry operations of the conventional unit cell. As such, it is possible to describe all of the electronic states in a solid within the Brillouin zone. If this zone is sampled or mapped on to a 2-dimensional representation of energy against zone coordinate, it is called a ‘band structure diagram’.

The optimal routes for sampling the Brillouin zone, that allow for the inclusion of high-symmetry ‘special points’ and other key regions of the electronic structure, have been specified for each different symmetry type.²¹⁰ The Brillouin zone and the sample path for SnS are shown in Figure 4-7, which are the coordinates directly mapped to the band structures shown in Figure 4-8. The corresponding real space representation of SnS is also shown in Figure 4-7, with an extended structure to highlight the pseudo-layered nature of SnS. It should be noted that Γ -X, Γ -Y and Γ -Z paths in the Brillouin zone (and the band structure) correspond to wave vectors in the a , b and c crystallographic directions in real space, respectively.

Now it is possible to see in the first panel of Figure 4-8 that SnS exhibits a fundamental electronic band gap of 1.11 eV in Γ -X that is spatially indirect, and a direct gap of 1.22

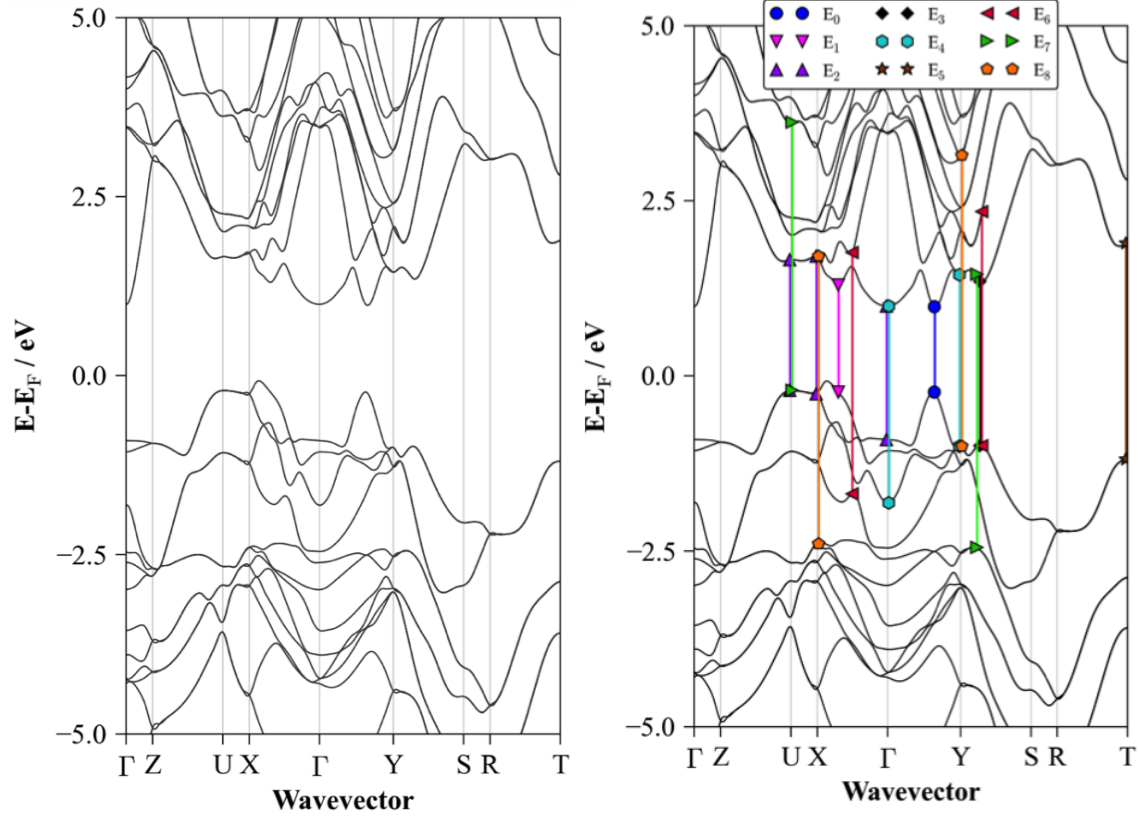


Figure 4-8: Band structure analysis for SnS at the HSE06 level of theory. The high resolution band structure showing a fundamentally indirect gap in Γ -X and a direct gap in Γ -Y (left) and critical point transitions mapped on to the same band structure (right). The top of the valence band is set to 0 eV.

eV in Γ -Y. Conversely it is possible to see that Γ -Z has a large gap with a relatively flat valence band maximum, given that the degree of dispersion of an energy band in a given direction characterises the strength of the bonding interactions along that vector, it can be said that the layers of SnS are weakly bonded. These results are significant as they show that the photon absorption mechanisms for SnS will (at the onset of absorption at least) occur in the bonding a, b plane, highlighted in Figure 4-7, rather than across the SnS pseudo-layer. The band diagram of SnS agrees well with the work of others from similar levels of DFT.^{211,212}

4.2.3 Temperature dependent electronic structure of SnS

For the single crystal of SnS, a change in band gap was observed as a function of temperature that indicated a possible switch in absorption mechanism. Density functional theory calculations correspond to solids at zero Kelvin as neither thermal expansion nor electron-phonon interactions are accounted for. As such, a method of approximating the effect of temperature on the electronic structure of SnS was identified, in order to more fully explore this relationship. Such calculations have proven insightful for the temperature dependent properties of other chalcogenide semiconductors in the literature, for example PbTe.²¹³

While the constant volume free energy of a system, Helmholtz energy (A), is given as

$$A(T, V) = E_0(V) + U_v(T, V) - TS_V(T, V) \quad (4.2)$$

where E_0 is the internal energy, $U_v(T, V)$ is the vibrational internal energy (which equates to the zero point energy at zero Kelvin) and S_V is entropy, only E_0 is available directly from DFT.

Phonons, or lattice vibrations, can be found from the changes in atomic forces from the displacement of atoms in the system away from their equilibrium position. The forces

are fitted to a harmonic potential energy surface in order to obtain force constants.

With the knowledge of the vibrational modes of a system, a partition function Z can be found *via*

$$Z = \exp(-U/k_B T) \prod_{k,\lambda} \frac{\exp(-\omega(k\lambda)/2k_B T)}{1 - \exp(-\omega(k\lambda)/k_B T)} \quad (4.3)$$

where U is a potential energy of the system, ω is the phonon frequency and the product is over vibrational modes, λ , and reciprocal-space wave vectors, k . The free energy can then be obtained by

$$A = -k_B T \log Z \quad (4.4)$$

Within a harmonic potential, the only temperature dependence is from the phonon occupation numbers, while the equilibrium distance between atoms is temperature independent. Lattice thermal expansion, however, can be accounted for within the quasi-harmonic approximation, which assumes that phonon frequencies are volume dependent, but that, at a given volume, the inter-atomic forces are still harmonic. It has been found that thermal expansion can be accounted for within this approximation reasonably up to half of the melting temperature of a material and, for SnS, a phase change is not observed up to more than 878 K.^{149,214}

A quasi-harmonic lattice dynamics calculation was performed by finding the phonon density of states of SnS for a range of expansions and compressions around the 0 K (relaxed) volume. The constant-volume free energy for each expansion and compression is evaluated as a function of temperature and energy - volume curves constructed, in order to find the equilibrium volume according to an equation of state. For SnS, these are shown in Figure 4-9,²¹⁵ and the resulting unit cell volume as a function of temperature plot, is

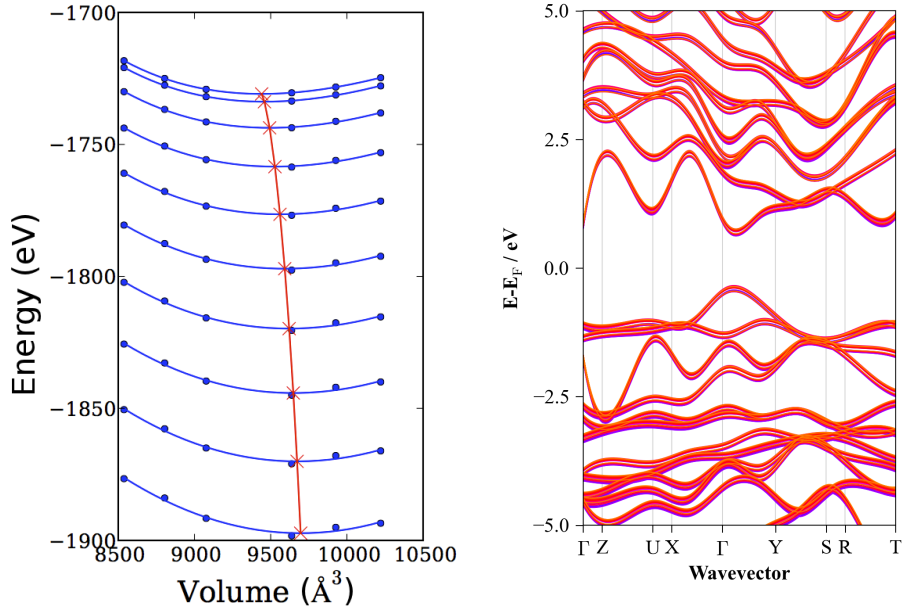


Figure 4-9: SnS free energy volume curves, showing the shift in supercell volume as a function of temperature (left) and a temperature dependent band structure showing little change of the electronic configuration with respect to thermal expansion (right), from 10 K in purple to 350 K in orange.

shown in Figure 4-10.

With the volume as a function of temperature identified, the band structure was calculated following the previous procedure for the volumes corresponding to between 10 and 350 K in steps of 10 K. These band structures are collated in Figure 4-9, with the corresponding band gaps shown in Figure 4-10.

The lower resolution of the band structure diagrams, shown in Figure 4-8, was necessary in order to complete such a large number of calculations at the hybrid level, but still show that the electronic structure is resilient with respect to change in thermal expansion. Similarly, the band gaps in Figure 4-10 show a small, linear increase in energy as

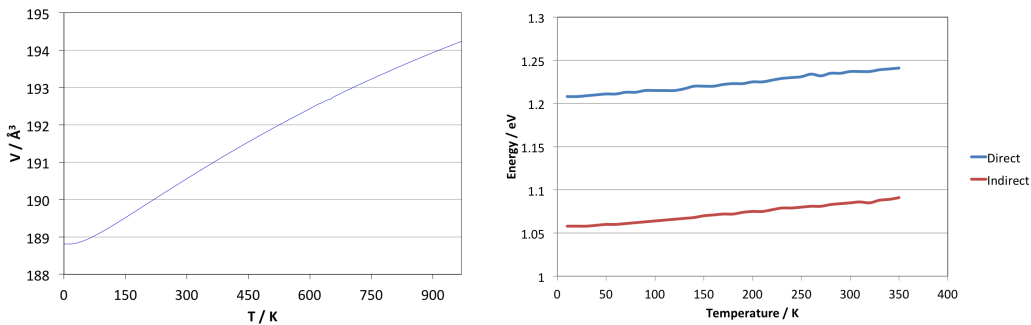


Figure 4-10: Temperature dependence of the SnS unit cell volume (left) and band gap (right).

‘temperature’ increases.

It should also be noted that no negative frequency phonons were obtained in this treatment of *Pnma* SnS, indicating that it is dynamically stable and, hence, the ground state configuration of tin monosulfide.

4.2.4 Dielectric function of SnS

This section details theoretical work accomplished in collaboration with colleagues at Pennsylvania State University in the USA, who successfully synthesised single crystals of SnS using the Bridgman-Stockbarger method. These crystals were characterised by colleagues at the National Renewable Energy Laboratory (NREL), also in the USA.²¹⁶ See the Section Acknowledgements, for full details.

It is possible to calculate the frequency dependent dielectric matrix from the ground state electronic configuration, *i.e.* the band structure presented in Figure 4-8. This property details the anisotropic permittivity of a material with respect to charges generated under illumination. It is calculated by the treatment of an independent particle promoted between electronic bands and, as such, to ensure sufficient accuracy, the calculations included 240 bands, only 40 of which were occupied. Specifically, these parameters were calculated

within the electric dipole approximation from the real and imaginary hybrid Kohn-Sham eigenstates.

The frequency dependent dielectric function has two components, the real and the imaginary functions. The imaginary part, ε_2 is found by²¹⁷

$$\varepsilon_2(\omega) = \frac{4\pi^2 e^2}{\Omega} \lim_{q \rightarrow 0} \frac{1}{q^2} \sum_{c,v,k} 2w_k \delta(\varepsilon_{ck} - \varepsilon_{vk} - \omega) \times \langle u_{ck+c\alpha q} | u_{vk} \rangle \langle u_{ck+c\beta q} | u_{vk} \rangle \quad (4.5)$$

where c and v refer to the conduction and valence band states respectively and u_{ck} is the cell periodic part of the orbitals at the k -point, k , with a weighting factor, w_k . ω is the frequency of the incident photon, Ω is the volume of the unit cell and q is the Bloch vector of the incident wave.

The real part of the dielectric tensor, ε_1 , is obtained using the Kramers-Krönig transformation

$$\varepsilon_r(\omega) = 1 + \frac{2}{\pi} P_v \int_0^\infty \frac{\varepsilon_r^2(\omega') \omega'}{\omega'^2 - \omega^2 + i\eta} \quad (4.6)$$

where P_v denotes the principal value and η is the complex shift.

The dielectric functions derived from theory and obtained for the single crystal SnS using variable angle spectroscopic ellipsometry (J. A. Woollam Inc. M2000-DI model) are shown in Figure 4-11. The agreement between the two is clear in each of the three crystallographic directions a , b and c as labelled (see Figure 4-7)

The dielectric function, or permittivity, is defined as the measure of the resistance that is encountered when forming an electric field in a medium. As such, the greater the value of the dielectric the more stable the charge generated within a photoactive material upon exposure to light. The static and high frequency dielectric constants are listed in Table 4.3

Table 4.3: Calculated high frequency (ϵ_∞) and static (ϵ_0) dielectric constants of SnS (from HSE06-DFT). The ionic contribution to the response (ϵ_{ion}) is calculated using the phonon dispersion from density functional perturbation theory.

Property	ϵ_a	ϵ_b	ϵ_c
ϵ_{ion}	21.36	37.64	22.72
ϵ_∞	12.70	14.02	11.85
$\epsilon_0 = \epsilon_{ion} + \epsilon_\infty$	34.06	51.66	34.57

along with the total dielectric resulting from the two. Here, it can be seen both with the dielectric functions (real and imaginary), and the dielectric constants, that the permittivity is greater along the b direction than in either a or c and would represent a preferential direction of charge transport in tin monosulfide.

Furthermore, this close agreement between DFT and the variable angle spectroscopic ellipsometry experiment allows for the direct mapping of key transitions on to the band structure of SnS (Figure 4-8). This is possible as the second order differential of the dielectric function allows for the identification of so-called ‘critical points’, which are shown in Figure 4-12, with a reported total of 9 points from the experimental data. As these transitions are most likely to occur for high symmetry points in the Brillouin zone, it is possible to then map the special points shown in Figure 4-7 back on to the single crystal dielectric function, as shown in the first panel of Figure 4-11. In this way, high levels of agreement and compatibility can be found between theory and experiment. At the very least, this practice allows for the conclusion that the agreement between the chosen level of DFT and single crystal experiments is high. It is expected therefore that properties derived from the HSE06 functional for semiconductor materials are, to all reasonable approximations, accurate.

The critical points mapped on to the direction dependent band structure highlight once again that the majority optical activity occurs in the bonding plane, with few transitions associated with eigenstates propagating in the c direction.

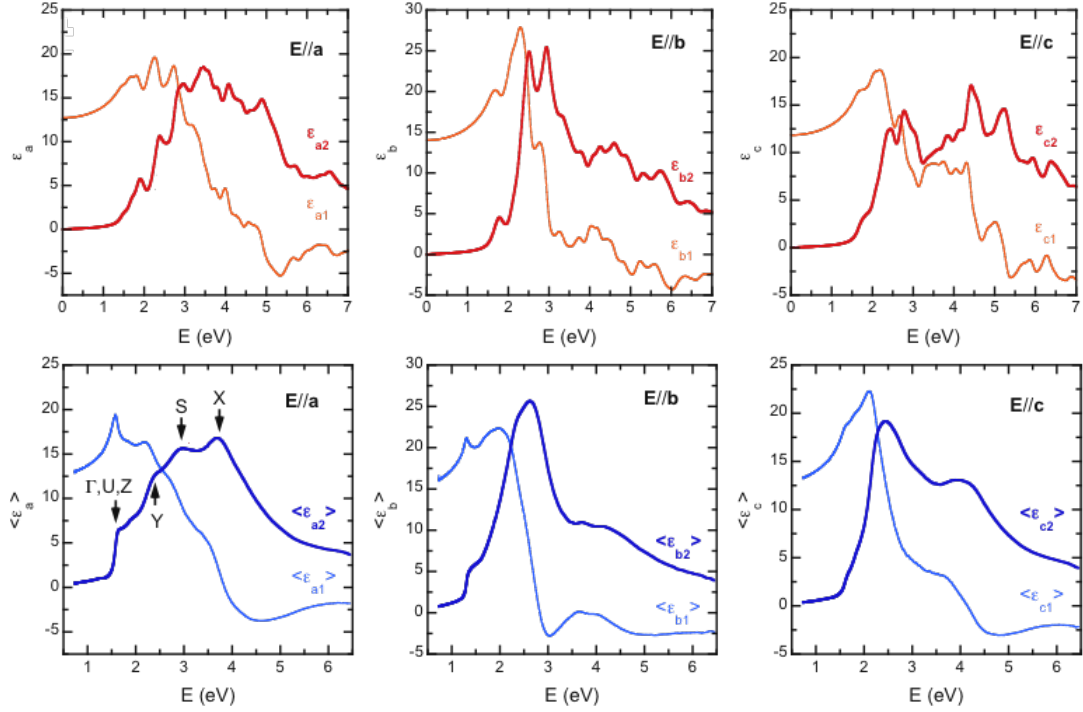


Figure 4-11: Calculated and spectroscopically determined dielectric spectra for the three principal crystallographic axes. Calculated data are presented along the top with single crystal data along the bottom. The real part is labelled as $\epsilon_x 1$ and imaginary part as $\epsilon_x 2$ where x is the direction.

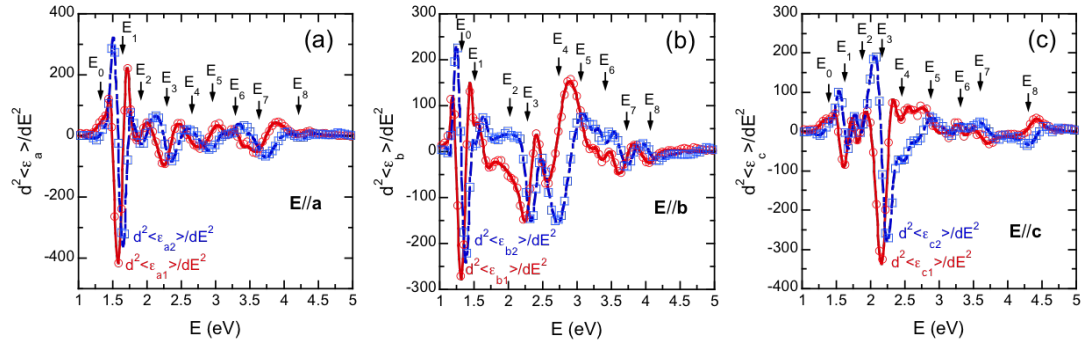


Figure 4-12: Real (red solid) and imaginary (blue dashed) second derivative dielectric data indicating standard critical point line shapes by best fit. The energies of each critical point are indicated by arrows and labelled in a numeric order.

4.2.5 Absorption coefficient of SnS

For direct comparison with single crystal data, it is also possible to calculate the absorption coefficient of a material based on the real and imaginary dielectric functions presented in the previous section, according to

$$\alpha = \frac{\frac{2E}{h} \frac{\sqrt{2}}{2} \sqrt{(\varepsilon_1^2 + \varepsilon_2^2)^{0.5} - \varepsilon_1}}{c} \quad (4.7)$$

where c is the speed of light, h is Planck's constant and E is energy.¹³⁶ For the DFT dielectric functions the calculated anisotropic absorption coefficient as a function of incident energy is shown in Figure 4-13 for the a , b and c crystallographic directions. This yields the expected steep gradient for photon absorption above the band gap value of SnS which is in good agreement with experimental literature that shows optical absorption reach higher than 10^5 cm^{-1} at greater than 1.5 eV.²¹⁸

In this graph, it is possible to confirm the earlier prediction of stronger absorption in the bonded plane (a and b) rather than perpendicular to it (c), as discussed in the previous section, and also in Section 4.2.2.

The Python code written to produce the anisotropic absorption coefficient as a function of incident energy, as shown here for SnS, can be found in the Appendix, Section A.4.

4.2.6 Assessment of potential device back contacts for SnS

Earlier in this thesis (Section 3.2.6), it was shown that SnS is likely to react with the much-used back contact molybdenum. It has also been shown that SnS has a relatively low work function compared to other photoactive materials. The final results section of this chapter seeks to address the questions: is the reactivity of SnS limiting current device performance and are there more suitable alternatives?

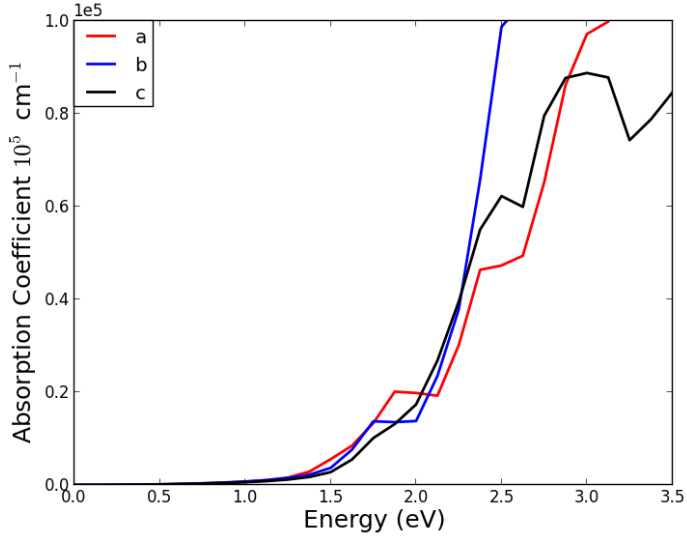


Figure 4-13: Optical absorption coefficient derived from DFT, pertaining to the crystallographic axes as labelled.

Ample work in experiment has focused on the optimisation of the buffer layer, *i.e.* top contact of SnS,¹⁷⁷ while relatively little work has been done on the device back contact, a device component of equal importance. One paper reports the use of copper as an electrode in such a device,²¹⁹ which, while desirable, due to abundance and cost factors, is likely to result in the formation of a CuSnS_x mixed phase instead. Besides this, the obtained efficiencies did not offer an improvement over the use of standard contacts.²²⁰

Devika *et al.* showed that Al, In and Sn (but not Ag) all formed Ohmic contacts with SnS,²²¹ demonstrating a potentially fruitful avenue of device research as yet unexplored for this material. Here the focus remains on Mo, Sn, Ti and W as contact metals as the potential benefits of SnS are negated if rare or expensive elements are incorporated into the same device.

Tin monosulfide is known to exhibit *p*-type conductivity,²²² where the majority charge carriers (holes) are collected at the back contact. As such, the work function of the back

contact for SnS must be smaller than that of SnS to allow proper extraction of holes.²²³ The earlier sections of this chapter have shown that SnS already has a relatively small work function compared to CZTS and literature values of CdTe or CuInSe₂.²²⁴ From this, one can predict that molybdenum might be an unsuitable contact for SnS, despite the fact that the record efficiencies for this material are published with this device architecture.²²⁵

While it was shown in Chapter 3 that the metals considered here, excluding tin, are likely to form interfacial disulfide layers, the effect that these layers may have on device performance is unknown. For example the presence of MoSe₂ has shown to be beneficial for CIGS cell performance, while the effect of MoS₂ formation in CZTS devices remains unclear.^{174,226}

Metals are characterised by high conductivity and mobile electrons. The work function of a metal is the difference between the Fermi level and the vacuum level, which determines the barrier height at a metal-semiconductor junction. The calculated work functions for the selected metals at three major crystallographic terminations are reported in Table 4.4, along with collected values from the literature. Agreement between experiment and theory is found across these values, with the possible exception of that for polycrystalline titanium metal. This could be explained by the presence of higher work function planes in the crystal that are not accounted for here and the fact that (as seen in this report) it is difficult to measure a work function accurately from surface sensitive techniques.

The electronic properties were also calculated for the metal disulfides, as shown in Table 4.5, again with good agreement with experiment. In these calculations, the termination is taken as the clean (001) as each disulfide forms a 2-dimensional structure with relatively weak van der Waals layers in the *c* axis. The values of the work function for each of these is greater in magnitude than either the work function of the metals shown in Table 4.4 or those of SnS. As such, our results indicate that any disulfide inter-layers would behave as hole blocking layers, preventing efficient charge extraction from SnS and limiting perfor-

Table 4.4: Calculated work functions (ϕ) for the corresponding metal surfaces at the HSE06 level of theory. All values are in eV with respect to the vacuum level and are compared with those in literature.⁹⁹

Metal	DFT			Experiment (where available)			
	(100)	Surface (110)	(111)	(100)	Surface (110)	(111)	poly crystalline
Mo	-3.76	-4.82	-3.81	-4.53	-4.95	-4.55	—
Sn	-4.96	-4.65	-4.49	—	—	—	-4.42
Ti	-3.23	-3.20	-3.25	—	—	—	-4.33
W	-4.26	-5.19	-4.07	-4.63	-5.22	-4.45	—

mance. All of these results are shown in alongside one another in a hypothetical contact arrangement *i.e* with the disulfide placed between the SnS and metal, in Figure 4-14.

However, the nature of the metal disulfides is also of significance, as the conductivity type places the work function of a material either close to the valence band maximum, for *p*-type, or close to the conduction band minimum, for *n*-type, materials. MoS₂ is predominantly *p*-type,⁵⁰ which places the work function of MoS₂ more than 1 eV lower than that of SnS. This would act to block hole extraction for SnS, but would form a non-detrimental contact with CZTS, which has a predicted work function energy also around 1 eV below SnS (see Figure 4-6). This agrees well with alternate analysis for CZTS.²²⁶

WS₂ is reported as *n*-type,⁵⁰ which would oppose the rectifying behaviour needed in a PV device and, combined with the favourable formation enthalpy of WS₂ shown in Table 3.10 of the previous chapter, almost precludes tungsten as a suitable contact.

SnS₂ is also known to be *n*-type²²² but the results from earlier indicate that SnS₂ would not spontaneously form with SnS in contact with tin metal.

Finally, TiS₂, is reported to be a semi-metal,²²⁷ which, itself, would pose no detriment to the workings of a PV cell, however the energy levels are much too low to be suitable as a contact in an SnS PV device.

If assessed purely by principles of band alignment, and excluding potential metal disul-

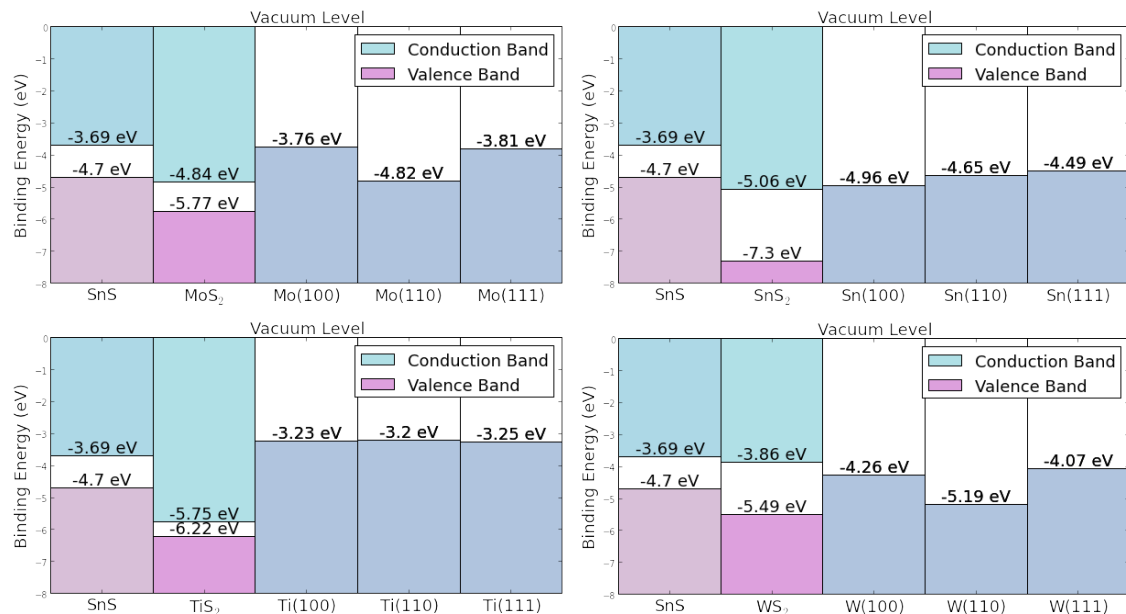


Figure 4-14: Calculated band offset diagram, using the HSE06 functional, for hypothetical tin sulfide contacts with indicated metal surfaces. The effect of any interfacial states is not accounted for.

Table 4.5: Bulk band gaps and ionisation potential for respective metal disulfides calculated with HSE06. Note that the ionisation potential and work function for a *p*-type material are close in energy, where the Fermi level lies at the top of the valence band.

Species	Bandgap (eV)		Ionisation Potential (eV)	
	Theory	Exp.	Theory	Exp.
MoS ₂	0.93	1.29 ²²⁸	-5.77	-5 ²²⁹
SnS ₂	2.24	2.2 ¹⁸⁶	-7.30	7.18 ²³⁰
TiS ₂	0.47	0.3 ²³¹	-6.22	5.8 ²³²
WS ₂	1.63	1.4 ²³³	-5.49	5.1 ²³⁴

fide formation, SnS(100) would be most likely to form an Ohmic contact with the Sn(110) surface. If one considers the thermodynamic driving force for contact degradation from the previous chapter and the likely effect of such a reaction, tin also offers the most ideal contact, as degradation is unfavourable. This prediction could pave the way for tin-only devices, with tin metal, SnS, SnS₂ and fluorine doped tin oxide forming a self-contained device, easily synthesised and mass-produced.

4.3 Results comparison & discussion

The fundamental band gaps presented in this chapter, for each of the tin sulfides, are shown in Table 4.6. It can be seen that the magnitude of the band gap is larger in experiment, for each case, than is reported from the hybrid level electronic structure calculations. While such discrepancies are often ascribed to the lack of thermal considerations in DFT, it has been shown in this chapter that such discrepancies are unlikely to be due to the effects of temperature. Instead, it is proposed that these variances are to be expected to a certain degree, given that DFT provides the fundamental band gap directly, whereas experimental methods rely on extrapolation after absorption or emission has already begun to occur.

While DFT predicts an increase in band gap with increasing temperature, in direct con-

Table 4.6: Obtained fundamental band gaps of the tin sulfides using UV/vis, UPS/IPES and HSE06 methods. All values are in eV.

Phase	fundamental band gap		
	UV/vis	UPS /IPES	HSE06
SnS	1.47	1.32	1.11
SnS ₂	2.42	2.47	2.24
Sn ₂ S ₃	1.20	1.79	1.09

tradiction to experiments that show the inverse relationship; this can be trivially attributed to crystal phonons activating more optical transitions in the crystal. For SnS, the direct band gap from theory (1.22 eV) and the 4 K band gap from the FTIR experiment (1.21 eV) show exceptional agreement with one another. Similarly, the indirect gap from DFT (1.11 eV) and that of 300 K from FTIR (1.14 eV) also agree well. These two values are the most directly comparable conceptually and their excellent agreement shows the suitability of the chosen simulation methods in this project.

However, the suggested practice of extrapolating DFT-obtained band gaps to room temperature values, outlined by Malone *et al.*,²¹² is flawed. The method does not account for the change in direction of the onset of absorption that is observed in the single crystal data below 100 K here, and, as such, is inapplicable to indirect band gap materials. That said, the agreement between these different levels of theory, for the ‘0 K’ band gaps at least, corroborate the HSE06 results in Table 4.6.

The results of this chapter also highlight the difficulties associated with relying on surface sensitive techniques, *i.e.* UPS/IPES in this case, for obtaining bulk crystal electronic properties. It has already been discussed that the placement of the Fermi level with respect to the vacuum is dependent on the defect concentration, and defect type, within crystals and thin-films. Without proper quantification of intrinsic and extrinsic defects of a system, as well as their relative electronic effects, it is difficult to accurately report reliable results for these techniques. Similarly, surface contamination, likely to occur almost immediately

upon exposure to atmospheric condition for the tin sulfides discussed in this project, is another source of uncertainty. However, the placement of the energy levels for the single crystals do still indicate that the sesqui- and disulfide phases will hinder the photovoltaic performance of SnS in a device, as do the results obtained from DFT.

According to the band edge analysis from the UPS/IPES method, Sn_2S_3 would act as a hole trap, and SnS_2 would act as both a hole and electron block if either were to occur in localised regions of SnS bulk. As a 2-dimensional material, if SnS_2 were to form as a layer between the top or bottom contacts of SnS, then device performance would be severely limited. Indeed, the formation of SnS_2 interlayers between SnS and common device components has been observed in the literature,¹⁷⁵ and is of great concern for this system.

From DFT, the lowest ionisation potential is found for SnS (Figure 4-6), with a monotonic increase from Sn_2S_3 to SnS_2 . Similarly, the electron affinity increases from 3.59 eV for SnS, to 4.16 eV for Sn_2S_3 and 5.06 eV for SnS_2 . This is a more intuitive result than those seen from the single crystal analysis, as increasing the ratio of sulfur in the solid, a more electronegative element than tin, allows for the material to hold its electrons more strongly.

The calculations predict that the $\text{SnS}/\text{Sn}_2\text{S}_3$ and $\text{Sn}_2\text{S}_3/\text{SnS}_2$ interfaces would form *p-n* junctions of a staggered nature, driving the separation of electrons and holes. The local presence of Sn_2S_3 would act as an electron trap, providing a reduction in energy in the conduction band that would need to be again overcome before the electron could be extracted. The alignment between SnS and SnS_2 is also problematic as it shows a so-called ‘broken gap’ heterojunction, indicating that spontaneous electron transfer would occur from the valence band of SnS to the empty conduction band of SnS_2 .²³⁵ With respect to solar cells, the presence of these impurity phases dispersed throughout an SnS layer (reported by multiple authors)^{93,132,236–238} would decrease device performance by mitigating

the desired rectifying behaviour across the cell. This could explain the limiting properties seen in PV cells as small-scale secondary phases and point defects have shown to be of macroscopic importance for $\text{Cu}_2\text{ZnSnS}_4$ (CZTS) devices.⁵⁸ As such, regardless of the preferred method of analysis presented in this thesis, the interpretation is that the presence of phase impurities ought to be suppressed as much as possible, in order to increase the efficiency of SnS devices.

Perhaps of greatest importance is the relatively low ionisation potential of SnS compared to other photo absorbers (*e.g.* CZTS). This result suggests that the valence band and conduction band of SnS are mis-aligned with those of common contacts, as the valence band energy of SnS equals the conduction band energy of CuInSe_2 and approaches the conduction band energy of CdS, according to literature values.²²⁴ As such, commonly used contacts such as molybdenum might not allow the effective extraction of charges necessary for PV performance.

It is possible that the formation of either SnS_2 or MoS_2 at device interfaces prevents the efficient extraction of charges necessary to yield an acceptable photovoltaic efficiency. Based on these findings; supported by both experiment and theory, it is possible to suggest a hypothetical photovoltaic device architecture to negate the weaknesses identified. Such a device ought to be made with tin as the contact metal, as this offers the best chance of mitigating contact degradation *and* offers the optimal energy level alignment for reported orientations of SnS.

While the presence of the sesqui- and disulfide phases in this report are treated as tin monosulfide impurities, the band off-set diagrams in this chapter suggest that a thin-film of Sn_2S_3 and SnS_2 could form an ideal photovoltaic heterojunction. At the very least it would appear that phase pure Sn_2S_3 should be further investigated as a photon absorbing material, given that its band energy levels are in closer agreement with CZTS than those of SnS.

Finally, a novel prediction arising from this work is that the (010) terminated SnS thin film would appear to be an optimal crystallographic orientation both in terms of optical absorption and charge carrier diffusion. This concept will be further explored in the subsequent chapter, however, in which charge transport will be explicitly investigated.

Chapter 5

Transport & defect properties

This chapter begins with a summary of the reported transport properties of SnS, SnS₂ and Sn₂S₃ from the literature and compares them with values obtained from single crystal analysis. The latter parts of this chapter present novel interpretations of results from DFT, in order to arrive at equivalent semiconducting properties. Once again, the comparison between the literature, experiment and theory, allow for the exploration of both the validity of selected theoretical methods and the properties of single crystals.

5.1 Single crystal analysis

5.1.1 Conductivity, mobility & related properties for all phases

Electrical resistivity is the degree to which a material opposes the flow of electricity. The inverse of this parameter is conductivity, a high degree of which is desirable for a photovoltaic component, as it allows for a greater electric current to be extracted from a device upon exposure to light.

Conductivity is proportional to the product of charge mobility and carrier concentra-

tion, where the mobility describes how quickly charges can move through a material and carrier concentration is the number of carriers in the valence and conduction band, from *p*- and *n*-type defects, respectively.

It has already been mentioned that SnS is a natural *p*-type material with hole-mediated transport. There is ample work supporting this conclusion in the literature; however, the values of relevant conducting properties vary. Reported conductivities range from 0.03 to $0.077 \Omega^{-1} \text{ cm}^{-1}$,^{79,181} carrier concentrations from 10^{15} to 10^{18} cm^{-3} , and hole mobilities from 4 to $139 \text{ cm}^2 \text{ V}^{-1} \text{ s}^{-1}$.^{50,180,181,239}

In contrast, SnS₂ is known to be an intrinsic *n*-type material. Reported conductivities range from 2×10^{-5} to $0.90 \Omega^{-1} \text{ cm}^{-1}$,^{50,240} carrier concentrations from 10^{13} to 10^{17} cm^{-3} , and electron mobilities from 15 to $52 \text{ cm}^2 \text{ V}^{-1} \text{ s}^{-1}$.^{50,240}

Finally, Sn₂S₃ has also been reported as an intrinsic *n*-type material with conductivities around $10^{-3} \Omega^{-1}$,¹⁹¹ carrier concentrations around 10^{15} cm^{-3} ,¹⁹¹ but with little information available for charge carrier mobilities.⁵⁰

All of these properties, listed in Table 5.1, are considered in this chapter, as it has already been established that multiple phases are likely to be present in a typical sample of tin monosulfide, indeed, SnS₂ impurities have even been observed in SnS samples only 30 nm thick.¹⁷⁵ While a wide range of these values is perhaps to be expected, considering the sensitivity of these parameters to synthesis conditions, there is still an underlying dependence on intrinsic materials properties. For example, each of the tin sulfide phases is expected to be anisotropic both in their crystal structure and electronic properties, and so different sample orientations could be a cause of the high degree of variability observed in charge mobilities in the literature.

Table 5.1: Reported electron transport properties for the tin sulfides, corresponding to each indicated reference.

Phase	Conductivity ($\Omega^{-1} \text{ cm}^{-1}$)	Carrier concentration (cm^{-3})	Mobilities ($\text{cm}^2 \text{ V}^{-1} \text{ s}^{-1}$)	Ref.
SnS	0.077	1.2×10^{15}	500	79
	0.069	1.16×10^{17}	3.73	180
	0.030	1×10^{15}	139	181
	–	1×10^{17}	385	241
	0.033	–	130	239
	–	3×10^{18}	90	64
SnS ₂	0.90	2×10^{17}	51.5	50
	2.4×10^{-5}	1×10^{13}	15	240
Sn ₂ S ₃	4.4×10^{-3}	9.4×10^{14}	–	191

5.1.2 Pulse-radiolysis time-resolved microwave conductivity

In order to assess transport parameters for the single crystal tin sulfides, pulse-radiolysis time-resolved microwave conductivity (PR-TRMC) measurements were performed. This method relies on the fact that the formation of mobile charges induces a rise in the electrical conductivity, which results in increased microwave absorption. The reduced amount of microwave power is detected on a nanosecond time scale and allows for the characterisation of conductivity.

In PR-TRMC experiments, charges are generated in the sample by irradiation with high-energy electrons. The SnS, SnS₂ and Sn₂S₃ samples consisted of micron-sized crystallites that were diluted approximately ten times by mixing them with polymethyl-methacrylate (PMMA) powder.

In order to measure the conductivity, the sample is inserted into a microwave conductivity cell with the dimensions of a rectangular K_a band microwave wave guide. The tin sulfide samples were irradiated with nanosecond electron pulses of 3 MeV. The incident high-energy electrons undergo scattering within the sample and transfer energy by

inducing ionisations. In this way, a close to uniform distribution of holes and electrons is produced. The penetration depth of 3 MeV electrons is approximately 1.5 cm, which exceeds the thickness of the microwave cavity (0.5 cm); hence, the incident 3 MeV electrons pass through the sample and charging does not occur.

After the nanosecond electron pulse, the change in conductivity of the sample is probed as a function of time by monitoring the attenuation of reflected microwave power between a frequency of 28 and 38 GHz, with a maximum electric field strength in the sample of 10 V m⁻¹. The fractional change in microwave power reflected by the cell ($\frac{\Delta P}{P}$) is directly proportional to the change in conductivity, $\Delta \sigma$, according to

$$\frac{\Delta P}{P} = A\Delta\sigma = Ae \sum_i \mu_i N_i \quad (5.1)$$

in which A is the sensitivity factor, N is the concentration of charges and μ their mobility. The initial value of N can be deduced using dosimetry measurements combined with an estimate of the average energy required to generate one electron-hole pair. Knowledge of N allows quantification of μ .

Unfortunately, this method, when applied to SnS, did not allow for the extraction of conductivity data, unlike for the single crystals of SnS₂ and Sn₂S₃, which will be discussed after the following analysis for SnS. The absence of data for SnS can be explained by a high dark conductivity of the tin monosulfide crystals, *i.e.* the conductivity in the absence of a pulse was too high to characterise a noticeable Fermi-level splitting when using the microwave measurements. The origin of this behaviour is nonetheless still instructive as to the nature of SnS.

Firstly, it should be noted that conductivity depends on carrier concentration, *i.e.* the more defects present, the higher the carrier concentration and the higher the conductivity. It should also be noted that a materials' Fermi-level is defined as the energy up to which

the population of states occurs. Where there is a distribution of states, *i.e.* all materials above 0 K, the Fermi level is defined as the chemical potential of the electrons, which will fall in the band gap for a non-degenerate semiconductor. If a material is highly defective, it is said that the bands are no longer in equilibrium and carrier populations can no longer be described by one Fermi level. Instead two Fermi levels are employed, one for the states in or near the bottom of the conduction band and one for the states in or near the top of the valence band. These are called quasi-Fermi levels and correspond to electrons and holes, respectively.

The problem is that PR-TRMC and photovoltaic activity both depend on splitting the equilibrium Fermi level to form these carrier quasi-Fermi levels upon exposure to light. If they are already displaced from equilibrium by the presence of a high concentration of defects, the illumination of a photoactive material in a device configuration will yield a diminished voltage.²⁶ This effect can be seen schematically in Figure 5-1, where increasing defect concentration further shifts the quasi-Fermi levels and restricts the voltage obtained. Indeed, such a scenario agrees well with the relatively low voltage output observed for the champion SnS cell.²⁴² As such, SnS devices might benefit from a reduction of the intrinsic conductivity, through control of the growth conditions or extrinsic doping.²²⁵

It is also possible that defects present in SnS, allow for exciton recombination via trap states located within the band gap, *i.e.* Shockley-Read-Hall recombination. In a particularly defective system with a high density of states within the band gap, it may be possible for the system to resist perturbation from an outside stimulus, in this case an electron pulse, via the recombination of existing free carriers. Such a scenario would yield no net change in carrier concentration, or subsequent change in microwave absorption, upon irradiation.

While the presence of extrinsic defects in these SnS samples was found to be high with the GDMS analysis presented in Chapter 3, these are to be expected to be present in each of

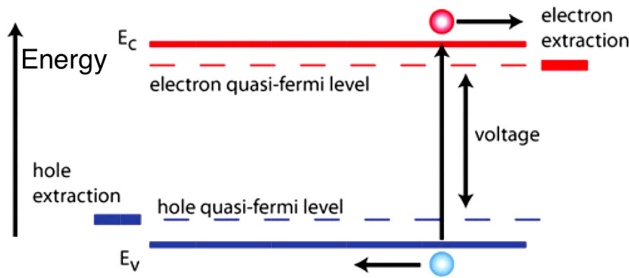


Figure 5-1: Energy level diagram depicting relationship between quasi-Fermi levels and maximum obtainable device voltage for a hypothetical intrinsic semiconductor. Increasing defect concentration within the band gap decreases the splitting of the quasi-Fermi levels and adversely affects performance. E_V and E_C are the energies of the valence band and conduction band, respectively.²⁴³

the three phases, as discussed in Section 3.2.5. The fact that SnS is the only crystal phase not to photo-excite during this analysis indicates that there is a large amount of intrinsic defects present, which are not seen in the other phases, a conclusion corroborated by the high reflectivity of SnS observed during the UV/vis analysis presented in Section 4.1.1. It is important to note that the GDMS technique used to arrive at this conclusion (see Section 3.1.2), does not allow for the characterisation or quantisation of intrinsic defects in these samples, which represents an interesting area of future research.

It may also be the case that the apparent tendency for tin monosulfide to lose sulfur over time forms regions of tin metal in the sample. Any metallic phase present in PR-TRMC analysis would allow for almost instantaneous charge recombination, and also lead to an absence of observable signal.

Returning to the results from the sesqui- and disulfide phases, the data produced for SnS₂ and Sn₂S₃ is shown in Figure 5-2. It can be seen that from the onset of the pulse, the signal rapidly increases due to the formation of mobile charge carriers. The maximum signal size can be converted into a mobility using Equation 5.1, yielding for both materials a value of the order of $150 \text{ cm}^2 \text{ V}^{-1} \text{ s}^{-1}$. These are comparable to the highest

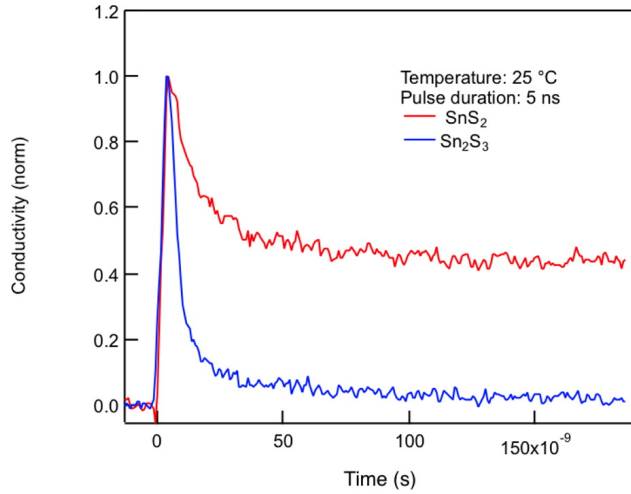


Figure 5-2: Normalised PR-TRMC traces recorded for SnS_2 and Sn_2S_3 using a pulsed 3 MeV electron beam, shown as a function of time.

values reported in the literature for these materials and suggest favourable properties for PV applications (see Table 5.1).

Directly after the pulse a fast decay is observed for both semiconductors; however, the decays are very different. The decay can be explained by the immobilisation of charge carriers due to, for example, electron trapping. Alternatively, recombination of charge carriers also leads to a reduction in signal size. For Sn_2S_3 , the signal decays to almost zero within a period of less than 50 ns. In contrast, the decay for SnS_2 is far slower and extends into the microsecond time scale.

The origin of the decay can be studied in more detail by changing the electron beam dose and comparing the dose-normalised PR-TRMC traces, as shown in Figure 5-3. For SnS_2 , the signal decreases more rapidly as the dose increases. This is a clear sign of charge-carrier recombination according to second-order electron-hole kinetics. For Sn_2S_3 , the decay is independent of the dose, indicating that trapping or recombination is a first-order process.

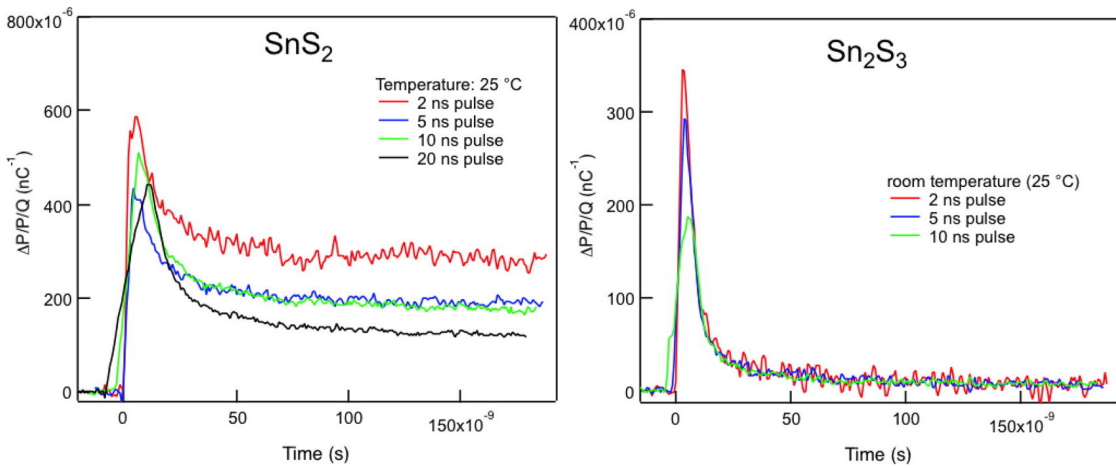


Figure 5-3: Dose-normalised change in conductivity for SnS_2 and Sn_2S_3 . The x -axis shows time in nano-seconds and the y -axis shows the fractional change in microwave power reflected by the cell divided by the integrated beam charge per pulse (Q) in nano-Coulombs.

At the lowest pulse of 2 ns, for SnS_2 , the lifetime ($\tau_{1/2}$) is 50 ns and the mobility (μ) is around $150 \text{ V}^{-1} \text{ s}^{-1}$, giving a mobility-lifetime product of $7.5 \times 10^{-6} \text{ cm}^2 \text{ V}^{-1}$. For Sn_2S_3 $\tau_{1/2}$ is approximately 5 ns and the mobility is around $150 \text{ V}^{-1} \text{ s}^{-1}$, giving a mobility-lifetime product of $7.5 \times 10^{-7} \text{ cm}^2 \text{ V}^{-1}$. These values are comparable with, but somewhat lower than, those found for the successful photoactive material CdTe ($7 \times 10^{-5} \text{ cm}^2 \text{ V}^{-1}$).²⁴⁴

The data for SnS_2 in Figure 5-4, shows that the signals do decay to zero, but only on a very long time scale. The low repetition rate of the accelerator of *ca.* 1 Hz would indicate that no charge-carrier accumulation occurs, and therefore the long lifetimes are attributed to the fact that the mobilities in different directions of the lattice are reported to vary by four orders of magnitude.²⁴⁵ This large anisotropy in mobility arises from the two-dimensional, sheet-like structure of the lattice in SnS_2 crystals *i.e.* the interaction of the highly energetic electrons of the accelerator pulse with the material induces the formation of charges over separate bonded ‘sheets’. Since the charge transport perpendicular to the sheets is slow,

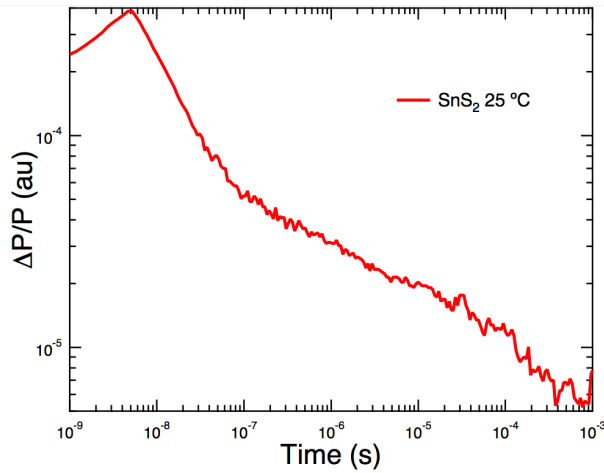


Figure 5-4: SnS_2 PR-TRMC signal decay as a function of time.

recombination of opposite charges is retarded, compared to that in an isotropic material.

Conversely, the rapid decay observed for Sn_2S_3 indicates a more isotropic conductivity where charges are able to spatially recombine. This is yet another indication of favourable properties for photovoltaic applications presented by Sn_2S_3 .

5.1.3 Hall-effect mobility measurements

In the absence of conductivity data for SnS , alternate analysis methods were sought. It was at this point in the project that all three of the crystal phases were found to be of insufficient purity for accurate Hall effect measurements. As such, a new batch of SnS crystals were synthesised using the same method as described in Chapter 2 previously, but this time replacing the 99.9 % purity tin with that of 99.9999 % purity, and subject to Hall effect analysis once again.

A Keithley 4200-SCS Semiconductor Characterization System was used with an Applied Magnetics Laboratory model # 4H2 Horizontal 2-Pole Adjustable Electromagnet in order to arrive at Hall effect measurements. The results were interpreted using a custom

LabView code developed by Christine Simmons and Rafael Jaramillo at the Massachusetts Institute of Technology, USA. This yielded an average conductivity of $19.84 \Omega^{-1} \text{ cm}^{-1}$, an average hole mobility of $95.35 \text{ cm}^2 \text{ V}^{-1} \text{ s}^{-1}$, and an average hole concentration of $1.287 \times 10^{18} \text{ cm}^{-3}$. The hole concentration agrees well with the hole concentrations of around 10^{18} reported by Albers *et al.*,²⁴⁶ but the conductivity is one of the highest reported for SnS to date.

It should be noted that the use of high-purity tin in the crystals, from which these Hall effect measurements were obtained, is not expected to reduce the presence of iodine from the CVT method that are observed in the GDMS analysis. As such, it is possible that the relatively large conductivity is due to extrinsic factors,*i.e.* iodine, in this case.

The crystals were also polished and subject to Hall effect measurements according to the orthorhombic system contact geometry of Montgomery,²⁴⁷ *i.e.* from two sample faces with edges along the principal crystal axes. This allowed for the calculation of anisotropic properties that yielded SnS conductivities of $8.929 \Omega^{-1} \text{ cm}^{-1}$ and $11.52 \Omega^{-1} \text{ cm}^{-1}$ in the *a* and *b* crystallographic directions respectively. As such, using the equation

$$\mu = \frac{\sigma}{N_p e} \quad (5.2)$$

where σ is conductivity, N_p is the concentration of holes and e is the elementary charge, the anisotropic hole mobilities are obtained as $68.5 \text{ cm}^2 \text{ V}^{-1} \text{ s}^{-1}$ and $88.4 \text{ cm}^2 \text{ V}^{-1} \text{ s}^{-1}$ along *a* and *b* respectively. This constitutes a mobility of around 29 % larger along the *b* axis compared to that of *a*, which is in agreement with the observation of a larger dielectric permittivity in the *b* direction for SnS, as presented in the previous chapter. It has also been noted in the literature that mobilities in the *c* direction of the crystal are around six times smaller than along either *a* or *b*, due to the weakly bound interactions between the covalent layers.²⁴⁶

The Hall analysis thus shows that SnS has favourable electrical properties for PV applications, but again, presents a high concentration of defects. As seen with the PR-TRMC analysis, this is not entirely favourable and could be the cause of the low voltage observed for SnS devices, while the obtained current remains fairly high.⁸⁴

5.2 Density functional theory analysis

5.2.1 Intrinsic defect formation for all phases

The previous sections showed that carrier concentration is one of the major factors determining electrical properties and is itself dependent on the presence of defects. Density functional theory allows for the explicit tendency of intrinsic defect formation to be calculated, which characterises both the degree and type of conductivity of a material.

The formation enthalpy of intrinsic point defects, tin and sulfur vacancies, was calculated using the supercell approach with the FHI-AIMS package.¹⁴¹ Lattice expansions of $(2 \times 4 \times 4)$, $(4 \times 4 \times 2)$ and $(2 \times 4 \times 1)$ were used for SnS, SnS_2 and Sn_2S_3 , respectively. k -point sampling of at least $2 \times 2 \times 2$ was performed, consistent with the length of the reciprocal lattice vectors. The defect formation energies were calculated with respect to the elemental standard states (Sn metal and solid S_8) and the concentrations were calculated following the law of mass action, under the assumption of thermal equilibrium at the growth temperature,²⁴⁸ according to the equation

$$N = n_i \exp^{-\left(\frac{\Delta H_f}{k_B T}\right)} \quad (5.3)$$

where N is the defect concentration, n_i is the number of defect species sites per unit volume in the crystal, ΔH_f is the defect formation enthalpy, k_B is the Boltzmann constant and T

Table 5.2: Point defect formation energies and concentrations calculated assuming sulfur rich growth conditions (atomic exchange with a reservoir of α -S) for the neutral defects at the respective synthesis temperatures. Multiple inequivalent sites for defect formation are distinguished with numerical subscripts. The type of the dominant defects is also indicated.

Phase	Spacegroup	Species	Formation energy (eV)	Concentration (cm^{-3})	Type
SnS	<i>Pnma</i>	V_{Sn}	0.68	2.28×10^{19}	acceptor
	<i>Pnma</i>	V_{S}	2.17	6.57×10^{12}	
SnS_2	<i>P-3m1</i>	V_{Sn}	3.16	2.54×10^{04}	donor
	<i>P-3m1</i>	V_{S}	1.80	2.21×10^{12}	
Sn_2S_3	<i>Pnma</i>	$V_{\text{Sn}(1)}$	1.17	7.08×10^{14}	acceptor
	<i>Pnma</i>	$V_{\text{Sn}(2)}$	2.68	2.04×10^{05}	
	<i>Pnma</i>	$V_{\text{S}(1)}$	1.67	7.72×10^{11}	donor
	<i>Pnma</i>	$V_{\text{S}(2)}$	1.38	5.13×10^{13}	
	<i>Pnma</i>	$V_{\text{S}(3)}$	1.77	1.63×10^{11}	

is temperature.²⁴⁹ Here, the temperature is chosen to be the synthesis temperature for the relative phase presented in Chapter 2, as the defects are assumed to be ‘locked in’ once cooled. These temperatures are higher than the anneal temperatures of typical SnS films and represent a possible overestimation of the magnitude of the concentrations, as can be seen by comparison with the values in Table 5.1.

In SnS, a fully ionised tin vacancy is associated with the generation of two positive charge carriers (i.e. holes) and one sulfur vacancy is associated with two negative charge carriers (i.e. electrons). These are expected to be the dominant native point defects, with the tin vacancy long assumed to be the origin of the *p*-type conductivity of SnS,²⁴⁶ while the sulfur vacancy is likely the origin of the *n*-type carriers in SnS_2 .

As shown in Table 5.2, the dependency of conductivity on defect stabilities is corroborated and, by extension, allows for the prediction of typical charge-carrier concentrations for each phase. The Sn vacancy has the lowest formation energy and highest concentration in SnS, which is consistent with that being the dominant acceptor defect. The predicted

high defect concentration agrees with the high Hall-effect conductivity measurements and the absence of PR-TRMC results presented already in this chapter.

For SnS_2 , the S vacancy dominates, which is consistent with its observed *n*-type behaviour from charge-balancing considerations. Overall, SnS_2 also shows a much lower tendency to form intrinsic defects, which agrees with the UV/vis spectra discussed in the previous chapter and with the PR-TRMC data presented in the previous section.

The Sn_2S_3 results elucidate the intermediate behaviour of a species containing both Sn(II) and Sn(IV) oxidation states. For SnS and SnS_2 the dominance of tin and sulfur vacancies, respectively, is unambiguous, which manifests as the observed longer carrier lifetimes and a second-order decay behaviour for the SnS_2 PR-TRMC analysis. Conversely in Sn_2S_3 , the formation energies of the two vacancy defects are close in energy, which indicates that carrier concentrations should be sensitive to the growth or annealing conditions, and, furthermore, that the major carrier type might be subject to change. This prediction also explains the first-order recombination behaviour shown in the previous section, as the high concentration of donor sites can effectively compensate the *n*-type carriers, and *vice versa*.

5.2.2 Charge carrier effective masses

The effective mass of a charge describes the ease with which a charge carrier can move through a material, with a heavier mass attributed to charges that move more slowly. It is related to charge mobility by

$$\mu = \frac{q}{m^*} \tau \quad (5.4)$$

where m^* is the effective mass, q is the elementary charge and τ is the carrier lifetime.

It was mentioned in the previous chapter that the dispersions of the band structure in-

dicate the strength of interaction in the same direction. BoltzTrap is a utility program that interpolates the electronic band structure and can derive pertinent semiconductor properties for a given system using Boltzmann transport theory.²⁵⁰ To date, this code and the underlying model has contributed to numerous projects, with over 300 citations at the time of writing. BoltzTrap was used in conjunction with the electronic-structure module of the pymatgen library in this project,²⁵¹ in order to calculate transport properties from the DFT band structure presented in Section 4.2.2. These codes assume an invariant band structure with respect to temperature, which was shown in the previous chapter (Section 4.2.3) to be a reasonable assumption.

In a simple parabolic band, the effective mass can be found by

$$m^* = \frac{\hbar}{\frac{\delta^2 E}{\delta k^2}} \quad (5.5)$$

i.e. the reduced Planck constant over the second derivative of the energy of the band, E , with respect to the wave vector k . For holes, the highest occupied valence band is used for E , whereas for electrons the lowest unoccupied conduction band is used. In most materials, however, certainly in anisotropic materials like the tin sulfides considered in this project, the effective mass is a tensor property, as bands can be non-parabolic and several parts of different bands can contribute to conductivity. Fortunately, these complexities can be accounted for within the semi-classical Boltzmann theory.²⁵²

The effective mass tensor, M , from a converged band structure calculation can be found via,²⁵³

$$M^{-1} = \frac{-\sum_i \int M^{-1}(i, k) f(E(i, k), E_F, T) \frac{dk}{4\pi^3}}{\sum_i \int f(E(i, k), E_F, T) \frac{dk}{4\pi^3}} \quad (5.6)$$

where E is the energy of the i th band, $f(E(i, k)$ is the Fermi-Dirac distribution and E_F is

the Fermi level, which is defined by,²⁵⁴

$$E_F = \frac{E_c + E_v}{2} + \frac{k_B T}{2} \log \frac{N_v}{N_c} \quad (5.7)$$

in which E_c is the energy of the conduction band, E_v is the energy of the valence band, and N_v and N_c are the density of states of the valence band and conduction band, respectively. E_F can be found from the carrier density, N , via the density of states from the band structure.

Using the value of the tin vacancy concentration for SnS, shown in Table 5.2, *i.e.* $2.28 \times 10^{19} \text{ cm}^{-3}$, with the SnS band structure discussed in the previous chapter, yields anisotropic values of the effective mass as shown in Table 5.3, from the BoltzTrap code. These results show, once again, a strong preference for charge transport in the b direction for holes, which is commensurate with earlier observations from this and the previous chapter.

The defect concentration used in this case, is somewhat larger than the carrier concentrations typically reported, likely due to the explicit assumption of complete ionisation of defects in this model and the relatively high synthesis temperatures in this case. As such, it is expected that the effective masses are somewhat underestimated compared to those in the literature. That said, experimentally determined effective masses for holes along the b crystallographic orientation are also of the order of $0.2 m_p^*$, from carrier reflectivity measurements.⁵⁰ These results are commensurate with earlier observations from this and the previous chapter.

5.2.3 Charge carrier mobilities

Mobility is the second component of conductivity, alongside carrier concentration. Now that the anisotropic effective masses have been obtained from the previous section, it is

Table 5.3: Charge carrier effective masses for SnS obtained from the semi-classical Boltzmann transport analysis of the DFT band structure.

Property	<i>a</i>	<i>b</i>	<i>c</i>
hole effective mass (kg)	9.869×10^{-31}	1.418×10^{-31}	1.340×10^{-30}
relative hole effective mass m_p^*	1.083	0.156	1.471

possible to arrive at an anisotropic value of free carrier mobility, entirely from *ab initio* methods. The procedure for arriving at such a value is a sum of charge scattering phenomena, according to the following equation

$$\frac{1}{\mu} = \frac{1}{\mu_i} + \frac{1}{\mu_l} + \frac{1}{\mu_g} + \frac{1}{\mu_n} \quad (5.8)$$

where μ_i is the ionised impurity scattering, μ_l is the lattice vibration scattering, μ_g is the grain boundary scattering and μ_n is the neutral impurity scattering.

The ionised impurity scattering is given by

$$\mu_i = \frac{3(\epsilon_v \epsilon_\infty)^2 h^3}{Z^2 m_p^{*2} e^3 F_i(\xi)} \quad (5.9)$$

where ϵ_v is the permittivity of free space, ϵ_∞ is the high frequency dielectric constant, h is Planck's constant, N_p is the carrier concentration, e is the elementary charge and Z is the charge of the impurity. The anisotropic values of the high frequency dielectric constant, or the value of the real dielectric constant at zero frequency, were shown in the previous chapter to be 12.70, 14.02 and 11.85 for the *a*, *b* and *c* directions.

F_i is given as

$$F_i(\xi) = \ln(1 + \xi) - \frac{\xi}{1 + \xi} \quad (5.10)$$

where ξ is

$$\xi = (3\pi^2)^{1/3} \frac{\epsilon_v \epsilon_\infty h^2 N_p^{1/3}}{m_p^* e^2} \quad (5.11)$$

ξ is anisotropic due to the directional dependence of the effective mass and the dielectric constant, ϵ_∞ , and is derived under the assumption of a degenerate semiconducting system *i.e.* one with high doping. This is called the Brooks-Herring-Dingle model,¹³⁶ and, for SnS, allows for the values μ_i along the a , b and c directions to be found as 1.88×10^{-3} , 2.36×10^{-2} and $1.37 \times 10^{-3} \text{ m}^2 \text{ V}^{-1} \text{ s}^{-1}$ respectively.

Increasing temperature means stronger lattice vibrations, deformation of the lattice and limitation of charge mobility by acoustic phonon scattering. J. Bardeen and W. Shockley calculated the mobility arising from lattice scattering (μ_l) in non-polar materials as:²⁵⁵

$$\mu_l = \frac{2\sqrt{2\pi}e\hbar^4 C_l}{3m_e^{5/2} E_d^2 (k_B T)^{3/2}} \quad (5.12)$$

where C_l is the longitudinal elastic constant, E_d is the deformation potential, \hbar is $h/2\pi$ and T is the absolute temperature of the semiconductor.

DFT (specifically the VASP implementation of structure optimisation) allows for the calculation of a materials elastic constants as a stiffness tensor $C_{ijk\dots}$ where ijk are 1,2...6 corresponding to a system of axes fixed in space. This is achieved by performing six finite distortions of the lattice and deriving the elastic constants from the strain-stress relationship,²⁵⁶ in a similar way to the lattice relaxation as discussed in Section 2.2.3.1. The symmetry of the SnS lattice structure reduces the number of independent elastic coefficients to nine, yielding the tensor

Table 5.4: Data used for the calculation of deformation potential of SnS, where the work function is equated to the ionisation potential.

Volume fraction	Volume (\AA^3)	Log volume	Work function (eV)
0.95	743.17	2.87	4.18
1.00	814.28	2.91	4.29
1.05	889.79	2.95	4.40

$$C_{ij} = \begin{bmatrix} 43.65 & 36.48 & 24.26 & 0 & 0 & 0 \\ & 91.00 & 20.78 & 0 & 0 & 0 \\ & & 69.44 & 0 & 0 & 0 \\ & & & 24.57 & 0 & 0 \\ & & & & 44.69 & 0 \\ & & & & & 25.24 \end{bmatrix}$$

in units of GPa.

The C_{ij} diagonal components are the elastic constants for C_{11} , C_{22} and C_{33} and the shear elastic constants for C_{44} , C_{55} and C_{66} . The off-diagonal constants are referred to as the mixed elastic constants, *e.g.* C_{31} , but are not of further use in this work.²⁵⁷ As such, the elastic constants are 43.65, 91.00 and 69.44 along the a , b and c directions.

The term E_d in Equation 5.12 is the deformation potential, which is the work function variance as a function of the natural log of cell volume. As logs are unitless, the overall unit of E_d is energy. For SnS, the relevant parameters for the calculation of this term are shown in Table 5.4, and yield the value of E_d of 2.72 eV.

With this data, the values μ_l for SnS at 298 K can be obtained as 2.97×10^{-2} , 7.92 and $2.20 \times 10^{-2} \text{ m}^2 \text{ V}^{-1} \text{ s}^{-1}$ along a , b and c .

Returning to Equation 5.8, neutral impurities also scatter charges according to the equation

$$\mu_n = \frac{m_p^* e^3}{20\epsilon_\infty \epsilon_v \hbar^3 N_N} \quad (5.13)$$

where N_N is the density of neutral defects. Here, N_N is approximated as the concentration of Schottky defects, which consist of a cation and anion vacancy within the bulk crystal, usually having migrated into the bulk from the crystal surface. The equivalent nature of the defect pairs the system is overall charge neutral, but will have a non-zero defect concentration above 0 K.

As before the defect concentration can be found through an Arrhenius equation (Equation 5.3, this time with a factor of $2k_B T$ to account for the dual nature of the defects and, again, is calculated at the same temperature as the crystal synthesis. This approach yields an N_N of $4.89 \times 10^{11} \text{ cm}^{-3}$.

As such, it can be found that for SnS at 298 K, the values of μ_n are 3.15×10^6 , 4.10×10^5 and $4.58^6 \text{ m}^2 \text{ V}^{-1} \text{ s}^{-1}$ along a , b and c , respectively.

For completion, the corresponding equation for grain boundary scattering μ_g is included as

$$\mu_g = \left(\frac{L^2 e^2}{2\pi m_p^* k_B T} \right)^{1/2} \exp \left(-\frac{\psi_b}{k_B T} \right) \quad (5.14)$$

where L is the grain size and ψ_b is the grain boundary energy barrier. It can be seen that accounting for all possible grain boundary combinations and their barrier heights is a non-trivial task with electronic structure methods and that the size of the grain boundaries would be system dependent. As bulk calculations correspond to infinite perfect solids, the grain boundary scattering mechanism is neglected in this work.

Mobilities can now be found from Equation 5.8, which gives values of 1.77×10^{-3} , 2.36×10^{-2} and $1.29 \times 10^{-3} \text{ m}^2 \text{ V}^{-1} \text{ s}^{-1}$ in a , b and c directions respectively.

This yields an isotropic mobility of $236.7 \text{ cm}^2 \text{ V}^{-1} \text{ s}^{-1}$, compared to the experimentally observed Hall mobility value of $95.35 \text{ cm}^2 \text{ V}^{-1} \text{ s}^{-1}$ for SnS single crystals. The theoretically obtained values are unsurprisingly high when compared to those obtained from Hall measurement considering the high temperatures implicit in these calculated values. What does remain surprising is the degree to which anisotropy is overestimated using this method. Comparing again with the Hall-effect mobility measurement, the value of mobility in the *b* direction was found to be 29 % larger than that along the *a* vector, whereas here, the mobility in the *b* direction is predicted to be more than 13 times that along *a*.

The Python code written to produce anisotropic values for mobility, as discussed in this section for SnS, can be found in the Appendix, Section A.5.

5.2.4 Modelled conductivity for SnS

Given the values of mobility derived in the previous section, it is possible to arrive at anisotropic values of conductivity as a function of temperature, using the Boltzmann transport equations implemented in the BoltzTrap code.

Given Equation 5.4, anisotropic values of τ can be found to be 1.08×10^{-14} , 2.09×10^{-14} and $1.091 \times 10^{-14} \text{ s}^{-1}$ along *a*, *b* and *c* respectively, which are of the same order as those observed for solid elements at 273 K.²⁵²

The Boltzmann transport equations, as solved by the BoltzTrap code, report conductivity per relaxation time as a function of temperature and chemical potential

$$\frac{\sigma(T;E_F)}{\tau} = \frac{1}{\Omega} \int \sigma(E) \left[-\frac{\delta f_{\mu_{cp}}(T;E)}{\delta E} \right] \delta E \quad (5.15)$$

where Ω is the volume of the unit cell. Now that relaxation time has been found, it is possible to find the conductivity from the same level of theory.

These results, shown in Figure 5-5, show the strong electrical anisotropy, with the

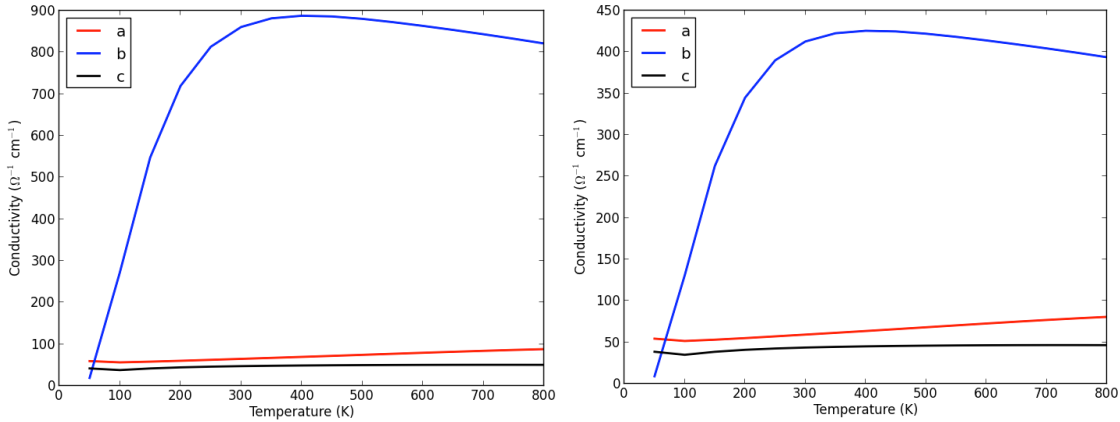


Figure 5-5: The anisotropic conductivity calculated for SnS using the values of τ calculated from the previous section (left) and using the recommended isotropic τ value of 1×10^{-14} (right).

higher degree of conductivity along the b axis, that has been observed repeatedly throughout the previous chapters. However, when compared with the experimentally observed conductivities, of up to $70 \Omega^{-1} \text{ cm}^{-1}$, the values are much too high. Even if the value of τ is held fixed at 1×10^{-14} for each of the three axes, effectively decoupling the results of this section from those of the previous section, the values are still much too large (also shown in Figure 5-5).

While it has been noted that to obtain reliable results using this method requires a significantly larger sampling of k -points than for standard properties,²⁵³ it can be seen from Figure 5-6 that for the b axis at least, the k -point mesh appears to converge to an unreasonably large value for the 300 K conductivity, relatively quickly. The values along the a vector appear to be approaching those of the b direction with increasing k -grid density; however, the conductivity in the c and b vector do not appear to be varying as much and are still a factor of nine apart. This factor is reported to be six in experiment,²⁴⁶ an observation that indicates that perhaps the qualitative anisotropy, at least, can be reproduced by the current level of treatment at a sufficiently high k -grid resolution. It should be noted, however,

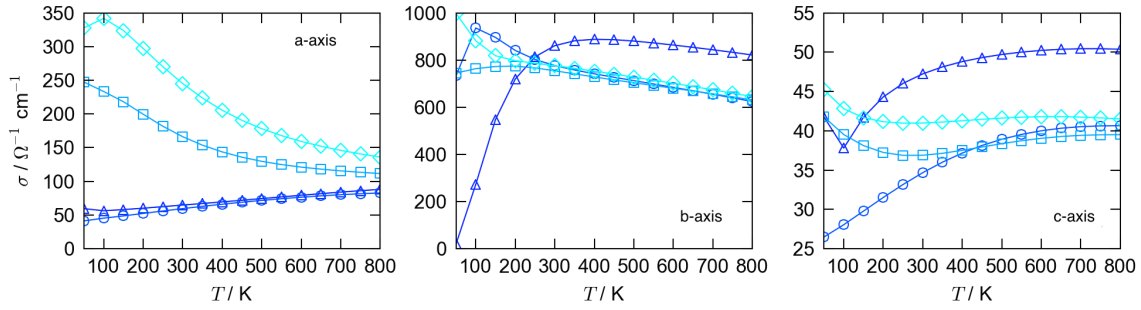


Figure 5-6: k -grid convergence for the conductivity of SnS from the BoltzTrap code, from blue (a resolution of 486 points), to cyan (a resolution of 13,122 points).

that the reciprocal sampling resolution of over 13,000 k -points, used here to produce both Figure 5-5 and Figure 5-6, is orders of magnitude larger than the recommended sampling by Moreno *et al.*,²⁵⁸ that was used in order to arrive at the accurate band structure and concomitant dielectric properties discussed in the previous chapter.

5.2.5 Results comparison & discussion

Once again, this chapter has shown how SnS can appear ideal as a photovoltaic material at first glance. The large conductivities presented, that are necessary for high efficiency PV devices, and the strong preference for tin vacancy formation, that defines a robust intrinsic *p*-type nature, certainly would be considered attractive. The PR-TRMC results obtained for SnS, however, could provide an explanation as to why high-efficiency PV devices with SnS as an absorber layer have not yet been realised. Usually, the reported short-circuit current is acceptable, yet the open-circuit voltage is too low, typically lower than 200 mV. It is possible that, due to a high background conductivity, the splitting of the quasi Fermi level under illumination is suppressed. Indeed, the reduction of dark conductivity of a PV cell has been shown to increase obtained voltage in the literature.²⁵⁹

The sulfur vacancy, in SnS, was thought to potentially act as an electron trap, but it

has been shown that the sulfur vacancies themselves do not compensate for the *p*-type contribution of tin vacancies, due to defect levels deep in the band gap.²¹¹ In this way, it is possible that the intrinsic defects of SnS do not mutually compensate, and is potentially the origin of the suppressed quasi-Fermi level splitting presented for the single crystal SnS in this work, and the low voltages obtained in devices.⁸⁴ That said, it is possible that this observation is unique to this study as the relatively high number of iodine defects present in the crystals (see Section 3.1.2) are considered an *n*-type, extrinsic dopant, given the lower valence of sulfur. As such, a high concentration of *n*-type iodine, and *p*-type tin vacancy defects could be the origin of the pinned Fermi levels. Further work, using an alternate single crystal synthesis technique would be required to fully explore this possibility.

The ease of formation of intrinsic defects in SnS is also elucidated explicitly with the use of DFT. Even relative to the alternate tin sulfide phases and the comparable synthesis conditions, SnS shows a predicted concentration of intrinsic defects, five orders of magnitude greater than the next highest predicted defect concentration (tin vacancy in Sn_2S_3). It is possible that such a tendency to form defects relates to the instability of single crystals seen throughout this project, while the sesqui- and disulfide phases have shown to be more resistant with respect to defect formation and crystallite instability.

The PR-TRMC results for SnS_2 show an excellent electron drift length that is considered desirable for an application such as photovoltaics, however, the charge lifetimes corroborate observations of a 2-dimensional transport system. Such systems are predicted to have many applications in nano-scale electronic devices, but would be problematic for charge extraction in PV configurations, unless a method of deposition that allowed for crystal growth of bonded planes perpendicular to a device contact were identified.

Finally, Sn_2S_3 does not appear to suffer from the same problem as SnS (*i.e.* no large density of carriers and concomitant dark conductivity), yet has a high carrier mobility, larger than amorphous silicon, for example.²⁶⁰ It is possible that a thin-film of stoichiomet-

ric Sn_2S_3 , extrinsically doped in order to be *p*- or *n*-type could be a superior photo-active material to tin monosulfide.

The transport properties derived from the DFT ground state electronic structure serve to illustrate the degree to which theoretical results can be used to assess materials properties. Similar levels of theory have recently been successfully applied to alternate photovoltaic materials with the goal of determining similar parameters.^{253,261} Unfortunately, it appears that the theoretical methods used in this thesis to arrive at values of mobility and conductivity significantly overestimate the electronic anisotropy and charge transport properties of SnS. While the anisotropy is certainly present in bulk SnS, it is the conclusion of this work that the methods detailed are more suited to comparative or screening studies, as previously performed by others,²⁵³ rather than quantitative prediction. It is likely that the effective mass tensor is the most accurate quantity pertaining to transport properties that can be derived purely from *ab initio* methods at this time, being directly related to band structure, which has been shown in this work (and others) to agree closely with experiment.

It should be noted that the successful photovoltaic material CZTS has also been shown to be anisotropic with respect to charge transport,²⁶² and so this is likely not a major efficiency loss mechanism for SnS in PV devices.

Chapter 6

Conclusion

This project has explored the multiphasic tin sulfide system with state of the art density functional theory and bulk materials analysis of single crystals. It has been the aim of this report to identify potential factors that might limit photovoltaic performance of the earth abundant tin monosulfide.

In the Introduction it was shown that a surprising number of potential issues associated with tin monosulfide are also associated with copper-zinc-tin-sulfide, a material that is able to achieve certified efficiencies of more than twice those of SnS.⁵³ Several of these expected ‘minor’ issues are reported for SnS in this project; however, several interesting and novel insights into the tin sulfide chemical phase space, that are unique to this system, have also been made.

First of all, it has been argued in this report that zincblende tin monosulfide does not now, nor ever has, existed. Instead, it is proposed that the rocksalt phase of SnS has been mis-assigned as zincblende, which represents a significant reduction in the complexity of the phase space of SnS, from four known phases to three. Also of significance, is that rocksalt tin monosulfide is known to form under epitaxial strain and could be present in

strained thin-film heterojunctions, *i.e.* device configurations. Such a species present at an interface could evade detection by composition analysis techniques such as depth profiling XPS,¹⁷⁵ and be concealed by orthorhombic SnS in surface sensitive characterisation techniques, such as grazing incidence X-ray diffraction, used by countless reports in the literature.^{83,220,263} Worryingly for PV applications, the rocksalt conformation tin monosulfide is predicted to exhibit the rare phenomenon of topological insulation,¹⁷⁷ which would be detrimental to device performance if such a state were present at interfaces.

Secondly, the presence of phase impurities has also shown to be likely problematic for tin sulfide PV devices, both by single crystal and DFT analysis. It is expected that Sn_2S_3 , which has been shown to be a persistent, stable phase throughout this report, would act as a recombination centre if it were locally present in an SnS sample. Worse still, SnS_2 is predicted to act as a blocking layer for charge extraction, which is disconcerting, given its observed presence at SnS heterojunction interfaces in the literature.¹⁷⁵ Whilst CZTS is similarly expected to suffer from the presence of impurity phases, the successful CdTe system has no known competing phases.

Thirdly, tin monosulfide exhibits a work function that is around 1 eV lower in magnitude than the current generation of successful photovoltaic materials, including CZTS. As a result, it is possible to conclude that the architectures of device used for SnS to date are not optimal, as they are designed to work with materials with band edge states of higher binding energy. Similarly, the low work function of SnS means that the presence of a metal disulfide interlayer, which are shown to likely form at contact interfaces in devices, will block efficient charge extraction, unlike for higher work function materials. While no such device degradation is observed directly in this project, the prediction for this occurrence agrees with the facile loss of sulfur for SnS observed repeatedly in this project. These predictions are commensurate with the observed low voltage output from SnS devices that still present a relatively high current and internal quantum efficiency.^{81,84} It is

worth stating that the work function of a material, if properly matched, has no affect on device performance, only the band gap represents an intrinsic limitation. As such, this prediction does not preclude the use of SnS as a photovoltaic material.

The observation of non-commensurate device contacts being used to trial potential photovoltaic materials also raises a broader concern. It would seem likely that many more photoactive materials might be able to contribute to the field of photovoltaics, were the device components more suitably tailored to the physical properties of the photon absorber layer. In this project, DFT has been shown to be a powerful predictive tool that can guide the construction of novel device configurations; not only is it possible to account for contact reactions inside a device, but the natural band alignments and likely electronic effects can also be predicted.

This project has also been unique in its direct comparison between theory and experiment, with results that are expected to be of greater use to the wider community. First of all, the thermodynamic reactions allow for an explicit understanding of system behaviour. For the SnS single crystals, the reaction enthalpies studied for the carrier species, iodine, allowed for an explicit prediction as to the optimisation of the chemical vapour transport method, for these and related systems in the future. Similarly, an optimal back contact for SnS was identified from the judicious selection of just four earth-abundant metals, that has yet to be implemented in PV devices. It is expected that broader searches could benefit the wider field at large.

Subsequently it was shown that an incredible level of agreement could be found between electronic structure calculations and experiment, even for an anisotropic system such as SnS. As a result, it is expected that properties closely related to the band structure, such as charge carrier effective mass, for example, are sufficiently accurate for quantitative analysis and comparative screening studies.²⁵³ In this case, such analysis allowed for the identification of an optimal crystallographic orientation for SnS thin films, that had not

been targeted prior to this work.

The exploration of the transport properties of the tin sulfides present in Chapter 5 (*i.e.* mobility and conductivity), however, appear to be pushing the limits of what time-independent electronic structure theory can realistically be expected to achieve. It is possible to see from Chapter 2, the great effort that has gone into reducing the complexity associated with treating solids at a quantum mechanical level. This, naturally results in the treatment of a perfect bulk solid. Thus, it is probably unsurprising that quantitatively predicting a physical property that depends on defects and imperfections is not yet as well implemented as some of the other theoretical methods. That is not to say that DFT is powerless in this regard, indeed the defect concentrations predicted in Section 5.2.1 were successful in elucidating the experimentally observed behaviour of the tin sulfide phases, both in this report and in the literature.

A limitation of this project is the quality of the single crystals when it came to defect analysis. Certainly the lack of observed quasi-Fermi level splitting with PR-TRMC analysis represents a potential loss mechanism for PV. However, with the known iodine impurities in the crystal it is impossible to discern whether the hole and electron states were split by tin and sulfur intrinsic vacancies, or tin vacancies and iodine dopants, respectively.

Finally, it should not be forgotten that SnS_2 and Sn_2S_3 are interesting semiconducting materials in their own right, despite the fact that their consideration has been secondary to SnS in this thesis. Indeed, the TGA for these single crystals and observations of stability with respect to oxygen exposure, would indicate that both of these phases are more stable than SnS, with electronic configurations more directly applicable to certain uses. For example, the deep energy levels and wide band gap of SnS_2 have lead to reports of a photon conversion efficiency of over 38 % for water splitting with this material.²⁶⁴ SnS_2 also belongs to the class of 2-dimensional semiconductors that have received enormous

attention for nano-scale electronics recently. It is hoped that the placement of the energy levels and band gaps of tin disulfide in this report might be of use for these applications, outside of photovoltaics.

Likewise, this report represents the first time an in-depth analysis as to the properties of tin sesquisulfide has been performed. The potential suitability of Sn_2S_3 as a photovoltaic material presents itself throughout this report, with properties that are arguably more desirable than tin monosulfide found in each of the three research chapters of this thesis. For example, the stability of the material seems greater than that of SnS, the work function and band gap lie more closely in energy with those of CZTS than do those of SnS, and the PR-TRMC analysis indicates more suitable transport properties than SnS as well.

This project provides a platform for further study of all earth abundant photovoltaic materials, not just SnS. It is hoped that, given the results of this project, a more holistic approach will be employed in the future implementation of potential photoactive materials, tailoring the entire device to suit the properties of the absorber layer.

Chapter 7

Future work

The results presented in this thesis provide much opportunity for the further exploration of the phases of tin monosulfide and the field of sustainable PV.

Firstly, as was discussed in Chapter 3, the CVT synthesis employed in this project was shown to lead to a relatively high concentration of iodine impurities in the SnS sample at least, but, most likely, all three phases. However, it is proposed that CVT with high purity precursors, cleaned and then polished could provide the crystal seed for use in a subsequent Bridgman-Stockbarger growth method, which does not require a carrier agent. In this way, large amounts of high-purity single crystals could be obtained. Keeping these under vacuum for as long as possible should allow for more accurate derivation of electronic properties using the characterisation techniques used in this report. UPS and IPES for example, that are sensitive to surface contaminants, could even receive crystals that had no prior exposure to oxygen or adventitious carbon, as they are synthesised, transported and analysed under vacuum.

Secondly, it was shown in this report that SnS appears to be surprisingly unstable, even when compared to the alternate tin sulfide phases. Chapter 3 detailed the observation of

sulfur loss at room temperature and atmospheric conditions, while Chapter 4 showed that heating under vacuum showed an accelerated loss of sulfur leading to surface metallisation. An example experiment to further investigate the observations detailed in this report include the sealing of SnS single crystals in an inert atmosphere, for a prolonged period of time. In this way, the sample is still subject to an ambient pressure and temperature, yet the reactive component of an oxygen atmosphere is removed. If SnS were to degrade somehow under these conditions, it is unlikely that it would ever be able to find use in a solid state device. In the same way that Cu₂S was disavowed after almost all devices were found to deteriorate over time due to copper diffusion that is difficult to control,⁵¹ it is possible that this could be the case for sulfur in SnS.

Similarly, the strong driving force behind the formation of a high concentration of defects was presented in Chapter 5. With a hypothetical high purity crystal from Bridgman-Stockbarger synthesis, the intrinsic defects could be observed explicitly, by the use of positron annihilation spectroscopy. This technique has been shown to be especially useful in the observation of lattice vacancy defects in semiconductor materials,²⁶⁵ unlike, for example the GDMS technique used in this project. In this way the optimal region of *p*-type conductivity of SnS could be identified as a function of single crystal synthesis conditions, and the large dark conductivity present in these crystals, suppressed.

Again, following on from the successful synthesis of high purity material, it would be possible to go one step further. Lambros *et al.* reported the successful exfoliation of single crystal SnS with adhesive tape, allowing for the isolation of thin-films, from a high purity, uniform precursor.¹²⁸ Such a possibility is commensurate with the continued observation of weak interlayer interaction for the SnS presented in this thesis. Care must be taken with respect to oxygen exposure in this regard, especially for thin-films, however this would allow for the presence of off-stoichiometric phases to be investigated using 2-dimensional mapping techniques, such as Raman spectroscopy, for example.

It is predicted in this work that an MoS_2 interlayer exists in SnS junctions with molybdenum. It is also predicted that increased performance could be obtained were tin used as a device contact, *and* were SnS orientated in the (010) direction. The degree to which these factors could increase performance remain to be seen; ultimately, the predictions made in this report can only be verified with device fabrication and suitable characterisation. For example, the power and sensitivity of depth profile X-ray photoelectron spectroscopy has been demonstrated in the literature,¹⁷⁵ were this performed on an SnS - molybdenum heterojunction, the presence of the disulfide could be verified.

Finally, SnS_2 and Sn_2S_3 ought to be further investigated as photo-active materials. Once again a precursor crystal synthesised from CVT, could seed much larger mass of high purity crystalline phases. While SnS_2 is already gaining interest as a water splitting photocatalyst, Sn_2S_3 has received little attention to date. Both the theory and experiment in this report predict that Sn_2S_3 could be a suitable photon absorbing material and that it would form a *p-n* junction with SnS_2 . These results indicate that a tin film with a depth-graded sulfur content could create strong rectifying behaviour in a device. The potential existence of Sn_3S_4 and Sn_4S_5 could also be investigated using materials simulation, which has been shown in this project to be an instructive tool in the analysis of the tin-sulfur stability phase space.

Bibliography

- [1] E. Wolf and I. Fung, *Climate Change Evidence and Causes*, the Royal Society & the US National Academy of Sciences report, 2014.
- [2] S. Shafiee and E. Topal, *Energy Policy*, 2009, **37**, 181–189.
- [3] S. Sorrell, J. Speirs, R. Bentley, A. Brandt and R. Miller, *Global Oil Depletion: an assessment of the evidence for a near-term peak in global oil production*, UK Energy Research Centre report, 2009.
- [4] R. Priddle, *World Energy Outlook*, International Energy Agency report, 2012.
- [5] C. Philibert, *Solar Energy Perspectives*, International Energy Agency report, 2011.
- [6] B. Dudley, *BP Statistical Review of World Energy*, British Petroleum report, 2012.
- [7] K. G. Kerry Gilpin, John Lushetsky, *Enlisting the Sun: Powering the U.S. Military with Solar Energy*, Solar Energy Industries Association report, 2013.
- [8] H. Wirth, *Recent Facts about Photovoltaics in Germany*, Fraunhofer Institut fur Solare Energiesysteme report, 2014.
- [9] Z. Dobrotkova, A. Goodrich, M. Mackay, C. Philibert, G. Simbolotti and X. Wenhua, *Renewable Energy Cost Analysis - Solar Photovoltaics*, International Renewable Energy Agency report, 2012.
- [10] J. L. Monteith and C. J. Moss, *Phil. Trans. R. Soc. B*, 1977, **281**, 277–294.
- [11] X. Zhu, S. Long and D. Ort, *Curr. Opin. Biotechnol.*, 2008, **19**, 153–159.
- [12] J. P. Denruyter and L. Mulder, *Solar PV Atlas: Solar Power in Harmony with Nature*, World Wildlife Fund report, 2013.

- [13] D. Perez, V. Cervantes, M. J. Baez and F. T. Dominguez, *PV Grid Parity Monitor*, Eclarion report, 2013.
- [14] C. Breyer and A. Gerlach, Proceedings of the 26th European Photovoltaic Solar Energy Conference, Hamburg, 2011.
- [15] L. M. Peter, *Phil. Trans. R. Soc. A*, 2011, **369**, 1840–1856.
- [16] W. Shockley and H. J. Queisser, *J. Appl. Phys.*, 1961, **32**, 510.
- [17] V. Quaschning, *The Sun as an Energy Resource*, Renewable Energy World report, 2003.
- [18] S. H. Lee, D. H. Kim, J. H. Kim, G. S. Lee and J. G. Park, *J Phys. Chem. C*, 2009, **113**, 21915–21920.
- [19] K. Mertens, *Photovoltaics: Fundamentals, Technology and Practice*, Wiley, 2013.
- [20] C. E. Fritts, *Am. J. Sci.*, 1883, **26**, 465–472.
- [21] D. M. Chapin, C. S. Fuller and G. L. Pearson, *J. Appl. Phys.*, 1954, **25**, 676–677.
- [22] M. A. Green, K. Emery, Y. Hishikawa, W. Warta and E. D. Dunlop, *Prog. Photovoltaics Res. Appl.*, 2014, **22**, 1–9.
- [23] M. A. Green, *Clean Electricity from Photovoltaics*, World Scientific Publishing Company, 2001.
- [24] M. Taguchi, A. Yano, S. Tohoda, K. Matsuyama, Y. Nakamura, T. Nishiwaki, K. Fujita and E. Maruyama, *IEEE J. Photovolt.*, 2014, **4**, 96–99.
- [25] C. R. A. Catlow, Z. X. Guo, M. Miskufova, S. A. Shevlin, A. G. H. Smith, A. A. Sokol, A. Walsh, D. J. Wilson and S. M. Woodley, *Phil. Trans. R. Soc. A*, 2010, **368**, 3379–3456.
- [26] T. Markvart, *Prog. Quant. Electron.*, 2000, **24**, 107–186.
- [27] V. Fthenakis, *Renew. Sust. Energ. Rev.*, 2009, **13**, 2746–2750.
- [28] S. Benagli, D. Borrello, E. Vallat, J. Meier, U. Kroll, J. Htzel, J. Bailat, J. Steinhauser, M. Marmelo, G. Monteduro and L. Castens, EU PVSEC Proceedings, 2009, pp. 2293–2298.
- [29] S. S and R. U, *Wide-gap Chalcopyrites*, Springer, 2006.

- [30] E. Alsema, M. de Wild-Scholten and V. Fthenakis, European Photovoltaic Solar Energy Conference, Dresden, Germany, 2006.
- [31] M. M. de Wild-Scholten, *Sol. Energ. Mat. Sol. Cells*, 2013, **119**, 296–305.
- [32] R. R. King, D. Bhusari, D. Larrabee, X. Q. Liu, E. Rehder, K. Edmondson, H. Cotal, R. K. Jones, J. H. Ermer, C. M. Fetzer, D. C. Law and N. H. Karam, *Prog. Photovoltaics Res. Appl.*, 2012, **20**, 801–815.
- [33] D. Swinbanks, O. Graydon and M. Konagai, 2010 Nature Photonics Technology Conference Future Perspectives on Photovoltaics, Tokyo, Japan, 2010.
- [34] R. W. G. Wyckoff, *Am. J. Sci.*, 1928, **16**, 349–359.
- [35] A. Kojima, K. Teshima, Y. Shirai and T. Miyasaka, *J. Am. Chem. Soc.*, 2009, **131**, 6050–6051.
- [36] H. Zhou, Q. Chen, G. Li, S. Luo, T. B. Song, H. S. Duan, Z. Hong, J. You, Y. Liu and Y. Yang, *Science*, 2014, **345**, 542–546.
- [37] J. M. Frost, K. T. Butler, F. Brivio, C. H. Hendon, M. van Schilfgaarde and A. Walsh, *Nano Lett.*, 2014, **14**, 2584–2590.
- [38] A. Nattestad, A. J. Mozer, M. K. R. Fischer, Y. B. Cheng, A. Mishra, P. Bauerle and U. Bach, *Nat. Mater.*, 2010, **9**, 1476–1122.
- [39] G. Boschloo and A. Hagfeldt, *Acc. Chem. Res.*, 2009, **42**, 1819–1826.
- [40] D. Li, H. Li, Y. Luo, K. Li, Q. Meng, M. Armand and L. Chen, *Adv. Funct. Mater.*, 2010, **20**, 3358–3365.
- [41] Q. Chen, H. Zhou, Z. Hong, S. Luo, H. S. Duan, H. H. Wang, Y. Liu, G. Li and Y. Yang, *J. Am. Chem. Soc.*, 2014, **136**, 622–625.
- [42] Z. Ning, O. Voznyy, J. Pan, S. Hoogland, V. Adinolfi, J. Xu, M. Li, A. R. Kirmani, J. P. Sun, J. Minor, K. W. Kemp, H. Dong, L. Rollny, A. Labelle, G. Carey, B. Sutherland, I. Hill, A. Amassian, H. Liu, J. Tang, O. M. Bakr and E. H. Sargent, *Nat. Mater.*, 2014, **13**, 822–828.
- [43] J. Wallentin, N. Anttu, D. Asoli, M. Huffman, I. Aberg, M. H. Magnusson, G. Siefer, P. Fuss-Kailuweit, F. Dimroth, B. Witzigmann, H. Q. Xu, L. Samuelson, K. Deppert and M. T. Borgström, *Science*, 2013, **339**, 1057–1060.

- [44] R. Dahal, B. Pantha, J. Li, J. Y. Lin and H. X. Jiang, *Appl. Phys. Lett.*, 2009, **94**, 063505.
- [45] A. Ennaoui and H. Tributsch, *Solar Cells*, 1984, **13**, 197–200.
- [46] S. Seefeld, M. Limpinsel, Y. Liu, N. Farhi, A. Weber, Y. Zhang, N. Berry, Y. J. Kwon, C. L. Perkins, J. C. Hemminger, R. Wu and M. Law, *J. Am. Chem. Soc.*, 2013, **135**, 4412–4424.
- [47] L. Yu, S. Lany, R. Kykyneshi, V. Jieratum, R. Ravichandran, B. Pelatt, E. Altschul, H. A. S. Platt, J. F. Wager, D. A. Keszler and A. Zunger, *Adv. Energy Mater.*, 2011, **1**, 748–753.
- [48] G. Liu, T. Schulmeyer, J. Brotz, A. Klein and W. Jaegermann, *Thin Solid Films*, 2003, **431–432**, 477–482.
- [49] S. C. Riha, S. Jin, S. V. Baryshev, E. Thimsen, G. P. Wiederrecht and A. B. F. Martinson, *ACS Appl. Mater. Inter.*, 2013, **5**, 10302–10309.
- [50] O. Madelung, *Semiconductors: Data Handbook*, Springer, 3rd edn, 2004.
- [51] R. Saraf, *IOSR-JEEE*, 2012, **2**, 47.
- [52] K. Ito and T. Nakazawa, *Jpn. J. Appl. Phys.*, 1988, **27**, 2094.
- [53] B. Shin, O. Gunawan, Y. Zhu, N. A. Bojarczuk, S. J. Chey and S. Guha, *Prog. Photovoltaics Res. Appl.*, 2013, **21**, 72–76.
- [54] W. Wang, M. T. Winkler, O. Gunawan, T. Gokmen, T. K. Todorov, Y. Zhu and D. B. Mitzi, *Adv. Energy Mater.*, 2014, **4**, –.
- [55] S. Chen, X. G. Gong, A. Walsh and S. H. Wei, *Appl. Phys. Lett.*, 2010, **96**, 021902.
- [56] S. Chen, J. H. Yang, X. G. Gong, A. Walsh and S. H. Wei, *Phys. Rev. B*, 2010, **81**, 245204.
- [57] Y. T. Zhai, S. Chen, J. H. Yang, H. J. Xiang, X. G. Gong, A. Walsh, J. Kang and S. H. Wei, *Phys. Rev. B*, 2011, **84**, 075213.
- [58] J. J. Scragg, T. Kubart, J. T. Wtjen, T. Ericson, M. K. Linnarsson and C. Platzer-Bjrkman, *Chem. Mater.*, 2013, **25**, 3162–3171.
- [59] M. Parenteau and C. Carbone, *Phys. Rev. B*, 1990, **41**, 5227.

- [60] J. M. Chamberlain and M. Merdan, *J. Phys. C: Solid State Phys.*, 1977, **10**, L571.
- [61] K. R. Reddy, N. K. Reddy and R. Miles, *Sol. Energ. Mat. Sol. C.*, 2006, **90**, 3041–3046.
- [62] C. S. Ferekides, U. Balasubramanian, R. Mamazza, V. Viswanathan, H. Zhao and D. L. Morel, *Sol. Energy*, 2004, **77**, 823–830.
- [63] Z. Xu and Y. Chen, *Semicond. Sci. Tech.*, 2012, **27**, 035007.
- [64] W. Albers, C. Haas, H. J. Vink and J. D. Wasscher, *J. Appl. Phys.*, 1961, **32**, 2220.
- [65] K. R. Reddy, P. P. Reddy, P. Datta and R. Miles, *Thin Solid Films*, 2002, **403?404**, 116–119.
- [66] M. B. Prince, *J. Appl. Phys.*, 1955, **26**, 534–540.
- [67] J. J. Loferski, *J. Appl. Phys.*, 1956, **27**, 777–784.
- [68] G. B. Haxel, J. B. Hedrick and G. J. Orris, *Rare Earth Elements Critical Resources for High Technology*, United states geological survey fact sheet, 2002.
- [69] D. Bauer, D. Diamond, J. Li, M. McKittrick, D. Sandalow and P. Telleen, *Critical Materials Strategy*, U.s. department of energy technical report, 2011.
- [70] M. W. Gaultois, T. D. Sparks, C. K. H. Borg, R. Seshadri, W. D. Bonificio and D. R. Clarke, *Chem. Mater.*, 2013, **25**, 2911–2920.
- [71] D. Anderson, *New Theory of the Earth*, Cambridge University Press, 2007.
- [72] K. C. Seto, B. Guneralp and L. R. Hutyra, *PNAS*, 2012, 16083–16088.
- [73] C. Anderson, *Tin Mineral Commodity Survey*, United states geological survey technical report, 2014.
- [74] V. M. Fthenakis, *Energy Policy*, 2000, **28**, 1051–1058.
- [75] C. Wadia, A. P. Alivisatos and D. M. Kammen, *Energy Environ. Sci.*, 2009, **43**, 2072–2077.
- [76] R. Moskalyk, *Miner. Eng.*, 2003, **16**, 921–929.
- [77] A. Alfantazi and R. Moskalyk, *Miner. Eng.*, 2003, **16**, 687–694.

- [78] M. McManus, *Appl. Energ.*, 2012, **93**, 288–295.
- [79] H. Noguchi, A. Setiyadi, H. Tanamura, T. Nagatomo and O. Omoto, *Sol. Energ. Mater. Sol. Cells*, 1994, **35**, 325–331.
- [80] H. Dittrich, D. J. Vaughan, R. A. D. Patrick, S. Graeser, M. Lux-Steiner, R. Kunst and D. Lincot, 13th European PV Solar Energy Conf., Nice, France, 2006.
- [81] N. Koteswara Reddy and K. Ramakrishna Reddy, Photovoltaic Specialists Conference, 1997, Conference Record of the Twenty-Sixth IEEE, 1997, pp. 515–518.
- [82] P. Sinsermsuksakul, L. Sun, S. W. Lee, H. H. Park, S. B. Kim, C. Yang and R. G. Gordon, *Adv. Energy Mater.*, 2014, 1400496.
- [83] O. E. Ogah, G. Zoppi, I. Forbes and R. Miles, *Thin Solid Films*, 2009, **517**, 2485–2488.
- [84] V. Steinmann, R. Jaramillo, K. Hartman, R. Chakraborty, R. E. Brandt, J. R. Poindexter, Y. S. Lee, L. Sun, A. Polizzotti, H. H. Park, R. G. Gordon and T. Buonassisi, *Adv. Mater.*, 2014, –.
- [85] Y. Wu, C. Wadia, W. Ma, B. Sadtler and A. P. Alivisatos, *Nano Lett.*, 2008, **8**, 2551–2555.
- [86] A. T. Kana, T. G. Hibbert, M. F. Mahon, K. C. Molloy, I. P. Parkin and L. S. Price, *Polyhedron*, 2001, **20**, 2989–2995.
- [87] P. K. Nair, M. T. S. Nair, V. M. Garcia, O. L. Arenas, Y. Pena, A. Castillo, I. T. Ayala, O. Gomezdaza, A. Sanchez, J. Campos, H. Hu, R. Suarez and M. E. Rincon, *Sol. Energ. Mat. Sol. C.*, 1998, **52**, 313–344.
- [88] P. Sinsermsuksakul, J. Heo, W. Noh, A. S. Hock and R. G. Gordon, *Adv. Energy Mater.*, 2011, 1116.
- [89] A. Ghazali, Z. Zainal, M. Z. Hussein and A. Kassim, *Sol. Energ. Mat. Sol. C.*, 1998, **55**, 237–249.
- [90] M. Sugiyama, K. Miyauchi, T. Minemura, K. Ohtsuka, K. Noguchi and H. Nakaniishi, *Jpn. J. Appl. Phys.*, 2008, **47**, 4494–4495.
- [91] C. C. Huang, Y. J. Lin, C. Y. Chuang, C. J. Liu and Y. W. Yang, *J. Alloys Compd.*, 2013, **553**, 208–211.

- [92] B. Ghosh, M. Das, P. Banerjee and S. Das, *Appl. Surf. Sci.*, 2008, **254**, 6436–6440.
- [93] K. Hartman, J. Johnson, M. I. Bertoni, D. Recht, M. J. Aziz, M. A. Scarpulla and T. Buonassisi, *Thin Solid Films*, 2011, **519**, 7421–7424.
- [94] M. Nassary, *J. Alloys Compd.*, 2005, **398**, 21 – 25.
- [95] M. Cruz, J. Morales, J. P. Espinos and J. Sanz, *J. Solid State Chem.*, 2003, **175**, 359–365.
- [96] H. Schafer, *Z. Anorg. Chem.*, 1956, **286**, 42.
- [97] R. Nitsche, H. U. Bolsterli and M. Lichtensteiger, *J. Phys. Chem. Solids*, 1961, **21**, 199–205.
- [98] D. Colombara, S. Delsante, G. Borzone, J. Mitchels, K. Molloy, L. Thomas, B. Mendis, C. Cummings, F. Marken and L. Peter, *J. Cryst. Growth*, 2013, **364**, 101–110.
- [99] *CRC Handbook of Chemistry and Physics*, ed. W. M. Haynes, CRC Press, Boca Raton, FL, 92nd edn, 2011-2012.
- [100] M. Born and V. Fock, *Z. Phys.*, 1928, **51**, 165–180.
- [101] P. A. M. Dirac, *Proc. R. Soc. A*, 1929, **123**, 714–733.
- [102] A. L. Hughes and M. A. Starr, *Phys. Rev.*, 1938, **54**, 189–193.
- [103] P. J. Mohr, B. N. Taylor and D. B. Newell, *Rev. Mod. Phys.*, 2008, **80**, 633–730.
- [104] M. Born and R. Oppenheimer, *Ann. Phys.*, 1927, **389**, 457–484.
- [105] W. Pauli, *Z. Phys.*, 1925, **31**, 373.
- [106] J. C. Slater, *Phys. Rev.*, 1929, **34**, 1293–1322.
- [107] D. R. Hartree, *Proc. Camb. Phil. Soc.*, 1928, **24**, 89.
- [108] P. Hohenberg and W. Kohn, *Phys. Rev.*, 1964, **136**, B864–B871.
- [109] W. Kohn and L. J. Sham, *Phys. Rev.*, 1965, **140**, A1133–A1138.
- [110] J. G. Lee, *Computational Materials Science*, CRC Press, Boca Raton, 2012.
- [111] E. Fermi, *Z. Phys.*, 1928, **48**, 73–79.

- [112] L. H. Thomas, *Math. Proc. Cambridge*, 1927, **23**, 542–548.
- [113] R. G. Parr and W. Yang, *Density-Functional Theory of Atoms and Molecules*, Oxford University Press, Oxford, 1989.
- [114] P. A. M. Dirac, *Math. Proc. Cambridge*, 1930, **26**, 376–385.
- [115] E. H. Lieb, *Rev. Mod. Phys.*, 1981, **53**, 603–641.
- [116] J. P. Perdew and Y. Wang, *Phys. Rev. B*, 1986, **33**, 8800.
- [117] J. P. Perdew and A. Zunger, *Phys. Rev. B*, 1981, **23**, 5048–5079.
- [118] U. von Barth and L. Hedin, *J. Phys. C*, 1972, **5**, 1629.
- [119] J. P. Perdew, A. Ruzsinszky, G. I. Csonka, O. A. Vydrov, G. E. Scuseria, L. A. Constantin, X. Zhou and K. Burke, *Phys. Rev. Lett.*, 2008, **100**, 136406.
- [120] A. D. Becke, *J. Chem. Phys.*, 1993, **98**, 1372–1377.
- [121] A. D. Becke, *J. Chem. Phys.*, 1993, **98**, 5648–5652.
- [122] J. Heyd, G. E. Scuseria and M. Ernzerhof, *J. Chem. Phys.*, 2006, **124**, 219906.
- [123] T. L. Bahers, M. Rerat and P. Sautet, *J. Phys. Chem. C*, 2014, **118**, 5997–6008.
- [124] R. P. Feynman, *Phys. Rev.*, 1939, **56**, 340–343.
- [125] H. Hellmann, *Einführung in die Quantenchemie*, Franz Deuticke, 1937.
- [126] F. Bloch, *Z. Phys.*, 1929, **52**, 555–600.
- [127] P. E. Blöchl, *Phys. Rev. B*, 1994, **50**, 17953–17979.
- [128] A. Lambros, D. Geraleas and N. Economou, *J. Phys. Chem. Solids*, 1974, **35**, 537–541.
- [129] R. Kniep, D. Mootz, U. Severin and H. Wunderlich, *Acta Crystallogr. Sect. B: Struct. Sci.*, 1982, **38**, 2022–2023.
- [130] R. M. Hazen and L. W. Finger, *Am. Mineral.*, 1978, **63**, 289–292.
- [131] T. Chattopadhyay, J. Pannetier and H. G. Von Schnerring, *J. Phys. Chem. Solids*, 1986, **47**, 879–885.

- [132] L. S. Price, I. P. Parkin, A. M. E. Hardy, R. J. H. Clark, T. G. Hibbert and K. C. Molloy, *Chem. Mater.*, 1999, **11**, 1792–1799.
- [133] M. R. Fadavieslam, N. Shahtahmasebi, M. Rezaee-Roknabadi and M. M. Bagheri-Mohagheghi, *Phys. Scr.*, 2011, **84**, 035705.
- [134] S. Lopez and A. Ortiz, *Semicond. Sci. Technol.*, 1994, **9**, 2130.
- [135] S. Kodigala, *Thin Film Solar Cells From Earth Abundant Materials: Growth and Characterization of Cu₂(ZnSn)(SSe)4 Thin Films and Their Solar Cells*, Elsevier Science, 2013.
- [136] *Handbook of Photovoltaic Science and Engineering*, ed. A. Luque and S. Hegedus, Wiley, 2nd edn, 2011.
- [137] J. C. Yang, B. Kolasa, J. M. Gibson and M. Yeadon, *Appl. Phys. Lett.*, 1998, **73**, 2841–2843.
- [138] *Encyclopedie des gaz*: Elsevier, 1976.
- [139] A. Weber, R. Mainz and H. W. Schock, *J. Appl. Phys.*, 2010, **107**, 013516.
- [140] P. Jain and P. Arun, *J. Semicond.*, 2013, **34**, 093004.
- [141] V. Blum, R. Gehrke, F. Hanke, P. Havu, V. Havu, X. Ren, K. Reuter and M. Scheffler, *Comput. Phys. Commun.*, 2009, **180**, 2175–2196.
- [142] G. Kresse and J. Furthmüller, *Phys. Rev. B*, 1996, **54**, 11169.
- [143] J. D. Head and M. C. Zerner, *Chem. Phys. Lett.*, 1985, **122**, 264–270.
- [144] G. H. F. Diercksen and S. Wilson, *Methods in Computational Molecular Physics*, Springer, 1983.
- [145] A. N. Mariano and K. L. Chopra, *Appl. Phys. Lett.*, 1967, **10**, 282–284.
- [146] E. C. Greyson, J. E. Barton and T. W. Odom, *Small*, 2006, **2**, 368–371.
- [147] D. Avellaneda, M. T. S. Nair and P. K. Nair, *J. Electrochem. Soc*, 2008, **155**, D517–D525.
- [148] M. Kan, J. Y. Wang, X. W. Li, S. H. Zhang, Y. W. Li, Y. Kawazoe, Q. Sun and P. Jena, *J. Phys. Chem. C*, 2014, **118**, 1515–1522.

- [149] H. Wiedemeier and F. J. Csillag, *Z. Kristallogr.*, 1979, **149**, 17.
- [150] R. Ibberson, O. Moze and C. Petrillo, *Mol. Phys.*, 1992, **76**, 395–403.
- [151] B. E. Warren and J. T. Burwell, *J. Chem. Phys.*, 1935, **3**, 6–8.
- [152] A. J. Bijl and N. H. Kolkmeijer, *J. Rontgen Soc.*, 1919, **15**, 101–101.
- [153] B. Bilenkii, A. Mikolaichuk and D. Freik, *Phys. Status Solidi*, 1968, **28**, K5–K7.
- [154] S. K. Arora, D. H. Patel and M. K. Agarwal, *Cryst. Res. Technol.*, 1993, **28**, 623–627.
- [155] W. J. Moore and L. Pauling, *J. Am. Chem. Soc.*, 1941, **63**, 1392–1394.
- [156] W. H. Baur and A. A. Khan, *Acta Crystallogr. Sect. B: Struct. Sci.*, 1971, **27**, 2133–2139.
- [157] J. D. Donaldson and D. C. Puxley, *Acta Crystallogr. Sect. B: Struct. Sci.*, 1972, **28**, 864–867.
- [158] R. A. Howie, W. Moser and I. C. Trevena, *Acta Crystallogr. Sect. B: Struct. Sci.*, 1972, **28**, 2965–2971.
- [159] R. G. Dickinson, *J. Am. Chem. Soc.*, 1923, **45**, 958–962.
- [160] N.-H. Dung and F. Thévet, *Acta Crystallogr. Sect. B: Struct. Sci.*, 1976, **32**, 1108–1111.
- [161] R. Sharma and Y. Chang, *J. Phase Equilib.*, 1986, **7**, 269–273.
- [162] A. V. Novoselova, V. P. Zlomanov, S. G. Karbanov, O. V. Matveyev and A. M. Gaskov, *Prog. Solid State Chem.*, 1972, **7**, 85–115.
- [163] V. Piacente, S. Foglia and P. Scardala, *ChemInform*, 1992, **23**, 19.
- [164] B. Schatschneider and J. Liang, Soft Matter, Biological Materials and Biomedical Materials - Synthesis, Characterization and Applications Symposium, 2011.
- [165] A. Tanuevski and D. Poelman, *Sol. Energ. Mat. Sol. C.*, 2003, **80**, 297–303.
- [166] A. Walsh and G. W. Watson, *J. Phys. Chem. B*, 2005, **109**, 18868–18875.
- [167] L. A. Burton and A. Walsh, *J. Solid State Chem.*, 2012, **196**, 157.

- [168] A. Walsh and S. M. Woodley, *Phys. Chem. Chem. Phys.*, 2010, **12**, 8446–8453.
- [169] R. Colin and J. Drowart, *J. Chem. Phys.*, 1962, **37**, 1120–1125.
- [170] L. A. Curtiss, K. Raghavachari, P. C. Redfern and J. A. Pople, *J. Chem. Phys.*, 1997, **106**, 1063–1079.
- [171] S. Ping Ong, L. Wang, B. Kang and G. Ceder, *Chem. Mater.*, 2008, **20**, 1798–1807.
- [172] S. P. Ong, A. Jain, G. Hautier, B. Kang and G. Ceder, *Electrochim. Commun.*, 2010, **12**, 427–430.
- [173] J. J. Scragg, P. J. Dale, D. Colombara and L. M. Peter, *ChemPhysChem*, 2012, **13**, 3035–3046.
- [174] J. J. Scragg, J. T. Watjen, M. Edoff, T. Ericson, T. Kubart and C. Platzer-Bjorkman, *J. Am. Chem. Soc.*, 2012, **134**, 19330.
- [175] A. Schneikart, H. J. Schimper, A. Klein and W. Jaegermann, *J. Phys. D: Appl. Phys.*, 2013, **46**, 305109.
- [176] S. Nishiwaki, N. Kohara, T. Negami and T. Wada, *Jpn. J. Appl. Phys.*, 1998, **37**, L71–L73.
- [177] Y. Sun, Z. Zhong, T. Shirakawa, C. Franchini, D. Li, Y. Li, S. Yunoki and X. Q. Chen, *Phys. Rev. B*, 2013, **88**, 235122.
- [178] S. Cheng and G. Conibeer, *Thin Solid Films*, 2011, **520**, 837–841.
- [179] Z. Zainal, M. Z. Hussein and A. Ghazali, *Sol. Energ. Mat. Sol. Cells*, 1996, **40**, 347–357.
- [180] Yanuar, F. Guastavino, C. Llinares, K. Djessas and G. Masse, *J. Mater. Sci. Lett.*, 2000, **19**, 2135–2137.
- [181] N. K. Reddy and K. T. R. Reddy, *Mater. Chem. Phys.*, 2007, **102**, 13–18.
- [182] M. Calixto-Rodriguez, H. Martinez, A. Sanchez-Juarez, J. Campos-Alvarez, A. Tiburcio-Silver and M. E. Calixto, *Thin Solid Films*, 2009, **517**, 2497–2499.
- [183] A. J. Ragina, K. V. Murali, K. C. Preetha, K. Deepa and T. L. Remadevi, *AIP Conference Proceedings*, 2011, **1391**, 752–754.

- [184] L. Amalraj, C. Sanjeeviraja and M. Jayachandran, *J. Crys. Growth*, 2002, **234**, 683–689.
- [185] G. Domingo, R. S. Itoga and C. R. Kannewurf, *Phys. Rev.*, 1966, **143**, 536–541.
- [186] A. Sanchez-Juarez and A. Ortz, *Semicond. Sci. Technol.*, 2002, **17**, 931.
- [187] C. Shi, Z. Chen, G. Shi, R. Sun, X. Zhan and X. Shen, *Thin Solid Films*, 2012, **520**, 4898–4901.
- [188] U. Alpen, J. Fenner and E. Gmelin, *Mater. Res. Bull.*, 1975, **10**, 175–180.
- [189] S. Lopez, S. Granados and A. Ortz, *Semicond. Sci. Technol.*, 1996, **11**, 433.
- [190] R. D. Engelken, H. E. McCloud, C. Lee, M. Slayton and H. Ghoreishi, *J. Electrochem. Soc.*, 1987, **134**, 2696–2707.
- [191] M. Khadraoui, N. Benramdane, C. Mathieu, A. Bouzidi, R. Miloua, Z. Kebab, K. Sahraoui and R. Desfeux, *Solid State Commun.*, 2010, **150**, 297–300.
- [192] H. B. H. Salah, H. Bouzouita and B. Rezig, *Thin Solid Films*, 2005, **480**, 439–442.
- [193] J. Pankove, *Optical Processes in Semiconductors*, Dover, 1971.
- [194] S. Baco, A. Chik and F. M. Yassin, *J. Sci. Technol.*, 2012, **4**, 61.
- [195] L. Cheng, M. Liu, M. Wang, S. Wang, G. Wang, Q. Zhou and Z. Chen, *J. Alloys Compd.*, 2012, **545**, 122–129.
- [196] N. Sarkar and S. Ghosh, *J. Phys.: Condens. Matter*, 2006, **18**, 1687.
- [197] E. Guneri, F. Gode, C. Ulutas, F. Kirmizigul, G. Altindemir and C. Gumus, *Chalcogenide Lett.*, 2010, **7**, 685.
- [198] N. K. Reddy, Y. B. Hahn, M. Devika, H. R. Sumana and K. R. Gunasekhar, *J. Appl. Phys.*, 2007, **101**, 093522.
- [199] G. Gauglitz and T. Vo-Dinh, *Handbook of Spectroscopy*, Wiley, 2006.
- [200] A. R. H. F. Ettema, R. A. de Groot, C. Haas and T. S. Turner, *Phys. Rev. B*, 1992, **46**, 7363–7373.
- [201] M. Sugiyama, T. Shimizu, D. Kawade, K. Ramya and K. T. Ramakrishna Reddy, *J. Appl. Phys.*, 2014, **115**, 083508.

- [202] V. Stevanovic, K. Hartman, R. Jaramillo, S. Ramanathan, T. Buonassisi and P. Graf, *Appl. Phys. Lett.*, 2014, **104**, 211603.
- [203] D. R. Harada, *MSc thesis*, Oregon State University, 2010.
- [204] A. Walsh, S. Chen, S.-H. Wei and X. G. Gong, *Adv. Energy Mater.*, 2012, **2**, 400–409.
- [205] B. R. Klaus. Ellmer, Andreas Klein, *Transparent Conductive Zinc Oxide*, Springer-Verlag, 2008.
- [206] A. Walsh, D. J. Payne, R. G. Egdell and G. W. Watson, *Chem. Soc. Rev.*, 2011, **40**, 4455.
- [207] G. Teeter, *J. Appl. Phys.*, 2007, **102**, 034504.
- [208] Y. Hinuma, F. Oba, Y. Kumagai and I. Tanaka, *Phys. Rev. B*, 2012, **86**, 245433.
- [209] A. Walsh, S. Chen, S. H. Wei and X. G. Gong, *Adv. Energy Mater.*, 2012, **2**, 400.
- [210] W. Setyawan and S. Curtarolo, *Comput. Mater. Sci.*, 2010, **49**, 299–312.
- [211] J. Vidal, S. Lany, M. d’Avezac, A. Zunger, A. Zakutayev, J. Francis and J. Tate, *Appl. Phys. Lett.*, 2012, **100**, 032104.
- [212] B. D. Malone and E. Kaxiras, *Phys. Rev. B*, 2013, **87**, 245312.
- [213] J. M. Skelton, S. C. Parker, A. Togo, I. Tanaka and A. Walsh, *Phys. Rev. B*, 2014, **89**, 205203.
- [214] L. N. Kantorovich, *Phys. Rev. B*, 1995, **51**, 3520–3534.
- [215] F. D. Murnaghan, *PNAS*, 1944, **30**, 244–247.
- [216] R. E. Banai, L. A. Burton, S. G. Choi, F. Hofherr, T. Sorgenfrei, A. Walsh, B. To, A. Croll and J. R. S. Brownson, *J. Appl. Phys.*, 2014, **116**, 013511.
- [217] M. Gajdoš, K. Hummer, G. Kresse, J. Furthmüller and F. Bechstedt, *Phys. Rev. B*, 2006, **73**, 045112.
- [218] C. Cifuentes, M. Botero, E. Romero, C. A. C. and G. Gordillo, *Braz. J. Phys.*, 2006, **36**, 1046–1049.

- [219] T. Ikuno, R. Suzuki, K. Kitazumi, N. Takahashi, N. Kato and K. Higuchi, *Appl. Phys. Lett.*, 2013, **102**, 193901.
- [220] N. Mathews, J. Tamy Benitez, F. Paraguay-Delgado, M. Pal and L. Huerta, *J. Mater. Sci.: Mater. Electron.*, 2013, **24**, 4060–4067.
- [221] M. Devika, N. K. Reddy, D. S. Reddy, Q. Ahsanulhaq, K. Ramesh, E. S. R. Gopal, K. R. Gunasekhar and Y. B. Hahn, *J. Electrochem. Soc.*, 2008, **155**, H130–H135.
- [222] L. A. Burton, D. Colombara, R. D. Abellon, F. C. Grozema, L. M. Peter, T. J. Savenije, G. Dennler and A. Walsh, *Chem. Mater.*, 2013, **25**, 4908–4916.
- [223] J. Nelson, *The Physics of Solar Cells*, Imperial College Press, 2003.
- [224] L. A. Burton and A. Walsh, *Appl. Phys. Lett.*, 2013, **102**, 132111.
- [225] P. Sinsermsuksakul, R. Chakraborty, S. B. Kim, S. M. Heald, T. Buonassisi and R. G. Gordon, *Chem. Mater.*, 2012, **24**, 4556.
- [226] P. Chelvanathan, M. I. Hossain, J. Husna, M. Alghoul, K. Sopian and N. Amin, *Jpn. J. Appl. Phys.*, 2012, **51**, 10NC32.
- [227] Q. Yan-Bin, Z. Guo-Hua, L. Di, W. Jiang-Long, Q. Xiao-Ying and Z. Zhi, *Chin. Phys. Lett.*, 2007, **24**, 1050.
- [228] R. Albrecht, L. Gmelin and A. Slawisch, *Gmelin Handbook of Inorganic and Organometallic Chemistry: Organorhenium Compounds, Binuclear Compounds 1*, Springer-Verlag, 1995.
- [229] R. H. Williams and A. J. McEvoy, *Phys. Status Solidi (B)*, 1971, **47**, 217–224.
- [230] H. Hughes and H. Starnberg, *Electron Spectroscopies Applied to Low-dimensional Structures*, Springer Netherlands, 2001.
- [231] K. Motizuki, *Structural Phase Transitions in Layered Transition Metal Compounds*, Springer, 1986.
- [232] E. E. Krasovskii and V. N. Strocov, *J. Phys.: Condens. Matter*, 2009, **21**, 314009.
- [233] D. Braga, I. Gutierrez Lezama, H. Berger and A. F. Morpurgo, *Nano Lett.*, 2012, **12**, 5218–5223.
- [234] S. Fiechter, *Sol. Energy Mater.*, 2004, **83**, 459–477.

- [235] P. Y. Yu and M. Cardona, *Fundamentals of Semiconductors*, Springer-Verlag, New York, USA, 2003.
- [236] N. R. Mathews, H. B. M. Anaya, M. A. Cortes-Jacome, C. Angeles-Chavez and J. A. Toledo-Antonio, *J. Electrochem. Soc.*, 2010, **157**, H337–H341.
- [237] R. W. Miles, O. E. Ogah, G. Zoppi and I. Forbes, *Thin Solid Films*, 2009, **517**, 4702–4705.
- [238] G. Barone, T. G. Hibbert, M. F. Mahon, K. C. Molloy, L. S. Price, I. P. Parkin, A. M. E. Hardy and M. N. Field, *J. Mater. Chem.*, 2001, **11**, 464–468.
- [239] V. R. Reddy, N. R. Reddy and C. Choi, *Solid-State Electron.*, 2005, **49**, 1213–1216.
- [240] C. Julien, M. Eddrief, I. Samaras and M. Balkanski, *Mater. Sci. Eng. B-Solid*, 1992, **15**, 70–72.
- [241] A. Wangperawong, S. M. Herron, R. R. Runser, C. Hagglund, J. T. Tanskanen, H.-B.-R. Lee, B. M. Clemens and S. F. Bent, *Appl. Phys. Lett.*, 2013, **103**, 052105.
- [242] P. Sinsermsuksakul, K. Hartman, S. B. Kim, J. Heo, L. Sun, H. H. Park, R. Chakraborty, T. Buonassisi and R. G. Gordon, *Appl. Phys. Lett.*, 2013, **102**, 053901.
- [243] S. Bowden, K. Ghosh and C. Honsberg, *Solar cells without p-n junctions*, The international society for optics and photonics technical report, 2013.
- [244] P. Sellin, A. W. Davies, A. Lohstroh, M. Ozsan and J. Parkin, *IEEE Trans. Nucl. Sci.*, 2005, **52**, 3074–3078.
- [245] S. G. Patil and R. H. Tredgold, *J. Phys. D: Appl. Phys.*, 1971, **4**, 718.
- [246] W. Albers, C. Haas and F. van der Maesen, *J. Phys. Chem. Solids*, 1960, **15**, 306 – 310.
- [247] H. C. Montgomery, *J. Appl. Phys.*, 1971, **42**, 2971–2975.
- [248] C. G. Van de Walle and J. Neugebauer, *J. Appl. Phys.*, 2004, **95**, 3851–3879.
- [249] P. M. Fahey, P. B. Griffin and J. D. Plummer, *Rev. Mod. Phys.*, 1989, **61**, 289–384.
- [250] G. K. Madsen and D. J. Singh, *Comput. Phys. Commun.*, 2006, **175**, 67–71.

- [251] S. P. Ong, W. D. Richards, A. Jain, G. Hautier, M. Kocher, S. Cholia, D. Gunter, V. L. Chevrier, K. A. Persson and G. Ceder, *Comput. Mater. Sci.*, 2013, **68**, 314–319.
- [252] N. Ashcroft and N. Mermin, *Solid state physics*, Saunders College, 1976.
- [253] G. Hautier, A. Miglio, G. Ceder, G.-M. Rignanese and X. Gonze, *Nat. Commun.*, 2013, **4**, 2292.
- [254] E. Seebauer and M. Kratzer, *Charged Semiconductor Defects: Structure, Thermodynamics and Diffusion*, Springer, 2008.
- [255] J. Bardeen and W. Shockley, *Phys. Rev.*, 1950, **80**, 72–80.
- [256] Y. Le Page and P. Saxe, *Phys. Rev. B*, 2002, **65**, 104104.
- [257] G. S. Manyali, *PhD thesis*, University of Witwatersrand, 2012.
- [258] J. Moreno and J. M. Soler, *Phys. Rev. B*, 1992, **45**, 13891–13898.
- [259] N. Li, B. E. Lassiter, R. R. Lunt, G. Wei and S. R. Forrest, *Appl. Phys. Lett.*, 2009, **94**, 023307.
- [260] A. R. Moore, *Appl. Phys. Lett.*, 1977, **31**, 762–764.
- [261] Y. He and G. Galli, *Chem. Mater.*, 2014, **26**, 5394–5400.
- [262] C. Persson, *J. Appl. Phys.*, 2010, **107**, 053710.
- [263] A. R. Garcia-Angelmo, M. Nair and P. Nair, *Solid State Sci.*, 2014, **30**, 26–35.
- [264] Y. Sun, H. Cheng, S. Gao, Z. Sun, Q. Liu, Q. Liu, F. Lei, T. Yao, J. He, S. Wei and Y. Xie, *Angew. Chem. Int. Ed.*, 2012, **51**, 8727–8731.
- [265] R. Krishnan and D. Upadhyaya, *Pramana*, 1985, **24**, 351–359.

Appendix A

Appendix

A.1 Single crystal XRD data

Table A.1: Single crystal crystallographic data for SnS_2 & Sn_2S_3 .

	SnS_2	Sn_2S_3
Mr	182.81	333.56
Crystal System	Trigonal	Orthorhombic
Space Group	R -3	Pnma
a,b,c (Å)	3.6349(2), 3.6349(2), 52.856(4)	8.8490(2) 3.74150(10) 13.9925(3)
γ (°)	120	90
V (Å ³)	604.80(7)	463.271(19)
Z	9	4
$\mu(\text{mm}^{-1})$	10.676	11.929
F(000)	738	592
T_{min} / T_{max}	0.14450/1.00000	0.21362 / 1.00000
2θ range (°)	3.47 / 32.81	2.91 / 32.84
No. reflections	508	11203
R[F]/wR[F2] (all data)	0.0365 / 0.0793	0.0229 / 0.0485
Restraints/Parameters	0/15	0/32

A.2 Glow discharge mass spectroscopy data

Table A.2: Glow discharge mass spectroscopy of an SnS single crystal

Element	Detection Limit (ppm wt)	Concentration		
		(ppm wt)	(atom ppm)	(cm ⁻³)
Li	0.010	< 0.01		
Be	0.010	< 0.01		
B		< 0.01		
F	0.100	< 0.1		
Na		0.390	1.279	5.32e16
Mg	0.050	0.120	0.372	1.55e16
Al		5.300	14.809	6.16e17
Si	- 0.3 wt%	1.800	4.832	2.01e17
P		< 0.05		
S	Matrix	Matrix		
Cl		2.400	5.104	2.12e17
K	0.100	< 0.1		
Ca		0.270	0.508	2.11e16
Sc	0.005	< 0.005		
Ti	0.010	< 0.01		
V	0.010	< 0.01		
Cr		< 0.01		
Mn	0.010	< 0.01		
Fe	0.010	0.190	0.256	1.07e16
Co	0.010	0.080	0.102	4.26e15
Ni	0.010	0.080	0.103	4.27e15
Cu	0.010	< 0.01		
Zn		0.050	0.058	2.40e15
Ga	0.010	< 0.01		

Element	Detection Limit (ppm wt)	Concentration		
		(ppm wt)	(atom ppm)	(cm ⁻³)
Ge	0.010	< 0.01		
As	10.000	< 0.1		
Se	0.050	< 0.05		
Br	0.050	< 0.05		
Rb	0.010	< 0.01		
Sr	0.010	< 0.01		
Y	0.010	< 0.01		
Zr	0.010	< 0.01		
Nb	0.010	< 0.01		
Mo	0.050	< 0.05		
Ru	0.050	< 0.05		
Rh	0.010	< 0.01		
Pd	0.010	< 0.01		
Ag	0.500	< 0.5		
Cd	0.500	< 0.5		
In	Binder	Binder		
Sn	Matrix	Matrix		
Sb		100.000	61.917	2.58×10^{18}
Te		< 0.5		
I	0.500	620.000	368.323	1.53×10^{19}
Cs	0.100	< 0.1		
Ba	0.050	< 0.05		
La	0.050	< 0.05		
Ce	0.010	< 0.01		
Pr	0.010	< 0.01		
Nd	0.010	< 0.01		
Sm	0.010	< 0.01		
Eu	0.050	< 0.05		
Gd	0.010	< 0.01		
Tb	0.010	< 0.01		
Dy	0.010	< 0.01		
Ho	0.010	< 0.01		
Er	0.010	< 0.01		

Element	Detection Limit (ppm wt)	Concentration		
		(ppm wt)	(atom ppm)	(cm ⁻³)
Tm	0.010	< 0.01		
Yb	0.010	< 0.01		
Lu	0.010	< 0.01		
Hf	0.010	< 0.01		
Ta	Source	Source		
W	0.010	< 0.01		
Re	0.010	< 0.01		
Os	0.010	< 0.01		
Ir	0.010	< 0.01		
Pt	0.010	< 0.01		
Au	0.100	< 0.1		
Hg	0.050	< 0.05		
Tl		< 0.05		
Pb		280.000	101.878	4.24×10^{18}
Bi		4.300	1.551	6.45×10^{16}
Th	0.005	< 0.005		
U	0.005	< 0.005		

A.3 X-ray photoelectron spectroscopy data

Table A.3: XPS atomic concentration peak assignments of SnS, SnS₂ & Sn₂S₃

Peak	SnS	SnS post anneal	SnS ₂	Sn ₂ S ₃
Sn a	7.62	3.83	1.6	9.55
Sn b	12.33	13.86	0	6.9
Sn c	10.12	15.26	0	5.73
Sn d	0.47	0.72	0	0.2
Sn e	0	0	19.43	0
Sn f	0	0	0.74	0
S a	12.03	13.32	27.51	10.12
S b	3.45	2.41	0	1.33
S c	0	0	2.1	0
C a	17.2	21.62	20.12	26.41
C b	3.14	1.96	2.17	2.34
C c	0	0	9.44	0
O a	20.59	20.29	3.11	20.2
O b	7.71	4.26	6.48	13.99
O c	2.57	1.34	3.26	3.22
O d	0	0	4.03	0
I a	2.78	1.14	0	0

A.4 Optical absorption coefficient script

```
#!/bin/python
import numpy as np
import matplotlib.pyplot as plt

RDie = list()
IDie = list()

# Open the file and split into Lines
f = open('OUTCAR','r')
lines = f.readlines()
f.close()

copy = 0
i = 0
for line in lines:
    inp = line.split()
    if inp == []:
        continue
    if len(inp) > 3 and inp[2] == "IMAGINARY" and inp[3] == "DIELECTRIC":
        copy = 1
    if copy == 1 and len(inp) > 3 and inp[2] == "REAL":
        copy = 0
    if copy == 1 and len(inp) == 7 and inp[1] != "X":
        IDie.append((inp[:]))
    i = i + 1
```

```

IDie= np.asarray(IDie)
IDie = IDie.astype(np.float)

copy = 0
i = 0
for line in lines:
    inp = line.split()
    if inp == []:
        continue
    if len(inp) > 3 and inp[2] == "REAL"
        and inp[3] == "DIELECTRIC":
        copy = 1
    if copy == 1 and len(inp) > 3 and inp[1] == "outermost":
        copy = 0
    if copy == 1 and len(inp) == 7 and inp[1] != "X":
        RDie.append((inp[:]))
        i = i + 1

RDie= np.asarray(RDie)
RDie = RDie.astype(np.float)

top = 0
bottom = len(RDie[:, 1])

C=2.99792458*10**10      # cm / s
h=4.135668*10**-15       # eV S

```

```

Alpha = list()

for x in range (top , bottom):
    for y in range(1 , 4):
        Alpha.append((2*(RDie[x , 0]/h)*(np.sqrt(2)/2)*np.sqrt((RDie[x , y]**2 + IDie [x , y]**2)**0.5 - RDie[x , y]))/C)

Alpha= np.asarray(Alpha)
Alpha = Alpha.astype(np.float).reshape(bottom ,3)

plt.plot(RDie[:,0] ,Alpha[:,0] , 'r-' , lw=2 , label = 'a')
plt.plot(RDie[:,0] ,Alpha[:,1] , 'b-' , lw=2 , label = 'b')
plt.plot(RDie[:,0] ,Alpha[:,2] , 'k-' , lw=2 , label = 'c')
plt.xlim(0 , 3.5)
plt.ylim(0 , 100000)
plt.xlabel(r'Energy_(eV)' , fontsize=18)
plt.ylabel(r'Absorption_Coefficient_{$10^5$cm$^{-1}$}' ,
           fontsize=18)
plt.ticklabel_format(style='sci' , axis='y' , scilimits=(0,0))
plt.legend(loc=2,
           ncol=1 , borderaxespad=0.)

plt.show()

```

A.5 Charge carrier mobility script

```
#!/bin/python

import numpy as np
import matplotlib.pyplot as plt
import scipy.constants as spc

Np = 2.28e25      #reciprocal cubic m
Nn = 4.888689e17 #reciprocal cubic m
Mpa = 1.339634e-30 #kg
Mpb = 1.418162e-31 #kg
Mpc = 9.868653e-31 #kg
Ca = 6.9436e10    #pascals
Cb = 9.1004e10    #pascals
Cc = 4.3649e10    #pascals
Era = 11.846846   #unitless
Erb = 14.018616   #unitless
Erc = 12.704445   #unitless
Ed = 4.3627e-19 #joules
T = 298           #kelvin

xia = ((3*(spc.pi**2))**(.1/3.))*((
    spc.epsilon_0*Era*(spc.h**2)*(
        Np*(1./3.)))/(Mpa*(spc.e**2)))
Fia = np.log(1+xia)-(xia/(1+xia))
muia = (3*(spc.epsilon_0*Era)**2*(spc.h**3))/(
    4*Mpa**2*spc.e**3*Fia)      #m^2 / V s
```

```

xib = ((3*(spc.pi**2))**(.1/3.))*(((
    spc.epsilon_0*Erb*(spc.h**2)*(
        Np*(1./3.))/((Mpb*(spc.e**2)))
    Fib = np.log(1+xib)-(xib/(1+xib))
    muib = (3*(spc.epsilon_0*Erb)**2*(spc.h**3))/(
        4*Mpb**2*spc.e**3*Fib) #m^2 / V s

xic = ((3*(spc.pi**2))**(.1/3.))*(((
    spc.epsilon_0*Erc*(spc.h**2)*(
        Np*(1./3.))/((Mpc*(spc.e**2)))
    Fic = np.log(1+xic)-(xic/(1+xic))
    muic = (3*(spc.epsilon_0*Erc)**2*(
        spc.h**3))/(4*Mpc**2*spc.e**3*Fic) #m^2 / V s

mula = (2*np.sqrt(2*spc.pi)*spc.e*spc.hbar**4*Ca)/(
    3*Mpa**(.5/2.)*Ed**2*(spc.k*T)**(.3/2.)) #m^2 / V s
mulb = (2*np.sqrt(2*spc.pi)*spc.e*spc.hbar**4*Cb)/(
    3*Mpb**(.5/2.)*Ed**2*(spc.k*T)**(.3/2.)) #m^2 / V s
mulc = (2*np.sqrt(2*spc.pi)*spc.e*spc.hbar**4*Cc)/(
    3*Mpc**(.5/2.)*Ed**2*(spc.k*T)**(.3/2.)) #m^2 / V s

munab = (Mpa*spc.e**3)/(
    20*Era*spc.epsilon_0*spc.hbar**3*Nn) #m^2 / V s
munb = (Mpb*spc.e**3)/(
    20*Erb*spc.epsilon_0*spc.hbar**3*Nn) #m^2 / V s
munc = (Mpc*spc.e**3)/(

```

```

20*Erc*spc . epsilon_0*spc . hbar**3*Nn) #m^2 / V s

invmua = 1/muia + 1/mula + 1/muna
invmub = 1/muib + 1/mulb + 1/munb
invmuc = 1/muic + 1/mulc + 1/munc

mua = 1/invmua
mub = 1/invmub
muc = 1/invmuc

totmu = np.sqrt(mua**2 + mub**2 + muc**2)

tau_a = (mua*Mpa)/spc.e
tau_b = (mub*Mpb)/spc.e
tau_c = (muc*Mpc)/spc.e

f=open('boltztrap.condtens_fixdoping','r')
condtens = f
condtau = np.genfromtxt(condtens, dtype=float, delimiter=',',
skiprows=1, skip_header=0, skip_footer=0,
usecols=(2,3,4,5,6,7,8,9,10))

conduct = condtau*tau_a #Ohm^-1 m^-1

g=open('boltztrap.condtens_fixdoping','r')
tempk = g
tempk = np.genfromtxt(tempk, dtype=float, delimiter=',',

```

```

skiprows=1, skip_header=0, skip_footer=0, usecols=(0))

conducta1 = conduct[:,0]
conducta2 = conduct[:,1]
conducta3 = conduct[:,2]
conducta = np.sqrt(conducta1**2 + conducta2**2 + conducta3**3)

conductb1 = conduct[:,3]
conductb2 = conduct[:,4]
conductb3 = conduct[:,5]
conductb = np.sqrt(conductb1**2 + conductb2**2 + conductb3**3)

conductc1 = conduct[:,6]
conductc2 = conduct[:,7]
conductc3 = conduct[:,8]
conductc = np.sqrt(conductc1**2 + conductc2**2 + conductc3**3)

plt.plot(tempk, conducta*0.01, 'k--', label='A')
plt.plot(tempk, conductb*0.01, 'b--', label='B')
plt.plot(tempk, conductc*0.01, 'r--', label='C')
plt.legend(( 'a', 'b', 'c'),
           'upper_left', shadow=False)
plt.title('Conductivity -vs- temperature')
plt.xlabel('Temperature -(K)')
plt.ylabel(r'Conductivity -($\Omega^{-1}$cm$^{-1}$)')
plt.show()

```